



HAL
open science

Pore-scale modeling and hydromechanics of partially saturated granular materials

Chao Yuan

► **To cite this version:**

Chao Yuan. Pore-scale modeling and hydromechanics of partially saturated granular materials. Fluids mechanics [physics.class-ph]. Université Grenoble Alpes, 2016. English. NNT : 2016GREAI033 . tel-01504376

HAL Id: tel-01504376

<https://theses.hal.science/tel-01504376>

Submitted on 10 Apr 2017

HAL is a multi-disciplinary open access archive for the deposit and dissemination of scientific research documents, whether they are published or not. The documents may come from teaching and research institutions in France or abroad, or from public or private research centers.

L'archive ouverte pluridisciplinaire **HAL**, est destinée au dépôt et à la diffusion de documents scientifiques de niveau recherche, publiés ou non, émanant des établissements d'enseignement et de recherche français ou étrangers, des laboratoires publics ou privés.

THÈSE

Pour obtenir le grade de

DOCTEUR DE LA COMMUNAUTÉ UNIVERSITÉ GRENOBLE ALPES

Spécialité : **IMEP2/Mécanique des fluides, Procédés,
Énergétique**

Arrêté ministériel : 7 août 2006

Présentée par

Chao YUAN

Thèse dirigée par **Bruno CHAREYRE** et
codirigée par **Félix DARVE**

préparée au sein du **Laboratoire 3SR - Grenoble**
dans l'**École Doctorale IMEP2**

Pore-scale modeling and hydromechanics of partially saturated granular materials

Thèse soutenue publiquement le **04/07/2016**,
devant le jury composé de :

Mr Pierre-Yves HICHER

Professeur à l'École Centrale de Nantes, Président

Mr S. Majid HASSANIZADEH

Professeur à Utrecht University, Rapporteur

Mr Antonio GENS

Professeur à Universitat Politècnica de Catalunya, Rapporteur

Mr Jean-Michel PEREIRA

Chercheur (HDR) à l'École des Ponts ParisTech, Examineur

Mr Bruno CHAREYRE

Maître de conférences (HDR) à l'INP Grenoble, Directeur de thèse

Mr Félix DARVE

Professeur à l'INP Grenoble, Co-Directeur de thèse



Acknowledgements

I would like to express my heartfelt gratitude to my supervisors, Bruno Chareyre and Félix Darve. Thanks Félix for accepting my application and inviting me to prepare my thesis in Laboratoire 3SR. Also thanks for his immense help and sincere encouragement. My special acknowledgements are for Bruno. Thanks for his thoughtful guidance, consistent help and encouragement in the preparation of this thesis. They are excellent colleagues in work and great friends in life.

I would like to thank Prof. Pierre-Yves Hicher, Prof. Majid Hassanizadeh, Prof. Antonio Gens and Prof. Jean-Michel Pereira for accepting our invitation to be members of my defense jury.

My sincere thanks go to the colleagues of Laboratoire 3SR. Thank them for taking good care of me in research and life during these four years. I enjoyed the time here and am proud of being a 3SRian.

Very special thanks to my family. I am grateful to my father and mother for all their support and encouragement.

This work was funded by the China Scholarship Council (CSC). Their sponsorship is gratefully acknowledged.

Contents

Abstract	xiii
Résumé	xv
General Introduction	xvii
I Literature Review	1
1 Two-phase flow in granular porous media	5
1.1 Physics of two-phase flow	5
1.1.1 Solid structure and one-phase flow	5
1.1.2 Two-phase flow	6
1.2 Numerical models for two-phase flow in (deformable) porous media . . .	8
1.2.1 Macro-scale continuum models	9
1.2.2 Micro-scale continuum methods	9
1.2.3 pore-scale methods	11
2 Physics and mechanics of unsaturated granular materials	19
2.1 Introduction	19
2.2 Stress variables	20
2.2.1 A single effective stress	20
2.2.2 Independent stress variables	23
2.3 Aspects of unsaturated granular materials behavior	24
2.3.1 Volumetric change	24
2.3.2 Strength behavior	25
2.3.3 Water retention curve	26
2.4 Constitutive modeling of unsaturated soils	27
II The 2PFV-DEM model	31
3 The two-phase pore-scale finite volume modeling	33
3.1 Pore-scale network	33
3.2 Fluid phases	35
3.2.1 Local rules	35
3.2.2 Pore invasion model	37

3.3	Forces on the solid phase	44
3.3.1	Integration of fluid-phase pressure	44
3.3.2	Integration of interfacial tension	44
3.3.3	Coupling with DEM	46
4	Implementation and model test	51
4.1	Implementation	51
4.1.1	The open-source code YADE	51
4.1.2	Coupling design	51
4.2	Model test	53
4.2.1	Numerical setup	54
4.2.2	Results and discussions	55
4.2.3	Comparison with experiments	58
III	Applications of the model	63
5	Finite size effects and the representative elementary volume	65
5.1	Introduction	65
5.2	Sample size	66
5.3	Subsampling	69
5.4	Boundary conditions and aspect ratio	70
5.4.1	Effect of side boundary connectivity	71
5.4.2	Effect of aspect ratio	76
6	Bishop’s effective stress parameter	83
6.1	Simulation setup	83
6.2	Recall $\bar{p}^c - s^w - \varepsilon_{11}$ relationship	84
6.3	Reproducing the expression of effective stress parameter	84
6.3.1	Macroscopic view	85
6.3.2	Microscopic view	85
6.3.3	Results	86
6.4	Micromechanical investigation on the effective stress parameter and saturation	89
7	Toward the pendular regime	95
7.1	Introduction	95
7.2	Description of the pendular bridge model	97
7.3	Extending 2PFV to the pendular regime model	98
7.3.1	Algorithm	98
7.3.2	Implementation	99
7.4	Numerical simulation	102
7.4.1	Hydraulic results	103
7.4.2	Mechanical results	105
	Conclusions and Perspectives	117

Appendix	121
Résumé en français	137

List of Figures

1.1	Schematic representation of phase diagram showing various flow regimes under different viscosity ratio and capillary number, after Joekar-Niasar and Hassanizadeh (2012), originally based on Lenormand (1990); Lenormand et al. (1988); Sinha and Wang (2007)	8
1.2	Classification of pore network topologies: (a) structured regular, (b) structured irregular (red color illustrates isolated pores), (c) unstructured regular, and (d) unstructured irregular, after Joekar-Niasar and Hassanizadeh (2012).	12
1.3	Illustration of a liquid bridge between two particles under pendular regime, after Scholtès et al. (2009a).	15
1.4	Calculation of capillary force based on a Voronoi diagram. (a) A Voronoi cell with projection of vertices on a particle (b) Calculation of a subdomain of the particle, after Kharaghani et al. (2012).	16
1.5	Evolution of capillary forces during drying (the viscous effects are negligible). (a) Saturation of W-phase $s^w = 1.0$, (b) $s^w = 0.9$, (c) $s^w = 0.6$ and (d) $s^w = 0.3$. Gray cylinders represent empty pores, and dark blue is for liquid; capillary forces are presented by red cones, and cone size scales with force magnitude, after Kharaghani et al. (2011).	17
2.1	Components of unsaturated soil with continuous air phase (Fredlund et al., 2012).	20
2.2	The relationship between effective stress parameter χ and the degree of saturation for a number of different soils in Zerhouni (1991) and review Nuth and Laloui (2008).	22
2.3	Volumetric characteristics expressed by independent stress variables in Bishop and Blight (1963)	24
2.4	Typical water retention curve for a granular material, after Al-Sharrad (2013).	27
2.5	Stress-strain constitutive models for unsaturated soils, summarized by Fredlund et al. (2012).	28
2.6	Three-dimensional representation of the yield surface in the BBM, after Alonso et al. (1990).	29
3.1	Comparison of triangulations and their dual Voronoi graph in two dimensions. (a) the dual graph of Delaunay triangulation has branches inside discs; (b) the dual of the Regular Triangulation has all branches in the pore space.	34

3.2	Regular triangulation in three dimensions (a) and two dimensions (b). . .	35
3.3	Pore geometry. (a)A pore defined by tetrahedral element of the finite volume decomposition. (b)Definition of a pore throat geometry. r^c is the curvature of meniscus; L_{nw} is the length of contact line between NW and W phases; L_{ns} is the length of contact line between NW and S phases. $L^{eff} = \sum(L_{nw} + L_{ns})$, in which L^{eff} is termed effective entry pore throat perimeter. A^{eff} is the planar project area of NW-W interface, and is termed effective entry pore throat area.	36
3.4	The displacement of NW-W interface between two equilibrium states, from (a) $p^c < p_e^c$ to (b) $p^c > p_e^c$ (in 2D for clarity).	37
3.5	(a) Construction of subdomain Ω_{ij} , the pore of Ω_i is occupied by NW-phase (Φ_i), the pore of Ω_j is occupied by W-phase (Θ_j); (b) Two-phase fluid pressure and interfacial tension on S-phase. (in 2D for clarity). . . .	38
3.6	Illustration of boundary conditions, NW-phase invasion and W-phase trapping in the network (in 2D mapping for clarity).	40
3.7	The definition of boundary condition by using “fictitious spheres”, after Catalano (2012)	42
3.8	Pores at boundaries ,following Catalano (2012). (a) One fictitious, (b) Two fictitious and (c) three fictitious.	42
3.9	Pore throat at boundaries (a) 1 boundary + 2 spheres and (b) 2 boundaries + 1 sphere	43
3.10	The fluid boundary condition of 2PFV model (in 2D for clarity).	43
3.11	Computation cycle of a DEM model.	46
3.12	(a) Definition of normal particle displacement. (b) Normal and shear stiffnesses at contacts.	48
3.13	Elastic-plastic contact model. Normal (a) and tangential (b) interaction law (Catalano, 2012)	49
4.1	The 2PFV algorithm (one invasion step)	53
4.2	Computation cycle of 2PFV-DEM	54
4.3	The water retention curves ($\overline{p^c} - s^w$) of drainage simulation. The sample is a dense cubic packing of 1000 spheres.	55
4.4	The process of drainage (400 particles), NW-phase invade from top. Brown (gray) is solid phase, blue (black) is W-phase, and light cyan (white) is NW-phase, see color version of this figure in the HTML.	56
4.5	Distribution of capillary pressure in “with-trap” mode of drainage. Brown circle is solid phase, light region is NW-phase pressure p^n , dark regions are W-phase pressures p^w , see color version of this figure in the HTML. . .	57
4.6	Distribution of capillary pressure in “without-trap” mode of drainage. Brown circle is solid phase, light region is NW-phase pressure p^n , dark regions are W-phase pressures p^w , see color version of this figure in the HTML.	58

4.7	Forces acting on solid particles induced by NW-W phase pressure and surface tension. Forces are shown in red arrows. Brown (gray) is solid phase, blue (black) is W-phase, and light cyan (white) is NW-phase, see color version of this figure in the HTML. (b) forces acting from disconnected W-phase. (c) forces acting from W-phase front. (in 2D for clarity)	59
4.8	The relationship between normalized capillary pressure and one-dimensional deformation ($\overline{p^c} - \epsilon_{11}$) in drainage simulation under the oedometer test conditions. The sample is a dense cubic packing of 1000 spheres.	59
4.9	Comparison between simulation and experiment for primary drainage $\overline{p^c} - s^w$ curves. The number of observations of simulation is 100.	61
5.1	Average $\overline{p^c} - s^w$ curve as a function of sample size in open-side mode (100 repeated simulations for each case). See colour version of this figure online.	67
5.2	Average $\overline{p^c} - s^w$ curve as a function of sample size in closed-side mode (100 repeated simulations for each case). See colour version of this figure online.	67
5.3	The relationship between standard deviation of saturation and packing size (in open-side drainage mode).	68
5.4	Micro-porosity versus averaging subdomain size. $\overline{\phi_{sub}} = 0.34$	71
5.5	Micro-saturation versus averaging subdomain size. (a): $\overline{s_{sub}^w} = 0.4$, (b): $\overline{s_{sub}^w} = 0.2$	72
5.6	Statistics of saturation and porosity versus size of the averaging subdomain.	73
5.7	Right: a slice through a sample at $s_{sub}^w = 0.4$ (the top boundary is connected to the NW reservoir), in which strong capillary fingering can be observed. Left: zoom on two subdomains used in the averaging procedure.	74
5.8	Right: a slice through a sample at $s_{sub}^w = 0.2$ (the top boundary is connected to the NW reservoir), in which patches of trapped W-phase are visible. Left: zoom on two subdomains used in the averaging procedure. .	74
5.9	Numerical setup and indexed layers. The bottom of Layer-01 is connected to the W-phase reservoir, the top of Layer-10 is connected to the NW-phase reservoir.	75
5.10	Comparison of invasion between a simulation in open-side drainage and the experiments of Khaddour et al. (2013). (a) Simulation (dark blue: W-phase, yellow: NW-phase). (b) experiment on glass beads. (c) experiment on Hostun sand (gray: glass beads/sand, dark blue: water, white: air). . .	75
5.11	Saturation distribution of different layers under certain capillary pressures in open-side drainage.	77
5.12	Saturation distribution of different layers under certain capillary pressures in closed-side drainage.	78
5.13	Comparison between different aspect ratios of simulations for $s^w - \overline{p^c}$ curves and $D^* - \overline{p^c}$ curves in open-side drainage	79
5.14	Comparison between different aspect ratios of simulations for $s^w - \overline{p^c}$ curves and $D^* - \overline{p^c}$ curves in closed-side drainage	79
6.1	The relationship between normalized capillary pressure-saturation-strain ($\overline{p^c} - s^w - \epsilon_{11}$) during drainage simulation under the oedometer conditions.	85

6.2	Particle-centered domain for the definition of effective stress σ^* at the particles scale	86
6.3	Variation of effective stress parameter χ with saturation for simulation results and experimental data. Simulation values are calculated from drainage test of a dense packing (40,000 spheres) under the oedometer test conditions.	87
6.4	A linear and reversible evolution of strain and contact stress during the drainage. The sample first shrinks, then swells.	88
6.5	Variation of effective stress parameter χ with saturation for simulation results. Simulation values are calculated from drainage test of a loose packing (40,000 spheres) under the oedometer test conditions.	88
6.6	An irreversible evolution of strain and contact stress during the drainage. The sample first shrinks, then swells.	89
6.7	Drainage simulation under oedometer test conditions. Evolution of local normalized effective stress and local saturation. (a) $\bar{p}^c = 9.05$; (b) $\bar{p}^c = 11.35$; (c) $\bar{p}^c = 11.90$; (d) $\bar{p}^c = 16.20$	91
6.8	The relationship between micro effective stress parameter and micro saturation. Derivation is based on macro p^c , i.e., the pressure difference between reservoirs.	92
6.9	The relationship between micro effective stress parameter and micro saturation. Derivation is based on the local capillary pressure.	92
7.1	The displacement of NW-W interface between two equilibrium states. From (a) to (b), the pendular bridge is not considered in previous chapters; from (a) to (c), the pendular bridge exists, practically. (in 2D for clarity).	96
7.2	Illustration of a liquid bridge between two particles in pendular regime model. (a) global geometry and (b) details of the bridge, following Scholtès et al. (2009) and Scholtès et al. (2009a)	97
7.3	Evolution of the capillary force F_{cap} with the inter-granular distance D for a given capillary pressure value: a meniscus can form for $D < D_{creation}$ and breaks off for $D > D_{rupture}$, following Scholtès et al. (2009a)	99
7.4	Illustration of the extended 2PFV model with the pendular bridge model, in 2D for clarity. (a) unsaturated granular material and the pore network of pore space. (b) the funicular cluster is modeled by 2PFV method. (c) the pendular bridge is modeled by Scholtès et al. (2009) and Chalak (2016)	100
7.5	The extended 2PFV algorithm (one invasion step)	101
7.6	The evolution of menisci number of different models and water retention curve. Pen denotes pendular regime model (i.e., the liquid bridge in previous section); Fun+Pen denotes the extended 2PFV model, which includes funicular and pendular regimes. The water retention curve is corresponding to the Fun+Pen model.	103
7.7	Water retention curves of different drainage models.	104
7.8	The relationships between normalized capillary pressure, saturation and one-dimensional deformation (\bar{p}^c - s^w - ϵ_{11}) in with-trap model, under the oedometer test conditions. The WRC corresponds to the Fun+Pen model.	106

7.9	The relationships between normalized capillary pressure, saturation and one-dimensional deformation ($\overline{p^c - s^w - \epsilon_{11}}$) in without-trap model, under the oedometer test conditions. The WRC corresponds to the Fun+Pen model.	107
7.10	The linear and reversible evolution of strain and contact stress during the drainage using “Fun” model and “Fun+Pen” model. The samples first shrink, then swell.	108
7.11	The relationship between the capillary stress and capillary pressure in with-trap drainage. All variables have been normalized.	110
7.12	The relationship between the capillary stress and capillary pressure in without-trap drainage. All variables have been normalized.	111
7.13	Comparison of effective stress parameter between funicular regime model and pendular+funicular regime model. The simulation is controlled by with-trap drainage.	113
7.14	Variation of $\chi^M - \chi^m$ with saturation in with-trap simulations.	113
7.15	Comparison of effective stress parameter between funicular regime model and pendular+funicular regime model. The simulation is controlled by without-trap drainage.	114
7.16	Variation of $\chi^M - \chi^m$ with saturation in without-trap simulations.	114
7.17	Cross section geometry of pore throat, the pore throat radius r^c is determined based on the balance of forces for non-wetting/wetting interface.	122
7.18	Comparaison des triangulations et de leur graph dual de Voronoi en deux dimensions. (a) le graphe dual de la triangulation de Delaunay contient des branches à l’intérieur des disques; (b) le dual de la Triangulation régulière contient toutes les branches dans l’espace poral.	138
7.19	Triangulation régulière en trois dimensions (a) et en deux dimensions (b).	139
7.20	Géométrie des pores. (a) un pore tétraédrique. (b) un étranglement. r^c est la courbure de l’interface; L_{nw} longueur de la ligne de contact entre phases NW et W; L_{ns} longueur de la ligne de contact NW-S. $L^{eff} = \sum(L_{nw} + L_{ns})$ où L^{eff} est le perimetre effectif de l’étranglement. A^{eff} est l’aire d’entrée effective.	139
7.21	Illustration des conditions aux limites, l’invasion de la phase NW et le piégage de la phase W.	140
7.22	(a) Construction d’un sous-domaine Ω_{ij} , les pores de Ω_i sont occupés par la phase NW (Φ_i), le pore de Ω_j est occupé par la phase W(Θ_j); (b) La pression du fluide à deux phases et la tension interfaciale sur la phase S. (En 2D pour la clarté).	141
7.23	Comparaison entre la simulation et l’expérience pour les courbes de drainage primaire $\overline{p^c - s^w}$ (100 simulations superposées).	144
7.24	Processus de drainage (400 particules), la phase NW envahie par le haut. Brown (gris) est la phase solide, celle bleue (noir) est la phase W, et celle cyan claire (blanc) est la phase NW.	145

7.25 Distribution de la pression capillaire en mode de drainage "avec-trap".
Le cercle de Brown est en phase solide, la région en couleur claire signifie la pression p^n en phase NW, les régions en couleur sombres sont des pressions W en phase p^w 146

List of symbols

A_{ij}^{eff}	projected area of $\partial\Phi_i \cap \Theta_j$ on S_{ij} (effective entry pore throat area) in Ω_{ij} , [m ²]
A_{ij}^f	the pore throat sectional area conjugate facet S_{ij} , <i>i.e.</i> , the void space area of S_{ij} , [m ²]
C	mean curvature of the fluids interface, [m ⁻¹]
C_a	capillary number, [-]
c'	the effective cohesion, [Pa]
χ	Bishop's effective stress parameter, [-]
χ^M	expression of χ from Marco-scopic view, [-]
χ^m	expression of χ from mirco-scopic view, [-]
$\underline{\underline{\chi}}$	the micro-scale effective stress parameter, [-]
\overline{D}	the average diameter of particles, [m]
Δt	time step, [s]
δ_c	normal particle displacement, [m]
δ_{ij}	length of $\partial(\Phi_i \cup \Theta_j)$ in contact with spheres, [m]
δ_{ij}^k	length of the part of $\partial(\Phi_i \cup \Theta_j)$ in contact with sphere k , [m]
E	solid particle elastic modulus, [Pa]
ε	strain tensor
\mathbf{F}^c	the fluid force vector acting on interface, [N]
$\mathbf{F}^{c,k}$	the fluid force vector acting on particle k induced by fluids pressure, [N]
\mathbf{F}^t	the tension force vector acting on the fluids-solid contact lines, [N]
$\mathbf{F}^{t,k}$	the tension force vector acting on particle k induced by interfacial tension, [N]
\mathbf{F}^k	the total force vector acting on particle k induced by fluids pressure and interfacial tension, [N]
F_n	normal component of contact force, [N]
F_t	tangential component of contact force, [N]
Γ	part of Ω occupied by the Solid phase, [m ³]
Γ_i	domain occupied by Solid particle i , [m ³]
γ	the interfacial tension between the two fluid phases, [N/m]
I_i	particle moment of inertia
\mathbf{K}	intrinsic permeability tensor
K_{ij}	the equivalent hydraulic conductivity from i to j , [m/s]
κ	intrinsic permeability, [m ²]
L_{ij}^{eff}	total length of three-phase contact lines (effective entry pore throat perimeter) in Ω_{ij} , [m]
M	viscosity ratio, [m]
M_i	generic moment applied on particle i , [N·m]
m_i	particle mass, [kg]
μ	fluid shear viscosity, [Pa·s]
N_s	number of spheres, [-]
N_c	number of tetrahedral cells, [-]

Ω	full domain of the three-phase problem, [m ³]
Ω_i	domain defined by tetrahedron i , [m ³]
Ω_{ij}	union of tetrahedra Ω_i and Ω_j , [m ³]
$\dot{\omega}_i$	particle rotational acceleration, [m/s ²]
Φ	part of Ω occupied by the Nonwetting phase (Nonwetting pores), [m ³]
Φ_i	part of Ω_i occupied by the Nonwetting phase (Nonwetting pore), [m ³]
ϕ'	the angle of shearing resistance, [-]
p^c	capillary pressure, [Pa]
$\overline{p^c}$	normalized capillary pressure, [-]
p_e^c	entry capillary pressure, [Pa]
p_i	fluid pressure in tetrahedron i , [Pa]
p^n	nonwetting phase pressure, [Pa]
p^w	wetting phase pressure, [Pa]
ϕ	porosity, [-]
Q_{ij}	the total volumetric flux from i to j , [m ³]
r^c	the radius of curvature of Nonwetting-Wetting interface (pore throat radius), [m]
r_e^c	entry pore throat radius, [m]
ρ_f	local density of the fluid, [kg/m ³]
S_{ij}	the common facets of tetrahedra Ω_i and Ω_j , [m ²]
s^n	nonwetting phase saturation, [-]
s^w	wetting phase saturation, [-]
s_{sub}^w	wetting phase saturation of a subdomain, [-]
$\overline{s^w}$	micro-scale wetting phase saturation, [-]
σ_{ij}^c	contact stress between particles, [Pa]
σ_{ij}	total stress, [Pa]
σ'_{ij}	effective stress, [Pa]
σ_{ij}^{net}	net stress, [Pa]
τ	shear strength, [Pa]
Θ	part of Ω occupied by the Wetting phase (Wetting pores), [m ³]
Θ_i	part of Ω_i occupied by the Wetting phase (Wetting pore), [m ³]
V_t	the total or bulk volume of material, [m ³]
V_v	the volume of void pore space, [m ³]
V_w	the volume of wetting phase fluid, [m ³]
v	the average velocity of the fluid, [m/s]
∂X	contour of domain X, [m ²]
$\partial^w X$	part of contour of X intersecting (or in contact with) the Wetting phase, [m ²]
$\partial^s X$	part of contour of X intersecting (or in contact with) the Solid phase, [m ²]
x_i	particle position, [m]
\dot{x}_i	particle velocity, [m/s]
\ddot{x}_i	particle acceleration, [m/s ²]

Abstract

The situation of two immiscible fluids flow through a deformable granular material is widely encountered in nature and in many areas of engineering and science. To understand the physical evolution of the multiphase system is of great importance for the applications. It requires the knowledge of all component phases, their distribution and interactions. A pore-scale coupled hydromechanical model is presented in this thesis based on previous work, aiming at simulating the quasi-static drainage of deformable granular materials. The model combines a pore network approach and the discrete element method (DEM) for the fluids and grains, respectively. A local criterion for determining the local movements of the fluids interfaces established to approximate the role of the local pore geometry on capillarity and namely on the forces exerted on the solid grains inside each pore. Special attentions have been paid to the entrapment events of the receding fluid and to the preferential invasion along the boundaries. The model is validated through comparisons with experimental results (water retention curves). We apply the model for examining two issues: (1) finite size effects and the concept of representative elementary volume (REV); (2) Bishop's effective stress parameter χ and the relationship between macro-scale effective stress and micro-scale contact stress. Finally, an extension to the pendular regimes is proposed and first results are presented and analyzed.

Key words: granular material, hydromechanical coupling, pore network, two-phase flow, drainage, unsaturated granular materials, discrete element method, effective stress

Résumé

Les situations où deux fluides non miscibles sont présents dans un matériau granulaire déformable sont largement rencontrées dans la nature et dans de nombreux domaines de l'ingénierie et de la science. Comprendre l'évolution de tels systèmes multiphasés nécessite la connaissance de toutes les phases, leur distribution et interactions. Un modèle micro-hydrromécanique couplé est présenté dans cette thèse sur la base de travaux précédents, visant à simuler le drainage quasi-statique de matériaux granulaires déformables. Il combine une approche de type réseau de pores et la méthode des éléments discrets (DEM) pour les fluides et les grains respectivement. Un critère local de mouvement d'interfaces fluides est établi, afin d'approximer au mieux le rôle de la géométrie porale sur les phénomènes capillaires et notamment les forces exercées sur les grains solides à l'intérieur de chaque pore. Une attention particulière est dédiée aux événements de piégeage du fluide drainé et à l'invasion préférentielle le long des bords du domaines. Le modèle est valide par la comparaison avec des résultats expérimentaux (courbes de rétention d'eau). Nous appliquons le modèle pour étudier deux questions: (1) les effets de taille finie et à la question du volume élémentaire représentatif (REV); (2) le paramètre de contrainte effective de Bishop et la relation entre contrainte effective macroscopique contrainte de contact micro-mécanique. Finalement, une extension du modèle au régime pendulaire est présentée et des premiers résultats sont présentés et discutés.

Mots clés: matériau granulaire, couplage hydrromécanique, réseau de pores, écoulement biphasique, drainage, saturation partielle, méthode des éléments discrets, contrainte effective

General Introduction

The situation of two immiscible fluids flow through a deformable granular material is widely encountered in nature and in many areas of engineering and science. This includes the soil mechanics, ground water hydrology, petroleum engineering, food industry, biomedical technology, etc. To understand the physical evolution of the multiphase system is of great importance for the applications. It requires the knowledge of all component phases, their distribution and interactions.

The motion of the fluid phases of the system is termed as two-phase flow in hydromechanics, in which the flow includes the movement of each individual fluid and the movement of the fluid-fluid interface. In the quasi-static regime, the flow can be simplified to the motion of the interface only and viscous effects can be neglected. One-phase flow can be described by Darcy's law and the generic motion of the fluid can be formulated by the Navier-Stokes equations. The difficulties arise when describing two-phase flow in the complex space of porous media. The microscopic interactions between the two fluids cause local fluctuations. As a consequence, one fluid may be replaced or entrapped by another fluid, finally. How to define such local fluctuations depend on not only the properties of the fluids themselves but also the properties of the space (i.e., boundary conditions). As a solution, pore-scale models can idealize the space as a network of pore bodies connected by narrow throats. Then the local criteria can be defined to formulate the local fluctuations associated to the pores. A proper network should decompose the space in a natural and simple way and preserve its geometrical characteristics. A decent local criteria should balance the accuracy and the efficiency, especially, when the fluid space may be changed due to the deformation of the solid skeleton.

Considering the solid phase, unsaturated soil is a special case of the multiphase system. The deformation or other mechanical behaviors of the soil are usually related to the definition of the effective stress. The classical continuum-based methods usually treat the effects of the fluids following empirical relations, namely, suction - saturation curves and their evolution with strain, relative permeability, and effective stress. At micro-scale, the motion of single solid grain is formulated by Newton's law of motion. Assigning a proper contact definition between the neighboring grains, we can obtain the macro-scale deformation. The discrete element method (DEM) provides a relevant framework in modeling such evolution. Considering the effects of the fluids on a single solid particle at the micro-scale, we need to formulate the fluid forces acting on this particle in terms of fluids pressure and interfacial tension. Thus a direct link should be established between the motion of the fluids and the properties of the solid grains.

To conclude, solving coupled flow-deformation problems need to map a network on a given set of solid grains. The mechanical coupling requires a direct and explicit link between the network geometry and the positions of the solid grains, and the computational

cost of updating the network should be kept as small as possible. Recently, a pore-scale approach has been found to be an effective approach for simulating hydromechanical couplings in deformable porous media with one-phase flow of a pore fluid (Chareyre et al., 2012; Tong, A.T. et al., 2012; Catalano et al., 2014; Scholtès et al., 2015). Therein, the basic idea was to combine the discrete element method (DEM) and a pore-scale model for, respectively, the granular solid phase and a viscous pore fluid. Termed PFV-DEM (PFV for “pore-scale finite volumes”) the coupling was applying concepts coming from the pore-network methods to a Lagrangian mesh following the movements of the solid particles, allowing the simulation of mechanical responses of Representative Elementary Volumes (REV) of porous solids. This is the cornerstone of the thesis.

In this work, we will propose a pore-scale hydromechanical coupled model for partially saturated porous media, termed as “2PFV-DEM” (two-phase pore-scale finite volume - discrete element method) model. It is designed specifically for simulating the quasi-static two-phase flow of drainage through deformable granular materials. The coupling scheme is similar to the strategy of PFV-DEM, where the actions of the fluids are represented by a network and the motion of solid phase is handled by DEM. The quasi-static flow is expressed by a sequence of individual equilibrium states, in which the motion of the fluids interface is highlighted. Special attention will be paid to the local criterion, i.e., the determination of a local threshold value. We focus on the faithful approximation of phases geometry and of the fluid pressures and interfacial tension acting on solid grains within each pore, and on the displacement of interfaces during drainage.

Two special features will be implemented in the model with respect to the reality of drainage phenomena and experimental setup. (I) In short-term, the receding fluid is allowed to be trapped by the invading fluid without motion. It will lead to the localizations in terms of fluid pressure and saturation. In long-term, the receding fluid is drained completely. (II) A preferential invasion along the boundaries of the sample is allowed with respect to the observations of some micro-scale experiments.

We will apply this model to solve two issues.

- Finite size effects. Microscale imaging techniques together with pore scale numerical models are promising tools for gaining insight into the governing mechanisms of two-phase flow in such systems. However, both experimental techniques and computational methods have severe limitations in terms of sample size, which raises questions about possible finite size effects. We will apply the model to assess the size effects and boundary effects with a series of primary drainage tests.
- Effective stress. The concept of effective stress is one of the fundamental concepts of soil science. The expression of effective stress for unsaturated soil (or the stress frameworks for unsaturated soil) is still not clear. For granular materials, how to build the link between the micro-stress/contact stress and effective stress is a hot topic. In the survey, we will follow Bishop’s expression to examine the relations between Bishop’s parameter and saturation from macro and micro points of view.

As an extension of the model, we will combine the liquid bridge model of pendular regime (Scholtès et al., 2009; Scholtès et al., 2009a; Chalak, 2016) with the current implementa-

tion. The capillary effects of the liquid bridge will be examined in terms of the saturation of the fluid and the deformation of the solid skeleton.

This thesis is organized in seven chapters grouped in three parts.

Part I introduces primarily the reader to the physics and mechanics of partially saturated granular material. The properties of the fluid phases are introduced based on the knowledge of two-phase flow in hydrology, where the algorithm and numerical methods are also reviewed (chapter 1). In chapter 2, the multiphase system is treated as the special case of unsaturated soil. The mechanical behaviors of the solid skeleton are reviewed. The stress framework and constitutive modeling of unsaturated soil are discussed.

part II concerns the description of the 2PFV-DEM coupled model, organized in two chapters. A first one (chapter 3) presents the details of the model, where the governing equations, drainage criteria and the coupling with the DEM are elaborated. A second one (chapter 4) shows the implementation of the model, which is based on an open-source code YADE platform. The functions of the model are presented by a simple test. A validation follows.

part III presents the applications and extension of the model. Chapter 5 focus on the issues related to size effects and boundary effects. Chapter 6 is devoted to the examination of Bishop's effective stress parameter χ , where the relations between macro-scale effective stress and micro-scale contact stress are investigated as well. The last chapter presents the extensions, where the liquid bridge model of pendular regime is extended into the current implementation.

Part I
Literature Review

Abstract

The study of the physics of fluid/fluids through deformable granular materials is of great importance in many areas of engineering and science, which include the soil mechanics, ground water hydrology, petroleum engineering, food industry, biomedical technology, etc. It covers a wide range of applications at different space-scales and time-scales, from the macro-scale such as oil recovery ($10^3 - 10^5$ m) to micro-scale such as biological systems ($10^{-5} - 10^{-3}$ m), and from long-time scale such as the organic contaminant dissolution study (longer than many decades) to short-time scale such as the “Haines jump” phenomenon in pore space (within few seconds). In all of these systems, the aggregate of porous media consists of the solid skeleton and two or more immiscible fluids. For different communities of science, the researchers may focus on different aspects of the complex aggregate system. For instance, in soil mechanics, the researchers term the aggregate materials as “unsaturated soils”, in which “unsaturated” is used for illustrating the degree of pore water saturation. They are mainly interested in the mechanical behaviors of the solid skeleton. On the other hand, the scientists in fluid mechanics mainly focus on the hydraulic behaviors of the fluid/fluids of the pore space, such as the pressure and distribution of the fluids. Also, in different communities, the same physical phenomenon or variable may be described by different terminologies, for example, the matric suction and capillary pressure are both used for describing the difference in pressure across the interface between two immiscible fluids.

In the thesis, we aim to model the physical interactions between the solid phase and two immiscible fluid phases. The properties of all components are equally important to us. Thus, the literature review is twofold. We will separately review the physics and mechanics of different components of the granular porous media, in which the theory behind the fluids is mainly from the community of hydrology and the properties of the solid phase is in the context of soil science.

Chapter 1

Two-phase flow in granular porous media

1.1 Physics of two-phase flow

In fluid mechanics, two-phase flow is a flow involving two immiscible fluids usually in a pipe. It is a particular example of multiphase flow. Two-phase flows in granular porous media are almost universally encountered in nature and in various applications of mechanical engineering and industry, such as the air/water fluids in unsaturated soil, water/oil fluids or water/gas fluids in petroleum engineering, blood/other body fluid in biochemical engineering, etc. To understand and model the physics of the interactions between fluid, fluid and solid phases is of great importance for such applications. The difficulty lies in the complex structure of the pore space constituted by the discrete (deformable and poly-disperse) solid phase, in which the hydraulic boundary conditions can not be accurately determined. Even though the fluids through a single pipe is given by simple equations, the network of the pipes is impossible to know in detail.

1.1.1 Solid structure and one-phase flow

Two important quantities are usually used to describe the properties of the granular porous medium: the porosity ϕ and the permeability κ .

$$\phi = \frac{V_v}{V_t} \quad (1.1)$$

where V_v is the volume of void pore space and V_t is the total or bulk volume of material, including the solid and void components. The void space of the medium can be artificially decomposed into pore bodies (large voids) connected by pore throats (narrow voids). The geometrical idealization of the pore body and the pore throat in numerical implementation (mainly related to pore scale approaches) will be reviewed in next section. The permeability describes the ability of a porous material to allow fluid to flow through it. It is related to the porosity, the shapes of the pores and the level of connectedness, i.e., the geometry of the medium. Permeability is a property of the porous media only, not the fluid. The proportionality constant for the fluid through a porous media is termed as hydraulic conductivity. It depends on not only the geometry of solid structure (i.e., intrinsic

permeability) but also the property and the amount of the fluid.

Consider flow of one fluid through a porous medium, the dynamic property of the fluid can be characterized by the dynamic viscosity μ . It measures the local resistance of the fluid to the rate of shear strain. The flow phenomena is formulated by Darcy's law,

$$\mathbf{u} = -\frac{\kappa}{\mu}(\nabla p - \rho \mathbf{g}) \quad (1.2)$$

where \mathbf{u} is the flux and ∇p is the pressure gradient vector. Darcy's law is only valid for slow, viscous flow (typically flows with a Reynolds number less than one).

The generic motion of fluid can be described by the Navier-Stokes (N-S) equations. These equations are established by applying Newton's second law to fluid motion, together with the assumption that the fluid stress is the sum of a diffusing viscous term and an isotropic pressure term. The N-S equations for irrotational flow can be written as:

$$\frac{\partial \rho_f}{\partial t} + \nabla \cdot (\rho_f \mathbf{u}) = 0 \quad \text{Continuity Equation} \quad (1.3)$$

$$\frac{\partial \mathbf{u}}{\partial t} + (\mathbf{u} \cdot \nabla) \mathbf{u} = -\frac{1}{\rho_f} \nabla p + \mathbf{F} + \frac{\mu}{\rho_f} \nabla^2 \mathbf{u} \quad \text{Equation of Motion} \quad (1.4)$$

$$\rho_f \left(\frac{\partial \zeta}{\partial t} + \mathbf{u} \cdot \nabla \zeta \right) - \nabla \cdot (K_H \nabla T) + p \nabla \cdot \mathbf{u} - \mu \nabla^2 \mathbf{u} = 0 \quad \text{Conservation of Energy} \quad (1.5)$$

where ρ_f =local density of the fluid, \mathbf{u} =flow velocity, \mathbf{F} =external force per unit mass, p =pressure of the fluid, ζ =thermodynamic internal energy, K_H =heat conduction coefficient and $\frac{\partial}{\partial t}$ refers to the time rate of change at a fixed point in the fluid. Usually, the N-S equations are too complicated to be solved in a closed form. However, some special cases can be simplified and derived. For instance, in case of incompressible fluids (constant ρ_f), the Continuity Equation reduces to:

$$\nabla \cdot \mathbf{u} = 0 \quad (1.6)$$

1.1.2 Two-phase flow

For the system of immiscible two-phase flow in a porous medium, each of fluids is considered to have a separately defined volume fraction and velocity field. The flow includes not only the movement of each individual fluid phase itself but also the movement of the interfaces between different phases. The contact angle quantifies the wettability of the solid phase surface to the fluid phases through the Young equation. From the contact angle, one can tell which fluid is nonwetting phase (NW-phase) and which fluid is wetting phase (W-phase) relative to the solid phase (S-phase). If the NW-phase invades the pore space and displaces the W-phase, this procedure is termed as "drainage" (for instance, the drying process in soil science); and if the flow is in opposite sequence, it is referred as "imbibition". The difference between NW-phase pressure p^n and W-phase pressure p^w is termed "capillary pressure" p^c , i.e., $p^c = p^n - p^w$. The force acting on the NW/W interface is referred as "capillary force".

Dynamic characteristics

The dynamic properties of the two-phase flow systems can be described by two dimensionless numbers, the capillary number C_a and the viscosity ratio M ,

$$C_a = \frac{\mu v}{\gamma}, \quad M = \frac{\mu_{inv}}{\mu} \quad (1.7)$$

where μ_{inv} is the viscosity of the invading phase, μ is the viscosity of receding phase, v is the average velocity of the receding phase, and γ is the interfacial tension between the two fluid phases (Lenormand et al., 1988; Lenormand, 1990). If C_a is very small (usually said less than 10^{-5}), the flow is dominated by capillary forces whereas for high value of C_a the capillary forces are negligible compared to the viscous forces. It is worth noting that C_a is usually considered as a macroscopic parameter, which can not be applied at pore scale. That is because the velocity of fluids can be significantly different at macro-scale and pore-scale (Lu et al., 1995; Joekar-Niasar and Hassanizadeh, 2012).

The viscosity ratio, which is determined by the types of fluids ($M > 1$, referred as favorable; $M < 1$, referred as unfavorable), can affect the characteristics of the flow and the entrapment of the fluid. Fig.1.1 illustrates the displacement of a W-phase by a NW-phase (i.e., drainage) in the absence of buoyancy forces at different C_a and M . Several flow regimes can be observed. If C_a is small and M is favorable, the NW-phase distributes in the form of capillary fingering (Fig.1.1a); if C_a is large and M is favorable, a stable front can be observed (Fig.1.1c). For unfavorable M , viscous fingering occurs (Fig.1.1b) and the invasion front is not stable if larger pressure gradient is applied (Vizika et al., 1994; Joekar-Niasar and Hassanizadeh, 2012).

States of fluid content

Let us consider a typical two-phase flow system in soil mechanics, i.e., water/air/soil, in which we assume the water is the W-phase and the air is NW-phase. It is well known the cohesion of the soil depends on the amount of water in the system. Also the water may exist in the pore space with different geometrical shapes (i.e., mensici) if its content varies. Thus a qualitative classification of the liquid content is commonly made. The following four regimes have been distinguished (Newitt and Conway-Jones, 1958; Iveson et al., 2001; Mitarai and Nori, 2006),

- **Pendular regime:** At low moisture level, the particles are held together by lens-shaped rings of liquid (liquid bridge).
- **Funicular regime:** Liquid bridges around the contact points and liquid-filled pores coexist. Both contribute to the cohesion of the medium.
- **Capillary regime:** Most pores are filled with the liquid, but the liquid bridges and clusters of isolated liquid also exist. The air pressure is larger than liquid pressure, thus the capillary pressure still results in a cohesive interaction between particles.
- **Slurry regime:** The liquid pressure is equal to, or higher than, the air pressure. No cohesive interaction appears between particles.

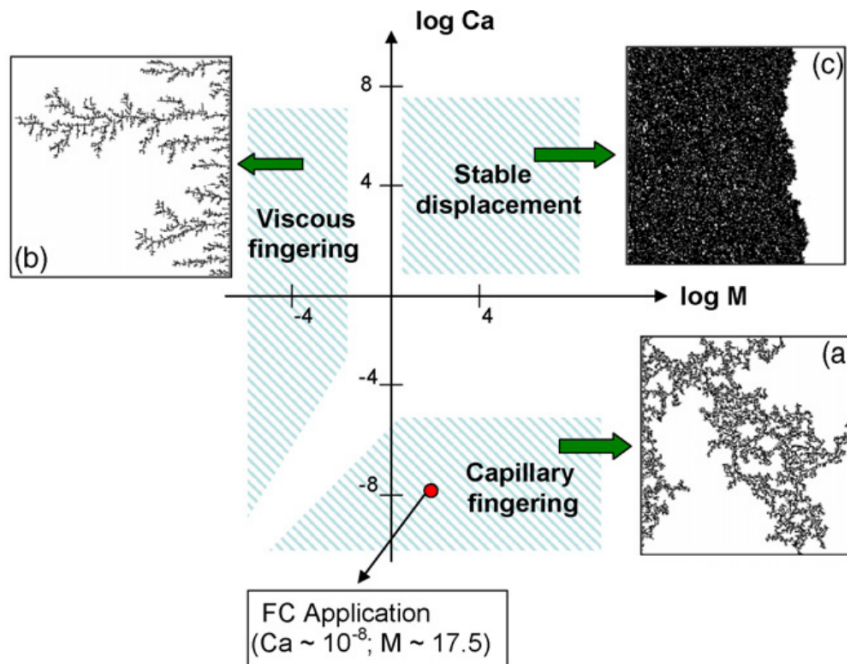


Figure 1.1: Schematic representation of phase diagram showing various flow regimes under different viscosity ratio and capillary number, after Joekar-Niasar and Hassanizadeh (2012), originally based on Lenormand (1990); Lenormand et al. (1988); Sinha and Wang (2007)

So far only the pendular regime has been investigated systematically from a micromechanical point of view. We will review this in next section.

In the thesis, since we also want to implement the pendular regime into the model, the algorithm of pendular regime will be recalled briefly. We will present this in chapter 7.

1.2 Numerical models for two-phase flow in (deformable) porous media

As reviewed in previous section, Darcy's Law and N-S equations formulate the physics of one-phase flow at different scales, which are essentially based on the similar conservation theory of macroscopic properties (i.e., mass, momentum, energy, etc.). Consequently, researchers tried to apply such theory on two-phase flow. The main difficulty is how to describe the local fluctuations induced by the microscopic interactions between the two fluids (capillary force dominated or viscous force dominated). The movement of one fluid affects the boundary conditions of the other fluid. Moreover, if the structure of the porous media is deformable, the coupling scheme will be extremely complicated.

In general, there are several approaches at three different scales available for simulating two-phase fluid flows (including the solid-fluids couplings).

1.2.1 Macro-scale continuum models

Macro-scale continuum models are used to solve the pressure and the saturation of wetting or nonwetting phases in most field-scale applications. By following the conservation theory, the local fluctuations at microscale in two-phase flow have been formulated in a variety of ways, mostly incorporated in Darcy's Law. The Buckley-Leverett theory is the famous one of them. It follows the mass conservation and assumes that the capillary pressure is a function of water (W-phase) saturation only, and the flow is linear and in steady-state (Buckley et al., 1942). As summarized by Joekar-Niasar and Hassanizadeh (2012), the following system of equations should be solved for a rigid porous medium and incompressible two-phase flow in the framework of Buckley-Leverett theory,

$$\phi \frac{\partial s^\alpha}{\partial t} + \nabla \cdot \mathbf{u}^\alpha = 0, \quad \alpha = n, w \quad \text{mass balance} \quad (1.8)$$

$$\mathbf{u}^\alpha = -\frac{1}{\mu^\alpha} k^\alpha \mathbf{K} (\nabla p^\alpha - \rho^\alpha \mathbf{g}), \quad \alpha = n, w \quad \text{Darcy's Law} \quad (1.9)$$

$$s^w + s^n = 1 \quad \text{pore volume conservation} \quad (1.10)$$

$$p^c = p^n - p^w = f(s^w), \quad dp^c/ds^w = 0 \quad \text{Buckley-Leverett's assumption} \quad (1.11)$$

where ϕ = porosity, s^α = the saturation of phase α , \mathbf{u}^α = velocity of phase α , μ^α = viscosity of phase α , k^α = the relative permeability of phase α , \mathbf{K} = intrinsic permeability tensor, and w and n refer to the wetting and nonwetting phases.

In hydrodynamics, the researchers mainly focus on the evolution of flow of the fluids, and are rarely interested in the deformation of the porous medium for macro-scale modeling. The majority of work about solid-fluids couplings is usually found in soil science, which will be reviewed in the next chapter. Those coupling schemes are based on empirical relations describing, namely, capillary pressure - saturation ($p_c - s_w$) curves and their evolution with strain, relative permeability, and effective stress. Such methods have acceptable computational costs for large problems, but the empirical laws therein have well known issues. Namely, hysteretic effects are very difficult to model and an accepted effective stress framework is still absent.

1.2.2 Micro-scale continuum methods

The micro-scale continuum methods, which include lattice Boltzmann method, volume of fluid method, smoothed particle hydrodynamics method and level set method, do not rely on such empirical relations. They are promising approaches for getting accurate results at very small scales and gaining understanding of the phenomena observed at the macroscale. However, they usually have high computational cost.

Lattice Boltzmann method

Lattice Boltzmann method (LBM) (or thermal lattice Boltzmann method (TLBM)) is a relatively new approach for simulating fluid flows and modeling physics of fluids in computational fluid dynamic (CFD). Unlike conventional CFD methods, which are based on discretization of macroscopic continuum equations (i.e., mass, momentum, and energy), LBM is based on microscopic models and mesoscopic kinetic equations (Chen and

Doolen, 1998). It is assumed that the fluid consists of fictive particles, and such particles perform consecutive propagation and collision processes over a discrete lattice mesh. In recent decade, Considerable work has been made through LBM to solve the problems related to two-phase or multi-phase flow. For instance, Gunstensen et al. (1991) proposed a multi-component LBM on the basis of two-component lattice gas model; Shan and Chen (1993) developed a LBM model with mean-field interactions for multi-phase flow; Swift et al. (1996) proposed a LBM model based on the free-energy approach, etc. In addition, the LBM has several computational advantages over other conventional CFD methods, including parallelization of the algorithm (Chen and Doolen, 1998), handling complex boundary conditions (Noble et al., 1995; Zou and He, 1997; Chen and Doolen, 1998; Mei et al., 1999), incorporation with microscopic interactions and simplicity of programming. Of course, some limitations are still blocking the implementation of LBM, namely, it is difficult to simulate the flows with high-Mach number and a consistent thermo-hydrodynamics scheme is still missing.

Volume of fluid method

Volume of fluid (VOF) method belongs to the class of Eulerian methods, first proposed by Hirt and Nichols (1981). In VOF, a scalar indicator function between zero and one, termed as volume fraction is employed to distinguish between two different fluids. Thus the free surface (i.e., fluid-fluid interface) can be tracked and located. However, VOF is not a standard method for solving flow problems. The N-S equations usually need to be incorporated to describe the motion of the flow of each fluid. VOF usually does not need high computational cost and programming friendly. Several models have been established by combining different flow solvers in the framework of VOF (Gueyffier et al., 1999; Welch and Wilson, 2000; Gopala and van Wachem, 2008; Raeini et al., 2012).

Smoothed particle hydrodynamics method

Smoothed-particle hydrodynamics (SPH) is a mesh-free particle method based on Lagrangian formulation. The underlying idea is to decompose the fluid into a set of discrete elements (termed as “particles”) with a spatial distance (termed as “smoothing length”). Their properties are described by a kernel function (Liu et al., 2003; Fulk and Quinn, 1996). The governing equations are established based on these discrete particles to compute the local physical variable (density, velocity, acceleration, etc.). The motion of the fluids is represented by the motion of particles, thus the fluid-fluid interface is not explicitly tracked and located. In recent years, extensive applications have been made in a wide range of areas of engineering and science, including the two-phase flow of hydrodynamics (Monaghan and Kocharyan, 1995; Morris, 2000; Colagrossi and Landrini, 2003; Tartakovsky and Meakin, 2005, 2006). The main disadvantage of SPH is that it requires large numbers of particles to reproduce the physical phenomena at the same scale, which makes the computational cost relatively expensive.

Level set method

The level set methods (LSMs), introduced by Osher and Sethian (1988), are computational techniques for tracking and analyzing the motion of an interface in two or three

dimensions. In LSM, the interface is represented by the zero contour of a signed distance function, termed as the level set function. The motion of the interface is governed by a differential equation for the level set function. LSM can automatically track the topological changes and obtain high order of accuracy. Thus, they are suitable for implementations in simulating the physics of two-phase flow (Sussman et al., 1994, 1999; Olsson and Kreiss, 2005; Di et al., 2007). The drawback of LSMs is that they are not conservative. For incompressible two-phase flow, loss or gain of mass might happen.

There are still many other micro-scale continuum methods that have not been reviewed in this section (for instance, front tracking method). In general, most of above methods also mainly focus on the motion of the fluids, rarely modeling the interactions between fluids and solid structure.

1.2.3 pore-scale methods

The third category of methods for simulating the two-phase flow is the family of pore-scale approaches. Pore-network models are the majority. Pore-network models introduce an intermediate scale at which pore bodies are identified. They enable the simulation of larger domains compared to micro-continuum models. They idealize the porous medium as a network of pore bodies connected by narrow throats. Pore-network modeling was pioneered by Fatt (see Fatt (1956) and companion papers), who derived capillary pressure and saturation ($p_c - s_w$) curves of primary drainage and computed pore size distributions in a network of interconnected pores. Since then, a number of different researchers have contributed to the current understanding of two-phase flow using pore-network models.

Network topology and geometry

Pore network models represent the continuous interconnected pore space by discrete networks of pores and throats. The topology is mathematically concerned with the properties of the pore space that are preserved under continuous deformations. It can be defined by two characteristics (Joekar-Niasar and Hassanizadeh, 2012): (1) the spatial location of pore bodies and (2) the connectivity of pore elements. Consequently, four categories of network topologies can be distinguished: structured regular (in majority), structured irregular (e.g., Koplik and Lasseter, 1985; Mogensen and Stenby, 1998), unstructured regular (e.g., King, 1987; Blunt and King, 1991) and unstructured irregular (very few), as illustrated in Fig.1.2.

Beside the topology, the geometries of pore bodies and throats can also affect the hydraulic behavior of the system. Two porous media with the same topology can have significant different properties (Joekar-Niasar et al., 2010b). The shape of the pores have been approached by regular geometries (e.g., cubic (Joekar-Niasar et al., 2010a; Raouf and Hassanizadeh, 2013) or spherical (Koplik and Lasseter, 1985)) and the shape of the pore throats by cylinders with various cross-sectional shapes (e.g., circular (Dias and Payatakes, 1986; Koplik and Lasseter, 1985) or triangular (Al-Gharbi and Blunt, 2005)) or with parallel pipes (Hughes and Blunt, 2000; Joekar-Niasar et al., 2010a). Angular cross sections have been proposed by some authors to reflect the phenomena of corner flow and the crevices occupied by the wetting phase. Statistically representative pore networks of

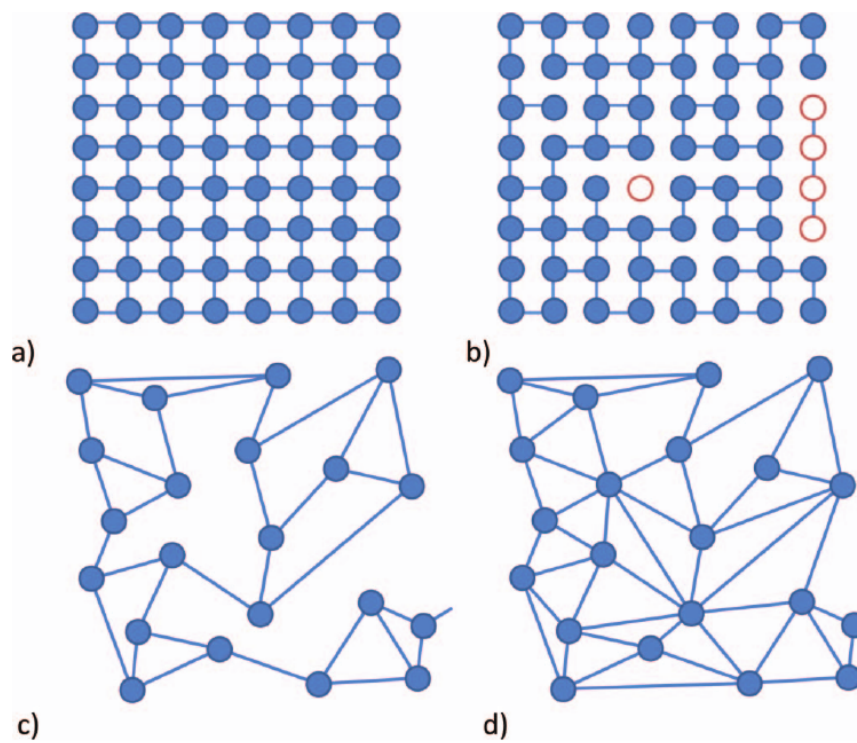


Figure 1.2: Classification of pore network topologies: (a) structured regular, (b) structured irregular (red color illustrates isolated pores), (c) unstructured regular, and (d) unstructured irregular, after Joekar-Niasar and Hassanizadeh (2012).

this kind can be generated to represent real porous samples (Khaksar et al., 2013; Rostami et al., 2015; Nikooee et al., 2014).

Other work focuses on mapping directly the pore space of real granular materials, a problem pioneered by Bryant and Blunt (Bryant and Blunt, 1992) (see also Bryant et al., 1993a,b), who constructed a network mapping an experimental specimen of packed mono-sized spheres. As imaging techniques reach smaller and smaller scales (Culligan et al., 2004; Khaddour et al., 2013), there is a growing interest in this problem and many pore-network extraction algorithms are being developed. They include the multi-orientation scanning method (Zhao et al., 1994), medial axis-based algorithms (Lindquist et al., 1996; Sheppard et al., 2005; Prodanović et al., 2006), Delaunay/Voronoi diagram-based methods (Bryant and Blunt, 1992; Øren and Bakke, 2003), or the method of maximal ball (Silin et al., 2003; Silin and Patzek, 2006)).

Solving coupled flow-deformation problems similarly requires to map a network directly on a given set of solid particles. Moreover mechanical coupling requires a direct and explicit link between the network geometry and the positions of the solid grains, and the computational cost of updating the network should be kept as small as possible. The Delaunay/Voronoi methods, which introduce a simple duality between the solid element and the void space, are suitable for such implementation. The very few existing models coupling a pore-network with a deforming material also adopted this methodology (in two dimensions (Jain and Juanes, 2009; Kharaghani et al., 2012), hence mainly qualitative).

A three-dimensional pore-scale approach termed *PFV* (Chareyre et al., 2012) has been proposed to effectively solve flow problems with a single fluid phase. Therein, the fluid flow was modeled using a pore-scale finite volume scheme (PFV) which shares many features with conventional pore-network methods. The method has proven effective in the context of coupled flow-deformation problems (Tong, A.T. et al., 2012; Catalano et al., 2014; Scholtès et al., 2015).

Algorithms

The conservation equations Eq.1.8-1.11 in the framework of Buckley-Leverett theory can formulate the physics of two-phase flow at macro-scale, but they are not suitable for the pore-scale modeling. A consistent adaptation is required. Joekar-Niasar and Hassanizadeh (2012) classified the approaches for solving two-phase flow into two general categories: single-pressure algorithm and two-pressure algorithm, assuming the flow in the pore throat has low Reynolds number (i.e., the inertial effects are negligible) and the solid structure is rigid. In single-pressure models, each pore body or throat can be occupied by only one fluid phase, thus only one pressure is assigned. (Although the pore body or throat may be occupied by both fluids, an equivalent single fluid with single pressure is introduced); In two-pressure models, a pore body is allowed to be filled by two fluids with individual pressure, i.e., a local capillary pressure can exist in a pore. Subsequently, Joekar-Niasar and Hassanizadeh (2012) summarized the adaptation of Buckley-Leverett's framework for pore scale models as follows,

(1) For single-pressure models, a pore body i connects to a pore body j through a pore

throat ij ,

$$V_i \frac{\partial s_i^w}{\partial t} + \sum_{j=1}^{N_i} Q_{ij} = 0 \quad \text{mass balance} \quad (1.12)$$

$$Q_{ij} = K_{ij} \Delta_{ij}, \quad \Delta_{ij} = f(p_i^n, p_j^n, s_i^w, s_j^w, p_{ij}^c) \quad \text{Darcy's Law} \quad (1.13)$$

$$s_i^w + s_i^n = 1 \quad \text{pore volume conservation} \quad (1.14)$$

$$p_{ij}^c = f(r_{ij}), \quad Q_{ij} = 0 \quad \text{if} \quad p_i^n - p_j^w < p_{ij}^c \quad (1.15)$$

where V_i is the volume of pore body i , s_i^w , s_j^w are the wetting saturation of i and j , Q_{ij} is the total volumetric flux from i to j , $K_{ij} [M^{-1}L^4T]$ is the equivalent hydraulic conductivity as a function of the pore throat radius, pore throat length and fluid viscosities. Δ_{ij} is related to the pressures of pore bodies i , j and throat ij (Koplik and Lasseter, 1985; van der Marck et al., 1997), p_{ij}^c is the entry capillary pressure of pore throat ij . r_{ij} is the radius of pore throat ij .

(2) For two-pressure models, a pore body i is filled by two fluids,

$$V_i \frac{\partial s_i^\alpha}{\partial t} + \sum_{j=1}^{N_i} Q_{ij}^\alpha = 0, \quad \alpha = n, w \quad \text{mass balance} \quad (1.16)$$

$$Q_{ij}^\alpha = K_{ij}^\alpha (p_i^\alpha - p_j^\alpha), \quad K_{ij}^\alpha = f(p_{ij}^c), \quad \alpha = n, w \quad \text{Darcy's Law} \quad (1.17)$$

$$s_i^w + s_i^n = 1 \quad \text{pore volume conservation} \quad (1.18)$$

$$p_i^c = p_i^n - p_i^w = f(s_i^w) \quad (1.19)$$

where K_{ij}^α is the hydraulic conductivity for phase α .

In the thesis, the method we will propose belongs to the single-pressure algorithm. One important issue in the method is how to solve the entry capillary pressure of pore throat, p_{ij}^c . Considering a pore body occupied by W-phase, the nonwetting phase can only invade the body through the throat when the local capillary pressure surpass the entry capillary of that throat. Entry capillary pressure can be determined by following the MS-P (Mayer-Stowe-Princen) method, which employs the balance of forces on the NW-W interface (Mayer and Stowe, 1965; Princen, 1969). The balance can be written as,

$$\sum \mathbf{F} = \mathbf{F}^c + \mathbf{F}^t = 0 \quad (1.20)$$

where \mathbf{F}^c is the capillary force acting on the area of W/NW interface and \mathbf{F}^t is the tension force acting on the contact lines between different phases. Based on this method, the entry capillary pressure for throats with different irregular shapes can be obtained (Mason and Morrow, 1991; Ma et al., 1996; Fenwick et al., 1998; Van Dijke and Sorbie, 2006; Joekar-Niasar et al., 2010b). In the thesis, we also employ this approach to calculate the entry capillary pressure of our model, which will be elaborated in next chapter.

Other hydromechanical coupling models at pore-scale

Some models may not focus on the physical interactions between the fluids; instead they take the solid particles as the main objects of study. They employ different modeling

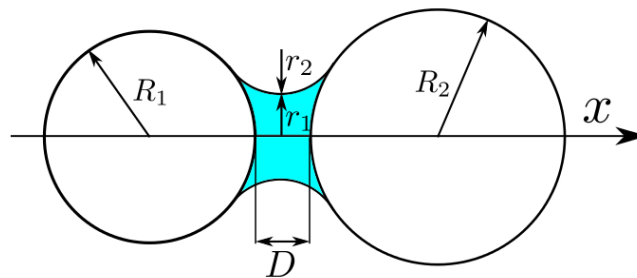


Figure 1.3: Illustration of a liquid bridge between two particles under pendular regime, after Scholtès et al. (2009a).

techniques adopted for the description of fluid flow within the medium, to be then coupled with the DEM. (These models technically belong to the particle scale approaches. We put them into the category of pore scale to review since their scales are at the same level.) The liquid bridge models for describing the pendular regime of fluids are typical ones.

As mentioned in section.1.1.2, in a NW/W/S phases system, namely a air/water/soil system of soil science, the water will exist in the form of liquid bridges between soil particles when the moisture level is low. Such system can be conceptualized as shown in Fig.1.3. The cohesive effects between two soil particles in contact or closed via a pendular bridge arise from the sum of three effects: the water surface tension acting at the water-soil boundary, the force exerted by the capillary pressure in the bridge itself and the buoyancy force resulting from the partial immersion of the particles (Fisher, 1926). The last item is negligible for particles smaller than 1 mm in diameter (Princen, 1968). Quantitatively, the total force is determined by the volume of liquid bridge, surface tension, contact angle and the separation distance between the two particles. Based on the conceptual model of Fig.1.3 (in 2D or 3D), the total force has to be numerically solved using various mathematical methods. The relationships between liquid content, cohesion force and separation distance have also been established. Consequently, the couplings with DEM could be well implemented (Hotta et al., 1974; Ennis et al., 1990; Lian et al., 1993; Li, 2003; Scholtès et al., 2009; Scholtès et al., 2009a).

In the thesis, the model we will propose mainly focuses on funicular regime. But it can be extended to cover the pendular regime with no difficulty. We will present this work in chapter 7, where the algorithm of pendular model will be recalled in detail.

Under the mechanical framework (i.e., based on the geometry and motion of the solid phase), two-phase flow in porous media under the pendular regime has been systematically investigated. The hydromechanical coupling models have been successfully established. However, rarely models related to the funicular regime or the evolution between different regimes can be found, except those developed by Slowik et al. (2009), Kharaghani et al. (2011, 2012). Slowik et al. (2009) proposed a model to describe the evolution from slurry regime to pendular regime (i.e., drying), in which capillary effects are formulated and the induced motion of the solid phase is simulated. This model is constrained in two-dimension, hence mainly qualitative. Kharaghani et al. (2012) proposed two models for simulating the mechanical effects during drying, which mainly reproduced the capillary effects under the funicular regimes. In Kharaghani et al. (2012), an irregular pore network model has been established using Voronoi diagram. The cap-

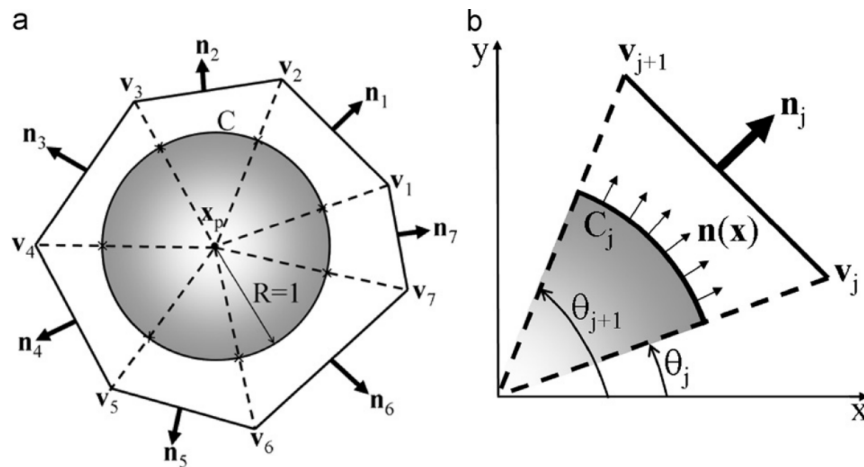


Figure 1.4: Calculation of capillary force based on a Voronoi diagram. (a) A Voronoi cell with projection of vertices on a particle (b) Calculation of a subdomain of the particle, after Kharaghani et al. (2012).

illary force can be accurately calculated based on the network topology (see Fig.1.4), however, this model is also constrained in two dimensions and the solid particles must be monosized. In Kharaghani et al. (2011), a three dimensions model is proposed, but the structure of the solid phase is strictly regular (see Fig.1.5). To our knowledge, no three-dimensional models with polydisperse-sized particles have been developed for simulating the hydromechanical couplings of two-phase flow in porous media.

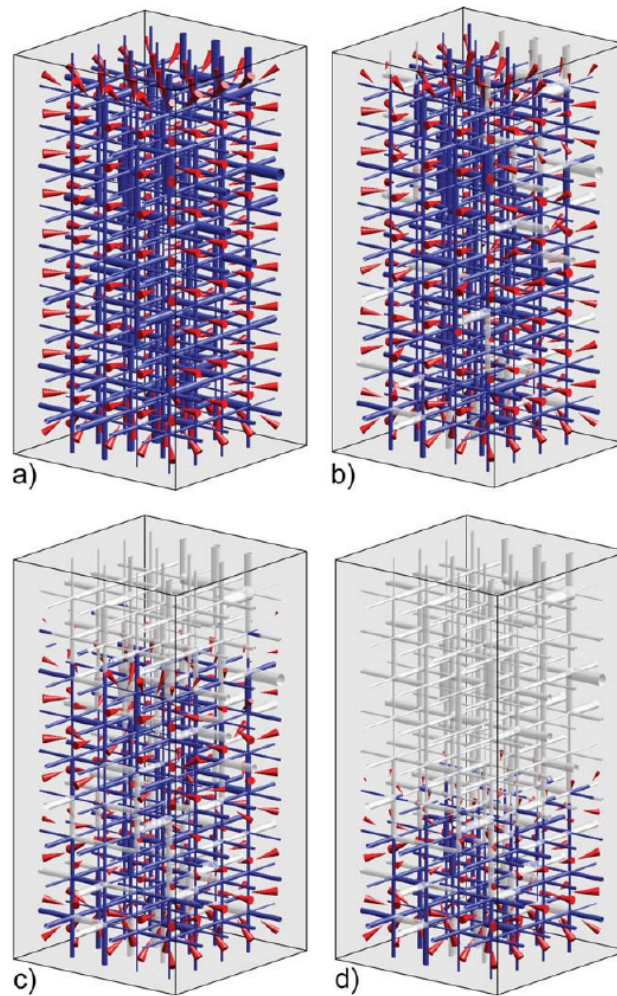


Figure 1.5: Evolution of capillary forces during drying (the viscous effects are negligible). (a) Saturation of W-phase $s^w = 1.0$, (b) $s^w = 0.9$, (c) $s^w = 0.6$ and (d) $s^w = 0.3$. Gray cylinders represent empty pores, and dark blue is for liquid; capillary forces are presented by red cones, and cone size scales with force magnitude, after Kharaghani et al. (2011).

Chapter 2

Physics and mechanics of unsaturated granular materials

2.1 Introduction

In soil mechanics, an aggregate which consists of the solid porous medium and two immiscible fluids is termed “*unsaturated soil*”. The fluid phases are usually air and water. The qualifier “unsaturated” (or alternatively, “partially saturated”) illustrates that the degree of pore water saturation is any value less than unity. We generalize the primary knowledge of unsaturated soil to review the physics and mechanics of unsaturated granular materials.

An unsaturated soil is originally defined as a three phases system, i.e., a certain type of soil, pore water and pore air. The “porosity” (Eq.1.1) is used to measure the void (i.e., “empty”) spaces in the soil. It is one of the primary physical terms for characterizing and classifying the different soils. Considering the water space, the content of pore water can be evaluated by the term of “*water saturation*” or “*degree of saturation*” $s^w(\%)$,

$$s^w = \frac{V_w(100)}{V_v} \quad (2.1)$$

where V_w is the volume of water. For other unsaturated granular materials, the saturation may be referred as the content of different fluids.

Then, the researchers realized that it might be more correct to recognize the existence of a fourth phase in unsaturated soils, namely, the water-air interface or “*contractile skin*” (Fredlund and Morgenstern, 1977) (see Fig.2.1). The most distinctive property of the contractile skin is that it can exert a tensile pull. It behaves like a thin rubber membrane pulling the solid particles together, forming a fixed partition between the air and water phases, and leading to volumetric shrinkage under no changes of total stress while the soil specimen undergoes drying (Fredlund and Rahardjo, 1993). In the four-phase system, the two fluid phases (air and water) continuously flow under the influence of a stress gradient, and the other two phases (solid particles and contractile skin) deform and come to equilibrium under the influence of a stress gradient (Fredlund et al., 2012).

Classical soil mechanics and geotechnical engineering usually treat the solid phase as either dry (pores filled with air, $s^w = 0\%$) or saturated (pores filled with water, $s^w = 100\%$). Unsaturated soil is much more complex, not only because of the existence of two fluid phases in which their distribution and movements are heterogeneous and disorganized, but

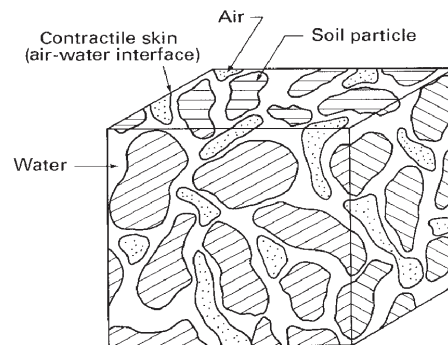


Figure 2.1: Components of unsaturated soil with continuous air phase (Fredlund et al., 2012).

also the effects of contractile skin which make the mechanical behaviors of solid structure unpredictable. By following the theory of saturated soil mechanics, the unsaturated soil mechanics began to emerge during the late 1970s and continues today. As summarized by Fredlund (2005), there are six challenges to the implementation of unsaturated soil mechanics. Two of them are highly related to the numerical modeling,

- To discover appropriate stress state variables for describing the physical behavior of unsaturated soils
- To develop (and test for uniqueness) constitutive relations suitable for describing unsaturated soil behavior

The literature reviews will focus on the above two issues.

2.2 Stress variables

2.2.1 A single effective stress

At early stage of soil mechanics, (Terzaghi, 1936) introduced the concept of effective stress for the particular case of saturated soil. He stated the principle of effective stress in the following terms:¹

“The stresses in any point of a section through a mass of soil can be computed from the total principal stresses σ_1 , σ_2 , σ_3 which act in this point. If the voids of the soil are filled with water under a stress u , the total principal stresses consist of two parts. One part, u , acts in the water and in the solid in every direction with equal intensity. It is called the neutral stress (or the porewater pressure). The balance $\sigma'_1 = \sigma_1 - u$, $\sigma'_2 = \sigma_2 - u$, $\sigma'_3 = \sigma_3 - u$ represents an excess over the neutral stress u and it has its seat exclusively in the solid phase of the soil. This fraction of the total principal stresses will be called effective principal stresses [...] A change in the neutral stress u produces practically no volume change and has practically no influence on the stress conditions

¹Using the nomenclature adopted by Skempton (1960)

for failure. [...] Porous materials (such as sand, clay and concrete) react to a change of u as if they were incompressible and as if their internal friction were equal to zero. All the measurable effects of a change of stress, such as compression, distortion and a change of shearing resistance are exclusively due to changes in the effective stresses $\sigma'_1, \sigma'_2, \sigma'_3$. Hence every investigation of the stability of a saturated body of soil requires the knowledge of both the total and the neutral stresses.”

The concept of effective stress forms the fundamental basis for studying saturated granular media mechanics and has been well accepted. Biot continued Terzaghi’s concept and proposed a general theory of consolidation for a fluid-saturated porous medium with occluded air bubbles, where the fluid/solid phases were treated as one body and the coupling terms were solved separately (Biot, 1941). Unsaturated porous media behavior is more complex. The state of stress in unsaturated materials is fundamentally different. The difficulties lies on how to consider the variable effects of water content and the role of contractile skin.

According to Terzaghi’s theory, the stress state variable for a saturated material can be expressed in the form of an equation:

$$\sigma'_{ij} = \sigma_{ij} - p^w \quad (2.2)$$

where σ'_{ij} is the effective stress, σ_{ij} is the total stress, and p^w is the pore water pressure. It is desirable to extend this concept to unsaturated materials. Numerous attempts have been made to develop a similar expression, in which all proposed equations have provided a single-valued effective stress or one stress state variable. This work was pioneered by Bishop (1960) and Bishop and Blight (1963). They proposed a tentative expression:

$$\sigma'_{ij} = (\sigma_{ij} - p^n) + \chi(p^n - p^w) \quad (2.3)$$

where p^n is pore air pressure and χ is a parameter related to the degree of saturation. The parameter χ is termed *the effective stress parameter*. The magnitude of the χ parameter is 1 for a fully saturated material and 0 for a dry material. Similar expressions have also been given by Aitchison and Donald (1956) and Jennings (1961). Such expressions indeed enable to describe a simple transition from fully saturated states, in which Terzaghi’s expression is covered, to partially saturated and completely dry states. Determination of χ and its dependency on the amount of water in the system is essential to evaluate the effective stress in unsaturated porous media. Bishop and Donald (1961) and Bishop and Blight (1963) performed experiments on cohesionless silt and compacted soils, respectively, to obtain the evidence for the validity of Eq.2.3 (see Fig.2.2).

The early experimental efforts were primarily concerned with determining the relationship between χ and the degree of saturation, s^w . Figure.2.2 shows a series of relationships between χ and s^w for a wide range of soil types (Bishop et al., 1960; Bishop and Donald, 1961; Jennings and Burland, 1962; Zerhouni, 1991). All curves evidence a seemingly trend for χ to follow the variations of s^w . However, no unique relationship can be found. Even though, some researchers started to propose the empirical expressions. Schrefler (1984) first raised the following simple expression:

$$\chi = s^w \quad (2.4)$$

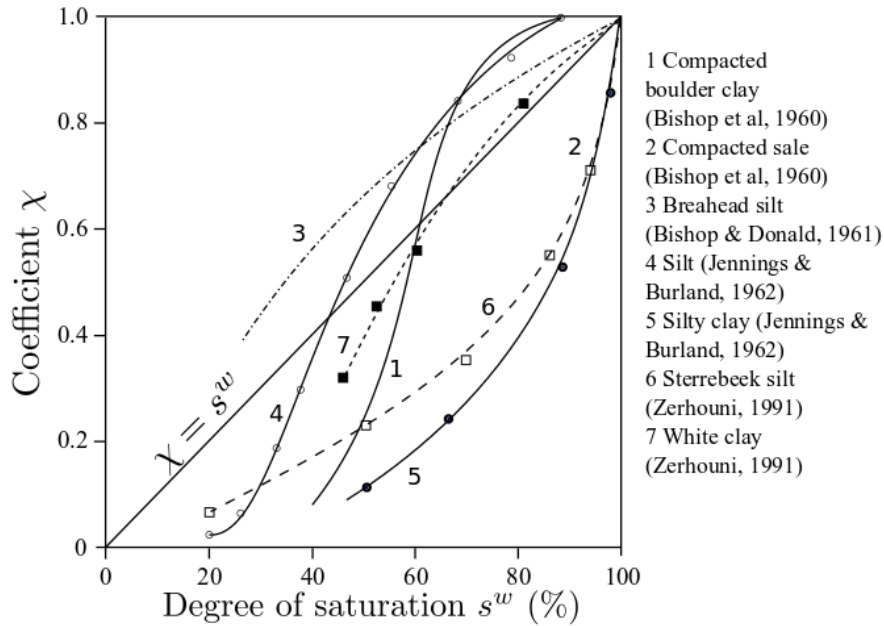


Figure 2.2: The relationship between effective stress parameter χ and the degree of saturation for a number of different soils in Zerhouni (1991) and review Nuth and Laloui (2008).

However, authors argued that such identity was not able to describe the ranges of saturation out of 20%-80%. Aitchison et al. (1985) proposed the following fitted expression,

$$\chi = \begin{cases} 1 & \text{if } s^w = 1 \\ (\alpha/s^w)s_e & \text{if } s^w < 1 \end{cases} \quad (2.5)$$

where s_e denotes the air entry suction and α denotes a coefficient varying from 0.3 to 0.35. More recently, Khalili et al. (2004) proposed that χ might be related to the current stress and stress history. He suggested to obtain the relationship by plotting χ against the ratio of matric suction over the air entry value. Khalili and Khabbaz (1998) wrote the following identity:

$$\chi = \begin{cases} (s^w/s_e)^{-0.55} & \text{if } s^w > s_e \\ 1 & \text{if } s^w \leq s_e \end{cases} \quad (2.6)$$

The definition of the effective stress has brought about some achievements in describing the shear strength of unsaturated materials, but it has not led to great success in modeling the general mechanical behavior. The limitations of the single effective stress were first reported by Jennings and Burland (1962). They argued that the “effective stress principle” failed to explain the collapse phenomenon upon wetting in unsaturated soils. A series of consolidation tests on several unsaturated soils were performed. The results showed that all samples collapsed upon flooding (*i.e.*, reducing suction), rather than expanding as is implied by the effective stress principle. Authors concluded that it is inappropriate to combine $(\sigma_{ij} - p^n)$ and $(p^n - p^w)$ into a single equation (Burland, 1965; Aitchison, 1965; Matyas and Radhakrishna, 1968; Brackley, 1971; Fredlund and Morgenstern, 1977).

Such early debates, prior to the 1990s, were mainly formulated within the context of a fully elastic (linear or not) theoretical framework. More recently, the authors argued that the plastic deformations such as collapse can be readily expressed within a single effective

stress framework by defining the yield surface as a function of suction (Kohgo et al., 1993; Modaressi and Abou-Bekr, 1994; Bolzon et al., 1996; Loret and Khalili, 2000; Khalili and Loret, 2001).

2.2.2 Independent stress variables

Besides the limitations described above, the essential question about the single-valued effective equation lies on the philosophical difficulty in justifying the use of soil properties in the description of the stress state. Morgenstern (1979) stated,

“The effective stress is a stress variable and hence related to equilibrium considerations alone. Bishop’s effective stress equation contains a parameter, χ , that bears on constitutive behavior. This parameter is found by assuming that the behavior of a soil can be expressed uniquely in terms of a single effective stress variable and by matching unsaturated behavior with saturated behavior in order to calculate χ . Normally, we link equilibrium considerations to deformations through constitutive behavior and do not introduce constitutive behavior directly into the stress variable.”

In 1960s and 1970s, many researchers realized that it is possible to use a multiple stress variable approach to model unsaturated materials behaviors rather than combining them into one single effective stress expression. This work was pioneered by Coleman (1962), who proposed the use of the net axial and radial stresses and the net pore water pressure to represent triaxial stress states. He suggested to express the volumetric strain as follows,

$$-\frac{dV}{V} = -C_{21}(dp^w - dp^n) + C_{22}(d(\frac{1}{3}(\sigma_1 + 2\sigma_3)) - dp^n) + C_{23}(d\sigma_1 - d\sigma_3) \quad (2.7)$$

where V is the overall volume, σ_1 is the axial total stress, σ_3 the lateral total stress, and C_{21} , C_{22} , C_{23} are independent parameters related to the material characteristics. Bishop and Blight (1963) plotted the volume changes under all-round pressure by using the independent stress variables (see Fig.2.3). Numerous researchers also implied the similar ways to describe the volumetric behavior (Matyas and Radhakrishna, 1968; Aitchison and Martin, 1973; Fredlund and Morgenstern, 1976).

Fredlund and Morgenstern (1977) then further examined the description of the stress state within the context of multiphase continuum mechanics. They postulated the unsaturated soil as a four-phase system, in which the air-water interface (i.e., “the contractile skin”) was considered as an independent phase. Their theoretical analysis concluded that “...any two of three possible normal stress variables can be used to define the stress state.” The possible combinations are: (1) $(\sigma_{ij} - p^w)$ and $(p^n - p^w)$; (2) $(\sigma_{ij} - p^n)$ and $(p^n - p^w)$; and (3) $(\sigma_{ij} - p^n)$ and $(\sigma_{ij} - p^w)$.

Such statement was also verified experimentally, in which a series of null test was performed. Through increasing each item of the combined stresses by the same amount, the experimental data indicated no overall volume change or water volume change. Among these three couples of variables, it was the combination (1) that proved to be the easiest to apply in engineering practice. From the physical point of view, the net stress $(\sigma_{ij} - p^n)$

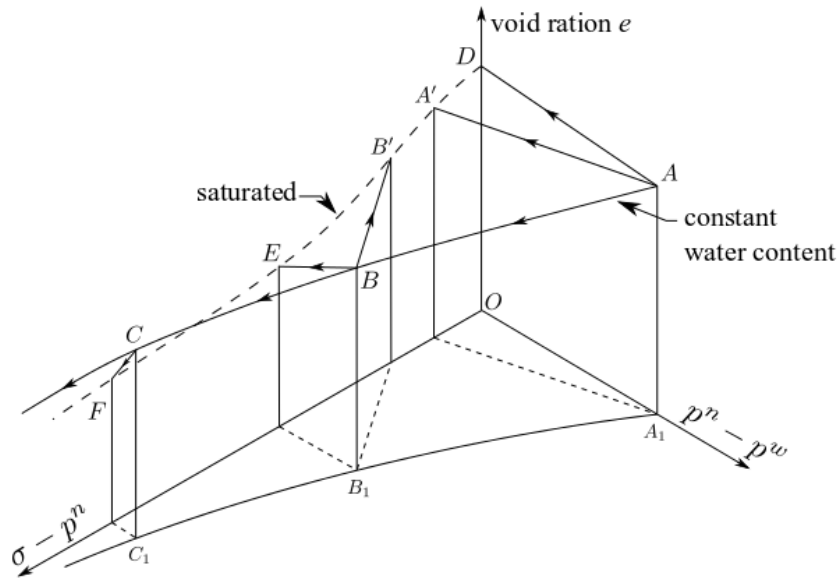


Figure 2.3: Volumetric characteristics expressed by independent stress variables in Bishop and Blight (1963)

accounts for the external loading, such as excavations or fills; the matric suction ($p^n - p^w$) can be considered as the consequence of climatic environment changing.

After the long-time debates on the stress framework for unsaturated soils, the independent stress variable approach has been proved to be an appropriate way for advanced constitutive modeling of unsaturated soils. (Although several forms of single effective stress framework are still possible.) It can produce a more meaningful description of unsaturated soil characteristics. The stress state variables can be used to formulate constitutive relations to describe the shear strength behavior and volumetric behavior.

2.3 Aspects of unsaturated granular materials behavior

Before we review the constitutive relationship of unsaturated porous media, it is necessary to summarize the basic features of the mechanical behaviors. In the field of unsaturated soil mechanics, the researchers mainly focus on three issues: (1) the volumetric behavior; (2) the strength behavior, and (3) the hydraulic behavior (Sheng et al., 2008).

2.3.1 Volumetric change

The volume changes of an unsaturated granular material can be caused either by the changes of external confining stress or by the changes of internal fluids potential (for instance, changing the matric suction). The volume changes of an unsaturated material can be expressed in terms of deformations or relative movement of the phases of the aggregate (i.e., the relative contents of fluid phases).

Loading/unloading at constant suction

The volume change characteristics induced by changes of confining stress have been extensively learned through different forms of loading conditions, such as isotropic, uniaxial, triaxial, oedometeric loading/unloading, etc (Biot, 1941; Coleman, 1962; Matyas and Radhakrishna, 1968; Barden, 1965; Maâtouk et al., 1995; Wheeler and Sivakumar, 1995). Generally, given a certain constant suction, sample shows gradual decrease in its volume when loaded; the sample swells when it is unloaded. During loading, the volume change is irreversible (i.e., plastic) if the sample is passing a yield stress. That is nothing special for the materials. For an identical sample loaded at different suction levels, the yield stress increases with increasing suction. Quantitatively, the volume changes behavior of unsaturated materials is usually described as a function of net stress and suction (including the wetting/drying cases of the next section). A series of expressions for formulating the stress-deformation relations under different loading/unloading conditions have been established using mathematical or semiempirical approaches (Fredlund et al., 2012; Chou and Pagano, 1967; Fung, 1965; Fredlund and Morgenstern, 1976; Alonso, 1993; Pham, 2005). Such relations can be used to predict the volume changes (including overall volume change and phase volume changes) that caused by the changes of stress state variables.

Drying/wetting at constant net stress

During drying (increasing suction), the volume of sample usually first decreases. For the materials with low plasticity, it is generally accepted that the volume change is small and reversible (i.e., the sample first shrinks then swells). At high level of suction, the plastic deformation may happen (i.e., the sample shrinks only).

The wetting cases are more complex. If it is performed (by decreasing suction) at low level of net stress, the sample swells. However, if the net stress is in high value, the volume shows a reduction, which is commonly termed as “collapse” (compression). Alonso et al. (1987) proposed the Loading-Collapse (LC) yield curve to reproduce such phenomenon, in which the deformation was treated as plastic behavior when the stress state reached the LC curve. This proposal was later employed in developing of the Barcelona Basic Model (BBM) (Alonso et al., 1990).

2.3.2 Strength behavior

Although the debates on universal stress framework were still lasting, the researchers have already started to formulate the shear strength of unsaturated granular materials using different stress variables.

Based on the single effective stress approach proposed by Bishop (1960), Bishop et al. (1960) extended the Mohr-Coulomb failure criterion to get the following equation for shear strength of an unsaturated material:

$$\tau = c' + (\sigma - p^n) \tan \phi' + \chi(p^n - p^w) \tan \phi' \quad (2.8)$$

where τ is the shear strength of the material, c' is the effective cohesion, ϕ' is the angle of shearing resistance and χ is Bishop's effective stress parameter.

Based on the independent stress variables framework, Fredlund et al. (1978) used net stress and matric suction to formulate the shear strength. They suggested the following expression:

$$\tau = c' + (\sigma - p^n) \tan \phi' + (p^n - p^w) \tan \phi^b \quad (2.9)$$

where $(\sigma - p^n)$ is the normal net stress on the failure plane, c' and ϕ' are the cohesion intercept and friction angle respectively for saturated conditions and ϕ^b is the friction angle with respect to suction. It was assumed that both ϕ' and ϕ^b are independent variables. If ϕ^b is a constant, the above expression predicts a linear increase of shear strength with suction. However, the subsequent experimental research showed that such relationship is nonlinear (Escario and Saez, 1986; Gan et al., 1988). Fredlund et al. (1987) suggested that ϕ^b is equal to ϕ' at low level of suction (the material remains saturated) and ϕ^b decreases with increasing suction as the material becomes unsaturated.

Khalili and Khabbaz (1998) employed a two stress state variables approach for the prediction of the shear strength with the form of Eq.2.8, in which the effective stress parameter was expressed by Eq.2.6. Alonso et al. (2010) used the information of the water retention curves of different soils to predict the shear strength by the following expression,

$$\tau = c' + [(\sigma - p^n) + S_r^e(p^n - p^w)] \tan \phi' \quad (2.10)$$

where S_r^e is termed the effective degree of saturation.

2.3.3 Water retention curve

The relationship between the suction (matric or total suction) and the water content (volumetric or gravimetric) is termed as a “water retention curve” (WRC) or “soil water characteristics curve” (SWCC) (or “capillary pressure-saturation ($p^c - s^w$) curve” in two-phase flow)². The main purposes of WRC are to predict the soil water storage, water supply to the plants and soil aggregate stability. Considerable work has been done on various aspects of WRC in soil science (Mualem, 1974; Fredlund et al., 1994; Croney, 1952; Leong and Rahardjo, 1997; Hassanizadeh et al., 2002). Fig.2.4 shows the typical WRCs expressed in terms of degree of saturation s^w and suction p^c , in which the $s^w - p^c$ curves during the wetting and drying process are following different paths. Such phenomenon is termed “hydraulic hysteresis”.

Although no unique relationship between suction and water content can be established, numerous constitutive expressions have been proposed to characterize the water retention response based on the experimental measurements, specifically formulating the main drying curve or the main wetting curve (Gardner, 1958; Brooks and Corey, 1964; Brutsaert, 1967; Campbell, 1974; Van Genuchten, 1980; Fredlund and Xing, 1994; Pham et al., 2005). In most of these expressions, one parameter bears a relationship to the air-entry value and a second parameter is related to the rate of soil desaturating. A third parameter may be introduced in some expressions to allow the curves to follow a different slope at low level of suction. For instance, Van Genuchten (1980) proposed the following

²Technically, WRC should be classified as the hydraulic content of the previous chapter, however, it is highly related to the mechanical behavior and the empirical constitutive relations of unsaturated soil in soil mechanics. Thus, we put the reviews in this section.

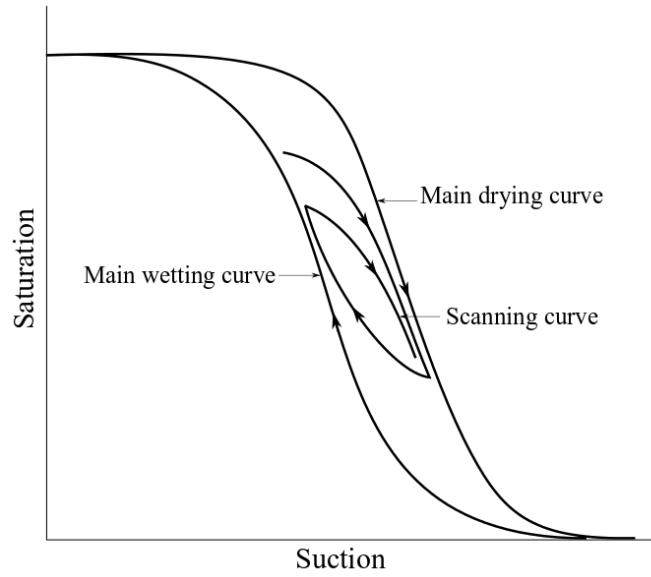


Figure 2.4: Typical water retention curve for a granular material, after Al-Sharrad (2013).

expression,

$$\theta(\psi) = \theta_r + \frac{\theta_s - \theta_r}{[1 + (\alpha|\psi|)^n]^{1-1/n}} \quad (2.11)$$

where, $\theta(\psi)$ is the water retention curve [L^3L^{-3}]; $|\psi|$ is suction pressure ($[L]$ or cm of water); θ_s is saturated water content [L^3L^{-3}]; θ_r is residual water content [L^3L^{-3}]; α is related to the inverse of the air entry suction, $\alpha > 0$ ($[L^{-1}]$, or cm^{-1}); n is a measure of the pore-size distribution, $n > 1$ (dimensionless).

2.4 Constitutive modeling of unsaturated soils

The mechanical constitutive law describes the strain and stress behaviors of the material and plays an essential role for the numerical implementation. In general, constitutive laws for unsaturated soils can be divided into two categories: elastic and elastoplastic models. Fig.2.5 shows an overview of some common types of constitutive models, which are summarized by Fredlund et al. (2012). Elastic models for unsaturated soils are usually based on the extensions of Hooke's law (Fredlund and Morgenstern, 1976). They are easy to implement within numerical analysis, however, they can not describe the irrecoverable strains. Thus, the elastoplastic models emerged.

In the context of continuum mechanics, the first complete elastoplastic model for unsaturated soils is the Barcelona Basic Model (BBM) (Alonso et al., 1990), which is based on the theoretical framework proposed by Alonso et al. (1987). A more summary form can also be found in Gens et al. (1989). BBM is intended for unsaturated soils which are slightly or moderately expansive, such as unsaturated sands, silts, clayey sands, and clays of low plasticity. The motivation of the development of BBM was to implement the mechanics and characteristics of unsaturated soils into the mature modeling of saturated soils. It is assumed that the net stress and suction are the fundamental variables.

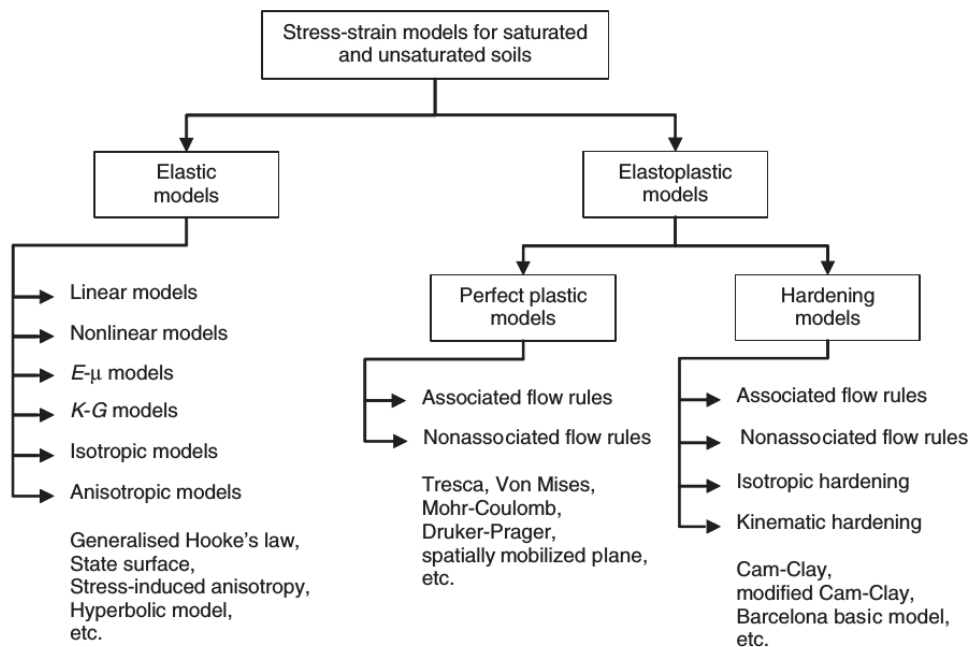


Figure 2.5: Stress-strain constitutive models for unsaturated soils, summarized by Fredlund et al. (2012).

Fig.2.6 illustrates the essential idea. It depicts a three dimensional yield surface in $p - q - p^c$ space, where p is the mean net stress, q is $(\sigma_1 - \sigma_3)$ and p^c is suction (see Fig.2.6). Under saturated conditions (i.e., $p^c = 0$), the yield surface corresponds to the Modified Cam-Clay (MCC) ellipse. With the increasing of suction, (i.e., unsaturated regimes are obtained,) the size of the elastic domain increases. The link between saturated and unsaturated regimes is the rate of increase, which is represented by the loading-collapse (LC) curves. The elastic domain is limited by yield limit related to suction increase (SI). This limit is determined by the maximum previously experienced suction.

The BBM accounts for the stiffness changes of the soil induced by suction changes and is able to reproduce many mechanical features of unsaturated soils, such as wetting-induced swelling or collapse. After that, a large number of other elastic-plastic models followed (e.g., Josa et al. (1992); Wheeler and Sivakumar (1995); Cui and Delage (1996) among many others). Most of them are based on the same fundamental principles, sought to improve some shortcomings of BBM.

A common feature of these models is that they employed the net stress as the stress variable for establishing the constitutive laws. As summarized by Gens et al. (2006), in general, three categories of models could be identified depending on the choice of stress variables for formulating the constitutive relationships: (1) net stress (the above models); (2) net stress plus a function of suction but not of degree of saturation (Kohgo et al., 1993; Modaressi and Abou-Bekr, 1994; Lorent and Khalili, 2002; Russell and Khalili, 2006) and (3) net stress plus a combined function of suction and degree of saturation (Bolzon et al., 1996; Jommi, 2000; Sheng et al., 2004; Tamagnini, 2004; Wheeler et al., 2003).

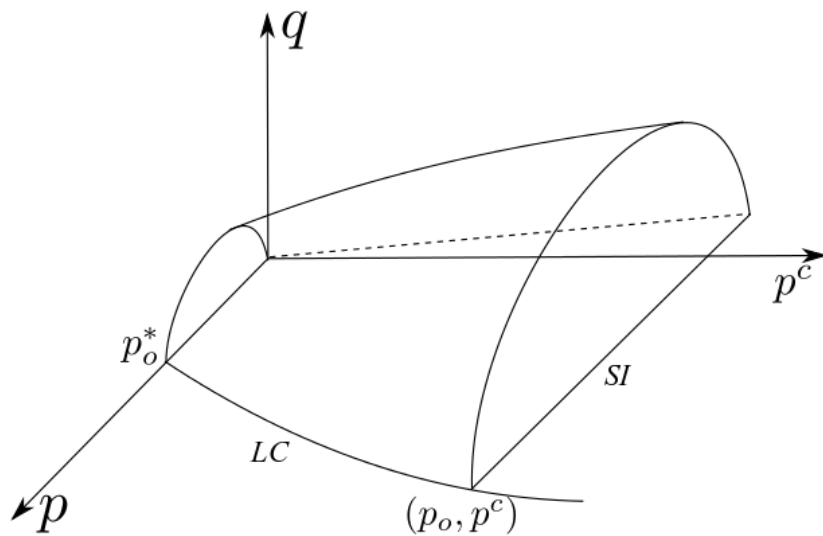


Figure 2.6: Three-dimensional representation of the yield surface in the BBM, after Alonso et al. (1990).

Conclusions

The phenomenon of two immiscible fluids through a deformable granular material is widely encountered in nature and in many areas of engineering and science. To understand the physics, i.e., the interactions between fluid, fluid and solid phases, is of importance for its applications. To reproduce the hydromechanical couplings of the complex system requires the knowledge of each component phase. Thus in this part, the literature reviews have been presented from two aspects.

The knowledge of the components of fluid phases has been reviewed in the context of two-phase flow of hydromechanics. The physical properties of two-phase flow, such as the dynamic characteristics and the states of the fluid, have been recalled. For the numerical aspect, three major categories of methods have been introduced based on the different scale references. The family of pore scale methods have been discussed in detail, where we focused on the pore-network modeling. The governing equations for the motion of the fluid phases have been reviewed on basis of conservation theory. In addition, we have introduced several other pore scale approaches for the hydromechanical couplings. Their limitations have been recalled.

The physics and mechanical properties of solid phase have been introduced on basis of the knowledge from soil science, where the system is termed as unsaturated soil. The basic features of the mechanical behaviors of unsaturated soil have been reviewed from three aspects. Such behaviors will be reproduced later with our model in the thesis. Two main issues which are related to the numerical modeling have been recalled.

- **Stress framework** The single effective stress framework is on basis of Bishop's expression, where the effective stress parameter has been formulated by many researchers. In chapter 6 and 7, we will recall this term and investigate its relationship with the saturation. The independent stress variables framework has proven effective in establishing advanced constitutive relationship for unsaturated soil.
- **Constitutive modeling** The elastoplastic constitutive modeling is the mainstream. In continuum-based background, the Barcelona Basic Model (BBM) has been considered as an appropriate framework for modeling the elastoplastic behaviors. Many constitutive models have been developed based on BBM. Depending on the implementation of different stress variables in the models, three categories elastoplastic constitutive laws have been distinguished.

Solving the hydromechanical couplings, a direct link between the hydraulic and mechanical responses is also required. The macro-scale continuum based models usually employ empirical relationships. The current micro-scale and pore-scale methods usually only focus on the motion of the fluid phases, considering the solid structure motionless. In the next part, we will present a new hydromechanical couplings scheme at the pore-scale, where the solid phase is deformable and an explicit link between the fluids and the solid structure can be found.

Part II

The 2PFV-DEM model

Chapter 3

The two-phase pore-scale finite volume modeling

In this chapter, we will propose a pore-scale model aiming to simulate the hydraulic and mechanical behaviors of unsaturated deformable granular materials. Specially, the model is designed for the quasi-static two-phase flow of drainage. We term this approach as “two phase pore-scale finite volume - discrete element method” coupling scheme, or “2PFV-DEM” model.

In the model, the unsaturated granular material is idealized to be a system composed by the spherical particles and two immiscible fluids, or termed the wetting/non-wetting/solid (W-NW-S) phases system. The underlying idea of 2PFV-DEM model is to combine a pore-scale network and the DEM for the fluid phases and the solid phase, respectively. The 2PFV component of the model follows a partitioned approach and is intended to provide a tool for the analysis of the behavior of two-phase flow of drainage. The DEM framework offers the possibility of modeling micro-mechanical behaviors by defining the mechanical properties of the individual interactions between particles. The hydro-mechanical coupling is ensured by an explicit topology of pore-scale network.

This first chapter will be devoted to the description of the model, in which the coupling strategy and the resolution of each component will be elaborated. The next chapter will present the implementation of the model. Some primary results will also be shown.

3.1 Pore-scale network

As mentioned in the general introduction, solving coupled flow-deformation problems need to map a network on a given set of solid grains. The mechanical coupling requires a direct and explicit link between the network geometry and the positions of the solid grains, and the computational cost of updating the network should be kept as small as possible. It makes the Delaunay/Voronoi methods best candidates since they introduce a simple duality between the solid objects and the void space.

Delaunay triangulations and their dual Voronoi diagram are widely used in computer science and many other areas related to computational geometry (Aurenhammer, 1991). In the area of granular materials, Delaunay triangulation has been applied for domain decompositions of sphere packings in order to define the micro-scale mechanical properties, such as strain and stress (Calvetti et al., 1997; Bagi, 2006; Jerier et al., 2010). For mono-

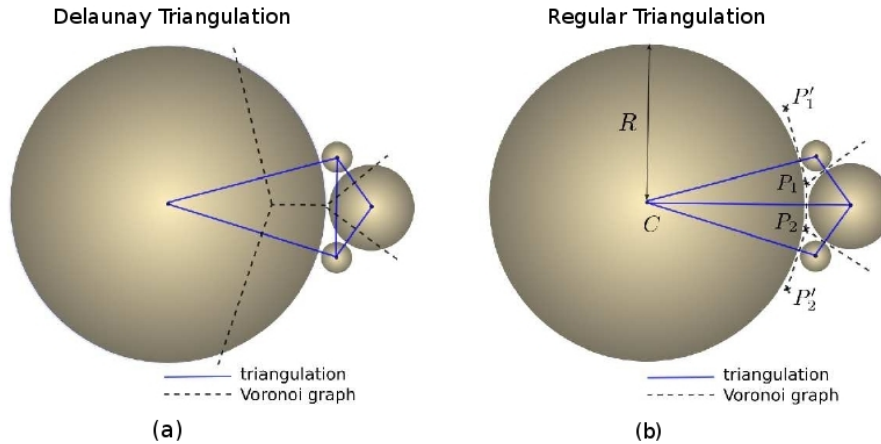


Figure 3.1: Comparison of triangulations and their dual Voronoi graph in two dimensions. (a) the dual graph of Delaunay triangulation has branches inside discs; (b) the dual of the Regular Triangulation has all branches in the pore space.

sized sphere packings, the Voronoi diagram is able to decompose the void space properly. However, for poly-disperse sized packing, this approach presents some shortcomings. Notably, the branches (in 2D) or facets (in 3D) of Voronoi cell may cross non-void regions, as illustrated in Fig.3.1a. In order to overcome such limitation, “Regular triangulation” method was proposed for the decomposition of the spheres of different sizes.

Regular Triangulation, also known as weighted Delaunay triangulation or power diagram, generalises the classical Delaunay triangulation to weighted points, where the weight accounts for the size of each sphere (Edelsbrunner and Shah, 1996). Typical examples are shown in Fig.3.2, where the tetrahedra define pore bodies and the facets correspond to the pore throats. The dual Voronoi graph of regular triangulation (also known as Laguerre graph or radical Voronoi graph) is based on radical planes and it is entirely contained in the void space. This is an appropriate feature to describe the flow path within the pore space, as opposed to the classical Delaunay/Voronoi graphs (see Fig.3.1b).

Based on the decomposition of Regular Triangulation, a pore is defined as the pore space surrounded by four solid spheres whose centres are the vertices of the corresponding tetrahedron. The volume of the pore body corresponds to the irregular cavity within the tetrahedron (see Fig.3.3(a)). The shape of a pore throat is defined by the cross sectional area extending within a tetrahedral facet (Fig.3.3(b)). The throat does not enclose any volume, but it will play a key role when defining the entry capillary pressure of an invading non-wetting phase (NW-phase).

Since each pore corresponds to a tetrahedron, it has four neighbours, resulting in a lattice of connectivity equal to four. Relatively similar networks can be found in other models (Mason, 1971; Mason and Mellor, 1995; Bryant et al., 1993a; Gladkikh and Bryant, 2003), yet the decomposition techniques therein are restricted to uniform particle sizes by the choice of Delaunay triangulation. Regular triangulation extends the approach to poly-disperse spheres. Its mathematical definition is limited to geometrical arrangements of non-overlapping or moderately overlapping spheres. More precisely the maximum overlap is when the centre of one sphere enters another sphere, in this occurrence the regular triangulation would be undefined. Since repulsive forces at contacts prevent such overlaps when the assembled spheres represent solid grains, the regular triangulation that is

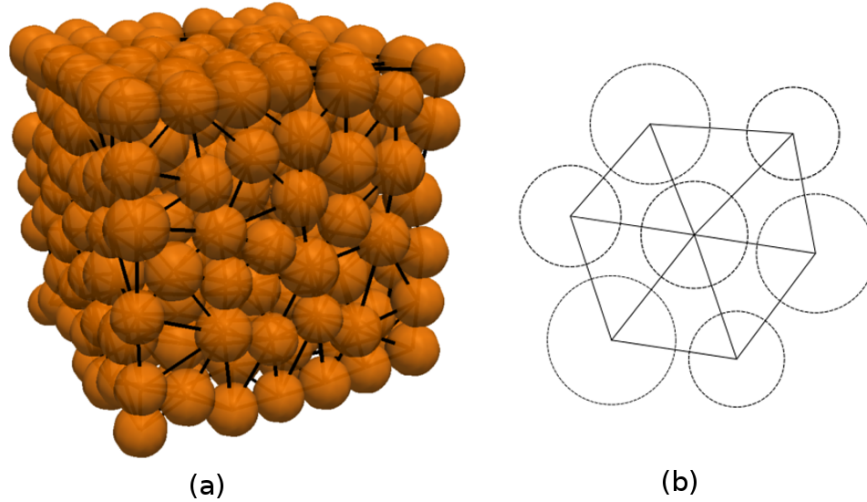


Figure 3.2: Regular triangulation in three dimensions (a) and two dimensions (b).

adopted is always defined.

In order to explain the governing equations of the couplings, hereafter we introduce the symbolic representation of pore geometry. Ω denotes a full domain occupied by a porous material, in which Γ , Φ and Θ are the domains occupied respectively by the S, NW and W phases: $\Omega = \Gamma \cup \Phi \cup \Theta$, $\Gamma \cap \Phi = \emptyset$, $\Gamma \cap \Theta = \emptyset$ and $\Phi \cap \Theta = \emptyset$ (Φ and Θ are also called “NW pores” and “W pores”). The NW-W interface of the two-phase problem in full domain can be expressed by $\Phi \cap \Theta$, and the NW-W-S phase interfacial contact lines can be written by $\Phi \cap \Theta \cap \Gamma$.

We denote by N_c the number of tetrahedral cells in the regular triangulation of the sphere packing, and by Ω_i the domain defined by tetrahedron i : $\Omega = \cup_{i=1}^{N_c} \Omega_i$. Similarly, N_s is the number of spheres, and Γ_k the domain occupied by sphere k , so that $\Gamma = \cup_{k=1}^{N_s} \Gamma_k$.

3.2 Fluid phases

3.2.1 Local rules

In the absence of gravity the movement of immiscible phases occurs in different regimes distinguished by the relative contribution of viscous stresses and surface tension. As introduced in section.1.1.2, the balance between the two depends on two dimensionless numbers, the viscosity ratio M and the capillary number C_a (Lenormand et al., 1988; Lenormand, 1990). The limit of “quasi-static” flow corresponds to $C_a = 0$, a situation in which the viscous effects can be neglected.

The model we propose aims at simulating the slow primary drainage of air-water systems, or more generally non-wetting/wetting (NW-W) systems. We assume a quasi-static regime and a perfect wetting of the solid (S-phase) by the wetting phase (W-phase). Consistently, the fluid pressure is piecewise uniform in every set of pores occupied by a certain phase and connected through this particular phase, i.e. one fluid cluster has only one fluid pressure (it applies for both the W and the NW phases). For drainage, the invade NW-phase is a single cluster of fluid, however, the receding W-phase can be separated into

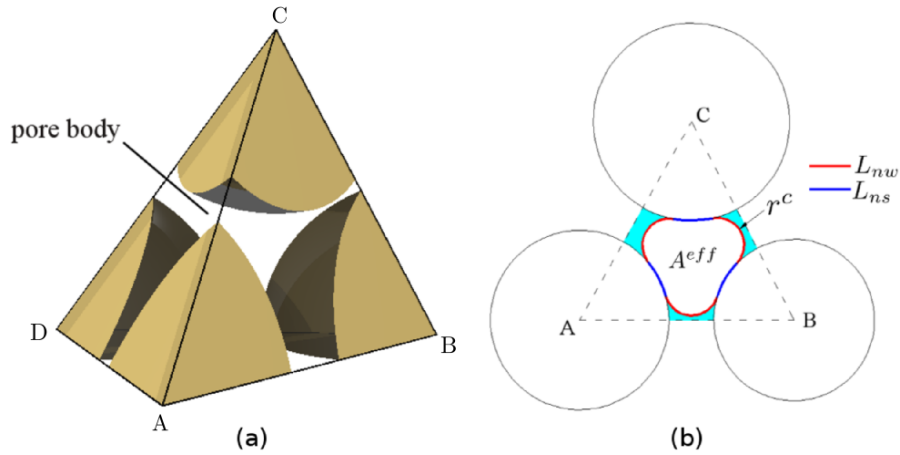


Figure 3.3: Pore geometry. (a) A pore defined by tetrahedral element of the finite volume decomposition. (b) Definition of a pore throat geometry. r^c is the curvature of meniscus; L_{nw} is the length of contact line between NW and W phases; L_{ns} is the length of contact line between NW and S phases. $L^{eff} = \sum(L_{nw} + L_{ns})$, in which L^{eff} is termed effective entry pore throat perimeter. A^{eff} is the planar project area of NW-W interface, and is termed effective entry pore throat area.

many clusters. We can assume such wetting clusters are all connected by the wetting phase film, then consequently all wetting clusters have the same value of pressure. Either we can assume the wetting clusters are independent and physically isolated by the NW-phase. The local W-phase pressure can differ from the reservoir pressure. Such two different assumptions will lead to two different hydraulic response. We will further explain and define them in next section.

The drainage process is controlled by the capillary pressure p^c , i.e., the pressure difference between the NW-phase and W-phase: $p^c = p^n - p^w$. In quasi-static flow, the invasion of a pore body can be seen as an instantaneous event in which the interface moves from one throat to the next ones by a so-called *Haines jump* (see Fig.3.4). Thus the interfaces are always located near the throats in the simulation, practically. When a pore saturated by the W-phase is adjacent to another pore already invaded by the NW-phase, the stability of the W-NW interface at the corresponding throat depends on the entry capillary pressure p_e^c associated to the throat (see next section). Because the entry capillary pressure of the pore body is smaller than that of the pore throat, the body is filled by the NW-phase spontaneously as soon as $p^c > p_e^c$.

If $p^c > p_e^c$, the pore is drained. In principle, a certain amount of the receding W-phase can be left behind in the invaded domain in the form of disconnected pendular rings (Scholtès et al., 2009; Scholtès et al., 2009a). At this stage we neglect the volume of such rings when determining the total volume of each phase. Neither do we consider the presence of W-phase in the corners of the throats (a situation sometimes considered for prismatic pore throats) as it would make little sense in sphere packings. To sum up, the pore space is entirely contained in the pore bodies and the saturation of one pore is simply binary, i.e., it equals 0 or 1 depending on which phase is present. Obviously, some real situations may differ significantly from such idealization. The residual saturation in particular may be modified by imperfect wettability, leaving some pores only partially drained, or by viscous effects - especially for high viscosity fluids such as oils.

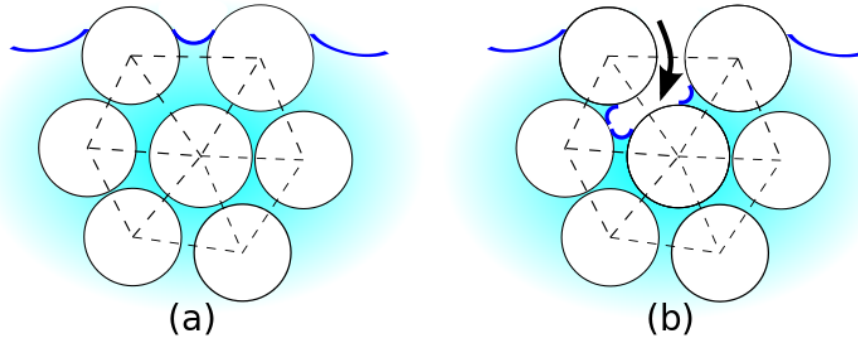


Figure 3.4: The displacement of NW-W interface between two equilibrium states, from (a) $p^c < p_e^c$ to (b) $p^c > p_e^c$ (in 2D for clarity).

The comparison with experiment in section 4.2.3 suggests that the simplifications may be acceptable for a first approach of some air-water systems. Further model refinement will be necessary for simulating more general conditions.

3.2.2 Pore invasion model

Numerically, we consider the solid phase of the unsaturated granular material as a random dense packing of poly-disperse spheres. Such packing will be generated with the DEM method (Šmilauer et al., 2015). The network representation of pore space can be obtained by using the Regular Triangulation as mentioned in previous section. The main numerical work for defining the 2PFV component is twofold. (1) Locally, define the algorithm for drainage of a single pore (i.e., determine p_e^c). (2) Globally, define the logic of drainage sequences of all pores.

Determination of entry capillary pressure

The drainage process is assumed in quasi-static regime, so p^c is applied into porous media to result from one equilibrium state to another. In fluid statics, a relationship between capillary pressure, p^c , interfacial tension, γ^{nw} , and mean curvature of the NW-W interface, C , is given by the Young-Laplace equation

$$p^c = 2C\gamma^{nw}. \quad (3.1)$$

C can be expressed in terms of the principal radii of curvature of the meniscus (r_1 and r_2) by

$$2C = \left(\frac{1}{r_1} + \frac{1}{r_2}\right) \quad (3.2)$$

This is a starting point for defining p_e^c , yet r_1 and r_2 are difficult to define precisely for an interface near a pore throat of complex geometry. Approximations are necessary.

We propose to determine p_e^c based on MS-P (Mayer-Stowe-Princen) method, which employs the balance of forces on the NW-W interface (Mayer and Stowe, 1965; Princen, 1969). The balance reads

$$\sum \mathbf{F}(p^c) = \mathbf{F}^c(p^c) + \mathbf{F}^t(p^c) = 0 \quad (3.3)$$

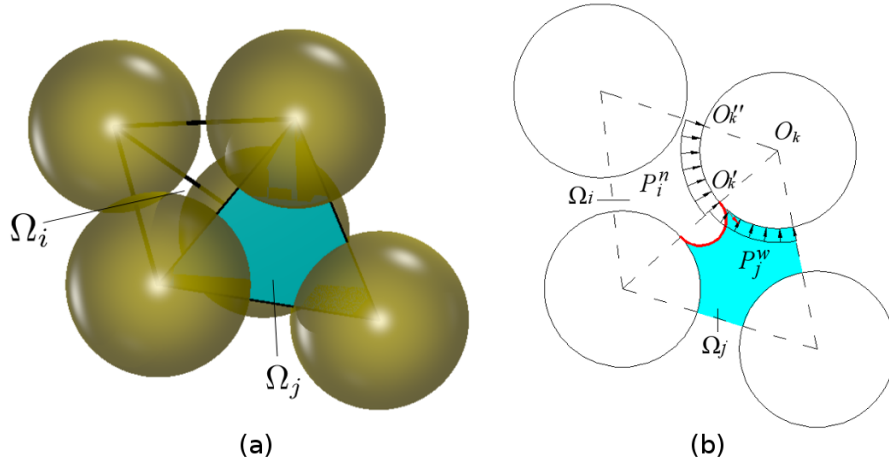


Figure 3.5: (a) Construction of subdomain Ω_{ij} , the pore of Ω_i is occupied by NW-phase (Φ_i), the pore of Ω_j is occupied by W-phase (Θ_j); (b) Two-phase fluid pressure and interfacial tension on S-phase. (in 2D for clarity).

where \mathbf{F}^c is the capillary pressure acting on the interface and \mathbf{F}^t is the total tension force on multi-phase lines. p_e^c is the value of p^c such that $\sum \mathbf{F}(p^c) = 0$. This method for determining p_e^c follows Ma et al. (1996); Prodanović and Bryant (2006) and Joekar-Niasar et al. (2010b). Therein, the MS-P method is applied to cylindrical throats. Our situation is more complex since the cross sectional shape is changing along the flow path. By employing the MS-P method we *de facto* assume that p_e^c is the same as in a cylindrical throat tangent to the solid phase at the narrowest cross section, an assumption which will be evaluated in section 4.2.3. For completeness, we recall the generic aspect of the MS-P method hereafter.

Figure 3.3(b) shows the typical geometry of a pore throat and the parts occupied by the different phases and interfaces. If p^c increases the region occupied by the NW-phase grows, pushing the W-phase further toward the corners of the throat. The longitudinal curvature of the W-NW interfaces is supposed to approach zero as p^c approaches p_e^c (Joekar-Niasar et al., 2010b), i.e., $r_1 \rightarrow +\infty$ in Eq. 3.2. Assuming that both phases pressure are uniform around the throat, the remaining cross-sectional curvature r_2 must take the same value for all three W-NW interfaces (based on Eqs. 3.1-3.2). This value is denoted by r^c and it is related to the entry capillary pressure

$$p_e^c = \frac{\gamma^{nw}}{r^c} \quad (3.4)$$

Let us start from the simple case and assume domain Ω_{ij} is involving a local drainage event, in which the void space in tetrahedron Ω_i is occupied by NW-phase Φ_i (i.e., Φ_i is a non-wetting pore), the void space in tetrahedron Ω_j is occupied by W-phase Θ_j (i.e., Θ_j is a wetting pore) and S_{ij} is the common facet of Ω_i and Ω_j , as shown in Fig. 3.5a. The pressure face NW-W interface domain $\Phi_i \cap \Theta_j$ can be written:

$$\mathbf{F}_{ij}^c = \int_{\partial\Phi_i \cap \Theta_j} (p_i^n - p_j^w) \mathbf{n} ds \quad (3.5)$$

Since the integral on the irregular NW-W interface could be computationally expensive, it can be solved by projecting the phases pressures on the conjugate planar part (i.e., the

pore throat section),

$$\mathbf{F}_{ij}^c = A_{ij}^{eff} (p_i^n - p_j^w) \mathbf{n} \quad (3.6)$$

where A_{ij}^{eff} is the projected area of NW-W interface on common facets of Ω_i and Ω_j , i.e., the projected area of $\partial\Phi_i \cap \Theta_j$ on S_{ij} (see Fig.3.3b).

The interfacial tension force on NW-W-S contact lines \mathbf{F}_{ij}^t can be written,

$$\mathbf{F}_{ij}^t = \int_{\partial^w\Phi_i \cap \Theta_j \cap S_{ij}} \gamma^{nw} \mathbf{n} dl + \int_{\partial^s\Phi_i \cap \Theta_j \cap S_{ij}} \gamma^{ns} \mathbf{n} dl - \int_{\partial^s\Phi_i \cap \Theta_j \cap S_{ij}} \gamma^{ws} \mathbf{n} dl \quad (3.7)$$

The multiphase interfacial tensions, γ^{ns} , γ^{ws} and γ^{nw} have a relationship with contact angle θ , defined by Young's equation,

$$\gamma^{ns} = \gamma^{nw} \cos \theta + \gamma^{ws} \quad (3.8)$$

Under a perfectly wetting assumption, i.e., $\theta = 0$, then Eq.3.7 can be written,

$$\mathbf{F}_{ij}^t = \int_{\partial^w\Phi_i \cap \Theta_j \cap S_{ij}} \gamma^{nw} \mathbf{n} dl + \int_{\partial^s\Phi_i \cap \Theta_j \cap S_{ij}} \gamma^{nw} \mathbf{n} dl = L_{ij}^{eff} \gamma^{nw} \mathbf{n} \quad (3.9)$$

in which, L_{ij}^{eff} is total length of contact lines (also is the perimeter of entry pore throat section).

All terms of Eq.3.6 and Eq.3.9 can be expressed as functions of r^c (see Appendix), so that the equilibrium equation Eq.3.3 is an implicit definition of r_e^c , the value of r^c for which the equation is satisfied (noting that $\sum F$ is a monotonic function of r^c):

$$\sum \mathbf{F}(r^c) = \mathbf{F}^c(r^c) + \mathbf{F}^t(r^c) = 0 \quad (3.10)$$

Solving the equation numerically gives r_e^c . In turn p_e^c can be determined using Eq.3.4.

Drainage and entrapment of W-phase

Globally, the drainage sequence of all pores is determined by their connectivity, i.e., the topological network. In order to explain the invasion logic of 2PFV model, we represent the 3-D network by using a 2-D lattice mapping (see Fig.3.6). The pore bodies and the throats are represented by squares and linear connections respectively. (The solid phase is not shown in the figure, for clarity.) Different flags are assigned to the pores to reflect the individual state of saturation (0 or 1) and whether a particular pore or a group of pores is directly connected to one of the main reservoirs. A search algorithm is employed for updating those states during invasion.

Initially, the sample is fully saturated. We assume the top and bottom boundaries are connected to NW and W reservoirs, respectively. The effect of gravity is ignored. Drainage starts by decreasing the W-phase pressure p^w of the W reservoir while the NW-phase pressure p^n in the NW reservoir is kept constant (thus increasing p^c). A search is executed on the pore throats which separate the phases. The throat with lowest p_e^c is where the first displacement of the interface will occur (Haines jump), leading to the invasion of a first pore by the NW phase. As soon as this pore is invaded the NW phase reaches new

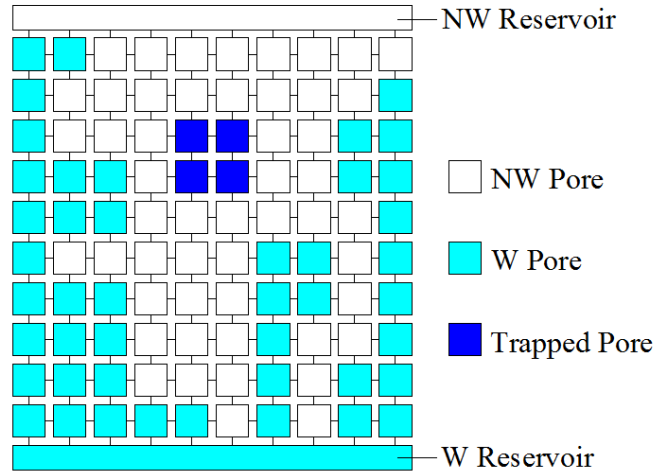


Figure 3.6: Illustration of boundary conditions, NW-phase invasion and W-phase trapping in the network (in 2D mapping for clarity).

throats, possibly triggering a recursive cascade of Haines jumps and invading more than one pore for one single value of applied p^w , until no more throats satisfy $p_e^c < p^c$. It leads to discontinuous changes of the W-phase content which have been also observed in experiments (Culligan et al., 2004). When the simulation reaches the new stable configuration for a certain applied p^c , the state flags are updated for the next step of drainage.

As the NW-phase is invading, the W-phase may form clusters of pores which are disconnected from the W reservoir (such W-phase clusters are also disconnected with each other). In order to identify these entrapment events, a dynamic search algorithm is employed after each drainage event. Geometrically, each individual W-phase cluster is indeed isolated by the NW-phase; physically, their connectivity may need further assumptions and discussions.

In short periods of time, we assume that there is no film flow or evaporation in the model, thus the disconnected regions remain saturated by a fixed amount of the W-phase throughout subsequent increases of p^c . In 2PFV model, we label this drainage mode as “with-trap” drainage. Such assumption is acceptable for sufficiently fast drainage. It is worth noting that the W-phase is assumed to be incompressible, thus the geometry of the W-phase and NW-W interfaces for disconnected regions remains unchanged throughout the next steps of drainage. According to Eq.3.1, p^c will also remain the same because of unchanged NW-W interfacial curvature. Since the disconnections of different regions may happen at different times of the drainage, every disconnected region has its own local value of p^w ultimately, i.e., the localization of p^c (consistently with Harris and Morrow (1964) for instance). To sum up, in “with-trap” drainage, we assume:

1. Physical disconnection between individual W-phase clusters is possible. The flux exchange between disconnected clusters is not allowed. It may lead to a non-zero residual saturation and to different pressure in different disconnected regions.
2. The local capillary pressure is subjected to the invasion sequence, which is essentially determined by the geometry of the pores. Pressure is not exchanged between disconnected clusters.

In long terms, this simplification may lead to slightly overestimate the W-phase content of samples subjected to p^c . Since under dry conditions, the mobilization of the trapped cluster can still be observed even if it has been disconnected from its reservoir. The possible cause of this transport would relay on surface potential and thermodynamic potential (Aslyng, 1963; Nitao and Bear, 1996; Tuller et al., 1999; Likos and Jaafar, 2013). Thus, we also develop another drainage model, termed “*without-trap*” drainage. In this case, we assume all isolated W-phase clusters are connected to the W-phase reservoir by the films and provide that mass transfer to or from the pendular rings is possible. Consequently, the diversity of inner pressure of different disconnected clusters will become inconspicuous because of the film transport. We assume that the pressure of each isolated domain is equal to the pressure of W-phase reservoir, for simplicity. To summarize, in “*without-trap*” drainage:

1. Mass can be exchanged between individual W-phase clusters. The disconnected W-phase can be drained eventually. Consequently, the residual saturation is 0.
2. The distribution of capillary pressure is uniform, which is equal to the pressure difference of reservoirs.

Although we artificially classify the connectivity of individual W-phase clusters/reservoir into two cases, the purposes can be seen from the physical point of view. The “*with-trap*”/“*without-trap*” drainages can be considered as the undrained/drained test conditions of soil mechanics, separately.

Boundary conditions

The boundary conditions are defined from two different aspects: the geometrical consideration of the network and the realistic requirements. In DEM simulation, the rigid walls are usually introduced to represent the boundaries in order to easily assign the boundary loading/unloading conditions. However, such definition will increase the complexity of the regular triangulation generation. To solve this limitation, we follow the strategy of Chareyre et al. (2012) and Catalano (2012), in which the “fictitious” sphere with near-infinite radius is introduced to replace the rigid wall when generating the network. Fig.3.7 depicts such definition in 2D. (Also see Fig.3.1b, assuming $R \rightarrow +\infty$, P'_1 , P_1 , P_2 and P'_2 become aligned.) Fig.3.8 and Fig.3.9 show the definition of pore body and throat at the boundaries. The main advantage of this method is that it will not introduce new geometrical terms. The definition of pores shape and connections in proximity to the boundaries don't need introduce any additional assumptions. All algorithms above are suitable to handle the pores near the boundaries. Consequently, the resultant fluid forces at boundaries can also easily be assigned. A more detailed definition of the pores shape at the boundaries can be found in Catalano (2012).

From a practical point of view, the objective of 2PFV-DEM is to mimic the realistic drainage tests on finite-sized samples. The invasion of NW-phase starts from one side of the sample and the W-phase is drained from another side. Thus, we define the pores near these two boundary sides connecting to the NW and W reservoirs, respectively. They will remain in the initial state throughout the drainage simulations (i.e., constantly occupied by the same phase). Correspondingly, the calculation of saturation will not involve the volume of these boundary pores.

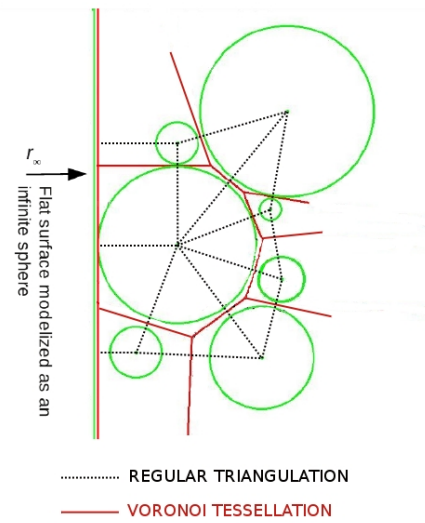


Figure 3.7: The definition of boundary condition by using “fictitious spheres”, after Catalano (2012)

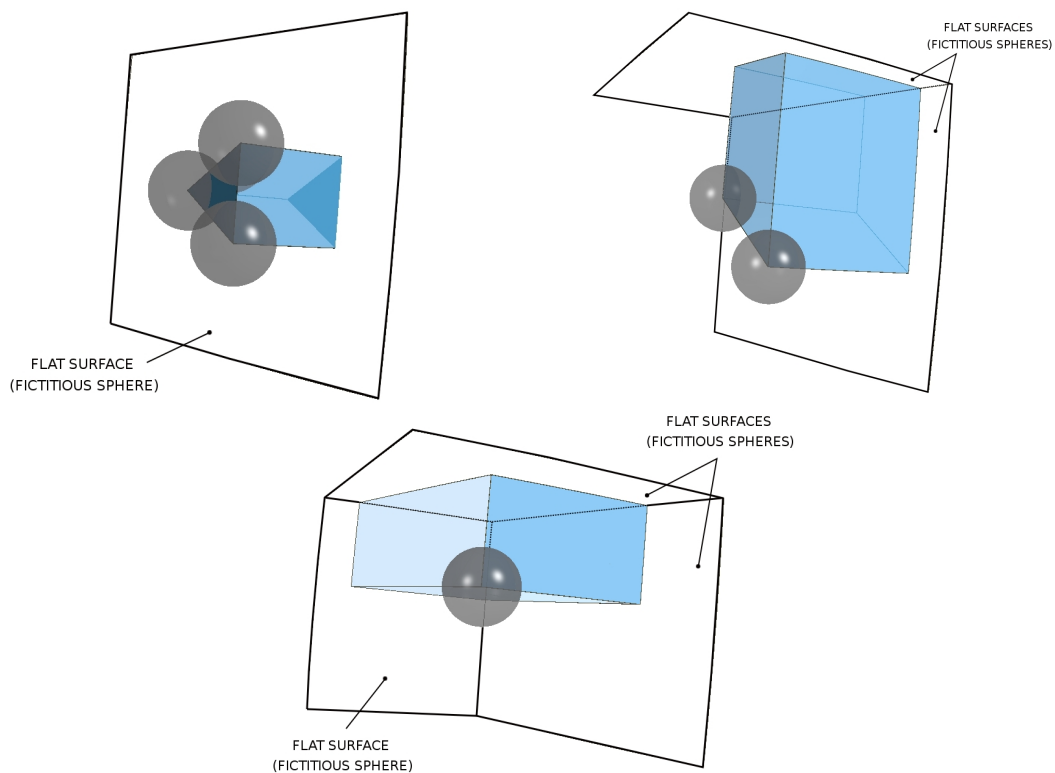


Figure 3.8: Pores at boundaries ,following Catalano (2012). (a) One fictitious, (b) Two fictitious and (c) three fictitious.

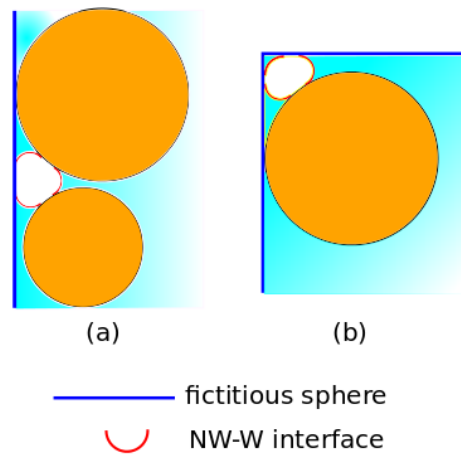


Figure 3.9: Pore throat at boundaries (a) 1 boundary + 2 spheres and (b) 2 boundaries + 1 sphere

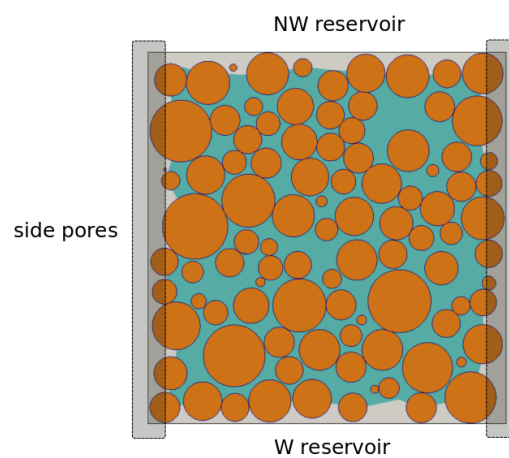


Figure 3.10: The fluid boundary condition of 2PFV model (in 2D for clarity).

Special attention has been paid to the connectivity of side boundary pores and throats (located between a vertical wall and the first layer of spheres along this wall, see fig.3.10). It will be seen that they can play a dominant role in the drainage process, in agreement with Chandler et al. (1982) (more discussion will be presented in Section 5.4).

In the model, we can decide whether such pores should be available for invasion or just disregarded and not participating to the system. We term them “*open-side*” drainage and “*closed-side*” drainage, separately. The latter case is hardly related to any realistic test condition although it may mimic the effect of a rough boundary or membrane boundary. It is introduced to enable interesting comparisons, mainly. The calculations of saturation are adapted to the different scenarios and exclude the boundary pores when they are closed.

3.3 Forces on the solid phase

During the drainage, the re-distribution of fluid phases will cause mechanical response on the solid phase. The main work for this section is to formulate the fluid forces induced by such evolution.

The total force \mathbf{F}^k generated on particle k by the two-phase fluid includes the effects of fluids pressures p and S-NW-W interfacial tensions γ ,

$$\mathbf{F}^k = \int_{\partial\Gamma_k} p \mathbf{n} ds + \int_{\partial\Phi \cap \Theta \cap \Gamma_k} \gamma \mathbf{n} dl = \mathbf{F}^{c,k} + \mathbf{F}^{t,k} \quad (3.11)$$

According to the Regular Triangulation of the structure, the network topology not only decomposes the void space of fluids but also discretizes the volume of particles. The forces $\mathbf{F}^{c,k}$ and $\mathbf{F}^{t,k}$ can be separately solved based on the geometry of pores and throats .

3.3.1 Integration of fluid-phase pressure

As mentioned in previous section, we assume that one pore can only be filled by a single fluid phase at the same time. Assuming pore i is incident to particle k (see Fig.3.5), the fluid force $\mathbf{F}_i^{c,k}$ induced by i on k can be written,

$$\mathbf{F}_i^{c,k} = \int_{\partial\Gamma_k \cap \Omega_i} p_i \mathbf{n} ds = \begin{cases} \int_{\partial\Gamma_k \cap \Phi_i} p_i^n \mathbf{n} ds & \text{: if } \Omega_i \text{ is occupied by NW-phase (i.e., } p_i = p_i^n \text{)} \\ \int_{\partial\Gamma_k \cap \Theta_i} p_i^w \mathbf{n} ds & \text{: if } \Omega_i \text{ is occupied by W-phase (i.e., } p_i = p_i^w \text{)} \end{cases} \quad (3.12)$$

Again, computing such integrals on spherical triangles in 3D could be computationally expensive. We project the pressure on the conjugate planar parts (angular sectors) of the closed domain $\Gamma_k \cap \partial\Omega_i$, whose trace in the plane of Fig.3.5(b) corresponds to segments $O_k O_k'$ and $O_k O_k''$.

3.3.2 Integration of interfacial tension

The interfacial tension is only taken into account when solid phase contacts with both NW-phase and W-phase. To integrate the interfacial tension forces, we keep using the

symbolic labels of Fig.3.5, in which Ω_{ij} is involving the S-NW-W contacting scenario. We first define the total tension force \mathbf{F}_{ij}^t , applied on the solid phase in Ω_{ij} . Since Ω_{ij} intersects three spheres, \mathbf{F}_{ij}^t will have to be later split into three terms. \mathbf{F}_{ij}^t is defined as:

$$\mathbf{F}_{ij}^t = \int_{\partial\Phi_i \cap \Theta_j \cap S_{ij}} \gamma \mathbf{n} dl \quad (3.13)$$

which has been obtained by following Eq.3.7 and Eq.3.9 when calculating p_e^c , but it can not be directly utilized here. Because at the instance of NW-phase invading through the pore throat, the contour of throat, i.e., the contact lines in Fig.3.3(b), is in a transient state. The pore will be drained simultaneously, leading to the length of NW-S contact lines L_{ns} increasing and the length of W-S contact lines L_{ws} decreasing. The NW-W interface extends into the pore body by covering the particles. So the interfacial tension force on S-phase need to be redefined by,

$$\mathbf{F}_{ij}^{t*} = \int_{\partial^s \Phi_i \cap \Theta_j} \gamma^{nw} \mathbf{n} dl \quad (3.14)$$

in which the new NW-W-S contact lines have to be defined. Such contact lines are irregular and difficult to be determined. But the new balance of NW-W interface can be obtained by,

$$\sum \mathbf{F}_{ij} = \mathbf{F}_{ij}^{c*} + \mathbf{F}_{ij}^{t*} = 0 \quad (3.15)$$

where \mathbf{F}_{ij}^{c*} is the phase pressure effects. \mathbf{F}_{ij}^{c*} can be estimated by projecting on S_{ij} with,

$$\mathbf{F}_{ij}^{c*} = \int_{\partial\Phi_i \cap \Theta_j} (p^n - p^w) \mathbf{n} ds \simeq A_{ij}^f (p^n - p^w) \mathbf{n} \quad (3.16)$$

in which, A_{ij}^f is the pore throat sectional area conjugating facet S_{ij} . Combining Eq.3.14-3.16, the total tension force can be obtained:

$$\mathbf{F}_{ij}^{t*} = -A_{ij}^f (p^n - p^w) \mathbf{n} \quad (3.17)$$

In order to define the interfacial tension force applied on each of the three spheres intersecting Ω_{ij} , it is assumed that the force on sphere k is proportional to the contact line on that sphere contained in the subdomain. If δ_{ij}^k denotes the length of the curved contact line $\partial\Gamma_k \cap S_{ij}$, the force on sphere k then reads:

$$\mathbf{F}_{ij}^{t*,k} = \mathbf{F}_{ij}^{t*} \frac{\delta_{ij}^k}{\sum_{k=1}^3 \delta_{ij}^k} \quad (3.18)$$

Note that when iterating over all domains Ω_i adjacent to one particle, the integral on interfacial contact line of δ_{ij}^k length should be calculated only once.

Finally, the total force on one particle is obtained by summing interfacial tension and pressure forces from all incident facets and contact lines:

$$\mathbf{F}^k = \sum_{(ij) \text{ incident}} \{ \mathbf{F}_i^{c,k} + \mathbf{F}_{ij}^{t*,k} \} \quad (3.19)$$

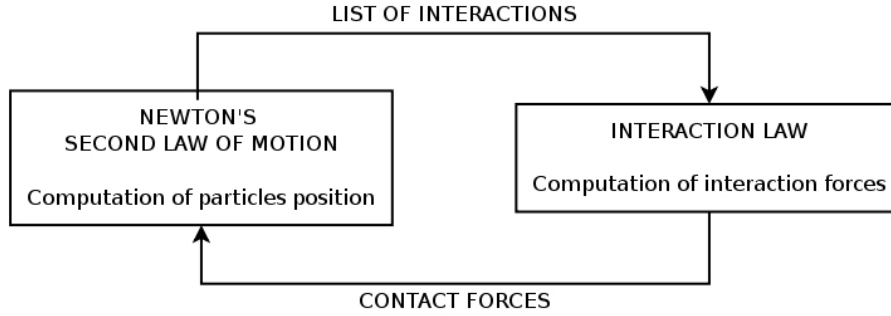


Figure 3.11: Computation cycle of a DEM model.

3.3.3 Coupling with DEM

After solving the fluid forces on solid phase, the DEM framework can be employed for handling the mechanical couplings. According to the principles of DEM (Cundall and Strack, 1979),

“the equilibrium contact forces and displacements of a stressed assembly of particles are found through a series of calculations tracing the movements of individual particles. These movements are the results of the propagation through the medium of disturbances originating at the boundaries: a dynamic process. The speed of propagation is function of the physical properties of the discrete medium.”

Fig.3.11 depicts such principles, in which the computational cycle of the DEM computation is shown.

In the 2PFV-DEM coupling, the hydraulic and mechanical behaviors are both assumed in the quasi-static regime, in which the displacements of W-NW interface and the forces induced by such displacements are only considered in a sequences of individual equilibrium states. We assume during each transient moment the capillary effects, i.e., the forces induced by the two fluid phases are constant. Such forces can be considered as “the medium of disturbances” and will be directly taken into account for solving “the equilibrium contact forces and displacements”. To sum up, the mechanical response of the unsaturated granular media can be considered as the sum effects of the dry granular medium mechanical behavior and the two-phase fluid capillary actions.

Computation cycle

As mentioned in the introduction of this chapter, the solid particles are idealized as spheres interacting with each other. In an oriented space of dimensions i ($i = 1, 2, 3$ in 3D), each sphere can be identified by its radius R , mass m and moment of inertia I_i . The motion of a sphere can be characterized by its position x_i , translational velocity \dot{x}_i and rotational velocity ω_i . The translational and rotational accelerations can be calculated by the Newton’s second law of motion:

$$\ddot{x}_i = F_i/m \quad (3.20)$$

$$\dot{\omega}_i = M_i/I_i \quad (3.21)$$

where F_i and M_i are the forces and moments applied to each particle. Considering the couplings, Eq.3.20 can be expressed by:

$$m\ddot{x}_i = F_i^c + mg + F_i^f \quad (3.22)$$

where F_i^c and F_i^f are the contributions of contact forces and fluid force, respectively, and g is the gravitational acceleration. F_i^c is defined by the interaction law which will be described in next section. F_i^f can be obtained by following Eq.3.19.

To follow the evolution of the system in time, particles position are updated at each time step Δt by integration of the accelerations \ddot{x}_i and $\ddot{\omega}_i$ according to a first-order centered finite difference scheme. We have:

$$\begin{aligned} \dot{x}_i^{[t+\Delta t/2]} &= \dot{x}_i^{[t-\Delta t/2]} + (\ddot{x}_i^{[t]} + g) \cdot \Delta t \\ \dot{\omega}_i^{[t+\Delta t/2]} &= \dot{\omega}_i^{[t-\Delta t/2]} + \ddot{\omega}_i^{[t]} \cdot \Delta t \end{aligned} \quad (3.23)$$

where \dot{x}_i and $\dot{\omega}_i$ are evaluated at time $t + \Delta t/2$. The new particles position at time $t + \Delta t$ are calculated by:

$$x_i^{[t+\Delta t]} = x_i^{[t]} + \dot{x}_i^{[t+\Delta t/2]} \cdot \Delta t \quad (3.24)$$

Once the new position of each particle is obtained, the list of interactions will be updated. Consequently, the new interaction forces will be computed.

Contact definition

The contact model determines the micro-scale force-displacement relationship of the interactions, by which the contact force can be obtained. In the simplest case, the relationship is defined by a normal stiffness k_n , a tangential stiffness k_t and an inter-granular friction angle ϕ_c , i.e., the traditional Cundall's linear elastic-plastic law (Cundall and Strack, 1979). For current implementation, there is no need to increase the complexity of the contact law. Thus, we keep using the simplest law hereafter. For other types of contact definitions in DEM, the coupling scheme is also allowed.

The contact force between two particles is the function of local displacement and local mechanical properties of the two particles. For the displacement, it can be expressed by the reference of particle geometry, i.e., the particles distance. We consider the negative distance as a ‘‘overlap’’, in which the two particles contact with each other. Such overlap reflects the deformation near the contact and can be formulated. In the simplest case, we define the normal particle displacement δ_c with the overlap by the following condition:

$$\delta_c = \begin{cases} U^n & U^n < 0 \\ 0 & U^n \geq 0 \end{cases} \quad (3.25)$$

where U_n is the overlap, or termed intergranular distance (see Fig.3.12a).

The components of contact force can be formulated by following Cundall and Strack (1979) (see fig.3.12b). The normal component \mathbf{F}_n is defined by:

$$\mathbf{F}_n = F_n \mathbf{n} = k_n \delta_c \mathbf{n} \quad (3.26)$$

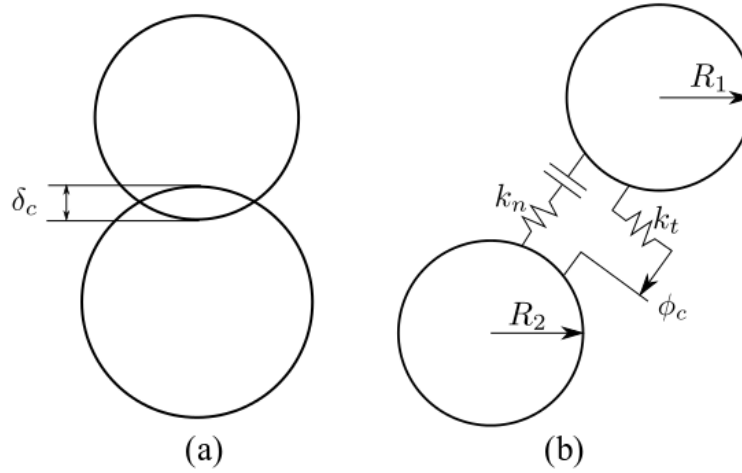


Figure 3.12: (a) Definition of normal particle displacement. (b) Normal and shear stiffnesses at contacts.

The tangential component \mathbf{F}_s is computed at each time step as function of the increment of tangential relative displacement Δu_s :

$$\Delta \mathbf{F}_s = F_s \mathbf{t} = k_t \Delta u_s \mathbf{t} \quad \rightarrow \quad \mathbf{F}_s^{(t)} = \mathbf{F}_s^{(t-\Delta t)} + \Delta \mathbf{F}_s^{(t)} \quad (3.27)$$

The normal stiffness k_n can be expressed by the global stiffness modulus E , and the harmonic mean of the interacting spheres' radius, R_1 and R_2 , as follows:

$$k_n = 2E \cdot \frac{R_1 \cdot R_2}{R_1 + R_2} \quad (3.28)$$

The shear stiffness k_t is defined as a fraction a of k_n , i.e.,

$$k_t = a k_n \quad (3.29)$$

The shear strength of the contact is defined by the Coulomb's criterion. We denote \mathbf{F}_s as the upper limit of the tangential force, it should satisfy the following condition:

$$\| \mathbf{F}_s \| \leq \mathbf{F}_n \tan \phi_c \quad (3.30)$$

where $\tan \phi_c$ is the intergranular friction angle. To sum up, the constitutive relationship can be depicted by Fig.3.13.

Conclusions

The pore-scale network has been established using the Regular Triangulation method. The local rules and governing equations have been shown. Two modeling assumptions, i.e., the short-term/with-trap and long-term/without-trap simulations, have been proposed. The hydromechanical coupling strategy has been elaborated. The detailed implementation is explained in next chapter.

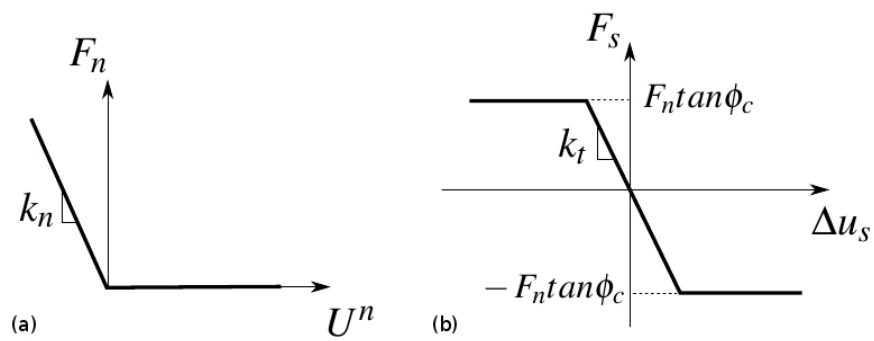


Figure 3.13: Elastic-plastic contact model. Normal (a) and tangential (b) interaction law (Catalano, 2012)

Chapter 4

Implementation and model test

4.1 Implementation

4.1.1 The open-source code YADE

The implementation of 2PFV-DEM model is based on the open-source code “Yet Another Dynamical Engine” (YADE) platform. The code YADE is an extensible open-source framework for discrete numerical models, focused on Discrete Element Method. The computation parts are written in c++ using flexible object model. Python is used for rapid and concise scene construction, simulation control, postprocessing and debugging (Šmilauer et al., 2015). Thanks to the open source licensing (GNU General Public License), the developers and users of Yade, the capability of the code is continuously increasing.

4.1.2 Coupling design

Network definition

The network generation has been implemented in C++ as part of YADE, with the help of “The Computational Geometry Algorithms Library” (CGAL) (Boissonnat et al., 2000). CGAL ensures exact predications and constructions, and provides very efficient algorithms for regular triangulation (Liu and Snoeyink, 2005). Initially, the regular triangulation and its dual Voronoi tessellation were proposed for solving the one-phase flow problems (Chareyre et al., 2012). Concerning the requirements for two-phase flow, currently only the regular triangulation is involved in the model. The network generation has been complemented with the set of functions for the determination of entry capillary pressure (Eq.3.10), updating the state flags and connectivity flags (section 3.2.2), and determination of fluid forces on the solid particles (Eq.3.19).

It is worthwhile to clarify that the current network definition in 2PFV-DEM model is static. We suppose that during the drainage only elastic deformation of small amplitude will be generated on the solid skeleton. Thus, the topology between solid phase and fluid space is considered to be fixed, although the solid grains may move due to the actions of intergranular contact forces. Consequently, the volume and geometry of the pores will not change for the computation. The movement of solid particles is simulated using DEM. As a result, the elastic deformation of the solid skeleton can be obtained. These assumptions

will be held hereafter in the thesis. They may be relaxed in future extensions of the current model.

Implementation of 2PFV

After the network generation, the 2PFV model is ready to be implemented. Fig.4.1 shows the flow chart for the 2PFV model only. Since the network topology is fixed, the geometry dependent terms, such as the volume of the pores and the entry capillary pressure of the throats, can be pre-calculated and saved with the topology information in the step “Network generation”. As mentioned in section 3.2.2, in the “update boundary condition” step, the hydraulic boundary conditions are controlled by changing the fluids pressure of the reservoirs. The drainage and entrapment detection are implemented in the step “Two-phase flow calculation”. With the help of the recursion algorithm, the drainage procedure can be expressed by changing the information of saturation, pressure and connectivity flag for each pore. The fluid forces on solid phase are determined by following the algorithm of section 3.3. Finally, the 2PFV model can be coupled with DEM by following Eq.3.22. Fig.4.2 shows a schematized view of the final coupled algorithm.

As mentioned in section 3.2.2, considering the possibility of connections between individual W-phase clusters, both “*with-trap*” and “*without-trap*” drainage are implemented in the model. Considering the side boundaries conditions in which the side pores may be available for invasion or not, the options of “*open-side*” and “*closed-side*” are also implemented.

Yade uses Python language for simulation control. The following code fragment (Listing 4.1) illustrates how the 2PFV module is introduced in a simulation setup (in Yade it appears as one optional *engine*). This example is a sub-part of the script used for the simulation presented in the thesis.

Listing 4.1: Introducing the 2PFV engine in a coupled DEM simulation

```
##The preamble of the script should setup a regular DEM simulation,
  defining particles properties and boundary conditions

##Instantiate a two-phase engine
unsat=UnsaturatedEngine()

##set boundary conditions for the fluid phases, the drainage is controlled
  by decreasing W-phase pressure (pw) and keeping NW-phase pressure (pn
  ) constant.
unsat.bndCondIsPressure=[0,0,1,1,0,0]
unsat.bndCondValue=[0,0,pw_initial,pn,0,0]
unsat.isPhaseTrapped=True #if True, "with-trap" drainage; if False, "
  without-trap" drainage.
unsat.isInvadeBoundary=True #if True, "open-side"; if False, "closed-side
  ".
unsat.initialization()
unsat.surfaceTension = surfaceTension
```

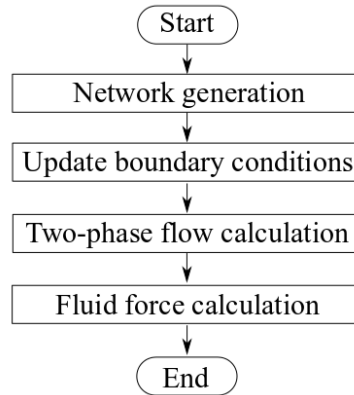


Figure 4.1: The 2PFV algorithm (one invasion step)

```

##start the invasion, the data of pc-sw-strain will be written into
pc_sw_strain.txt
file=open('pc_sw_strain.txt',"w")
for pw in arange(pw_initial,pw_end,pw_step): #decrease pw progressively
from pw_initial to pw_end, with a step of pw_step
  unsat.bndCondValue=[0,0,pw,pn,0,0]
  unsat.invasion()
  unsat.computeCapillaryForce()
  # Add the fluid and interfacial forces to the total force on each body
  for b in O.bodies:
    O.forces.addF(b.id, unsat.fluidForce(b.id), True)
  # then integrate the dynamics with these additional forces until a new
equilibrium state is reached
  while 1:
    O.run(1000,True)
    unb=unbalancedForce()
    if unb<0.01:
      break
  file.write(str(pn-pw)+"_□"+ str(unsat.getSaturation(True))+"_□"+str(-triax
    .strain[1]-ei1_initial)+"\n")
file.close()
  
```

To summarize, the library CGAL was employed for the triangulation procedure to build the explicit topological links between the fluid phases and solid structure. The invasion criterion for fluid phases was formulated and implemented based on the pore network. In turns the resulted fluid forces on solid phase was obtained. Such forces were coupled with the discrete element method by following the law of motion and has been implemented in the open-source code YADE. The mechanics of solid phase finally has been modeled.

4.2 Model test

In this section, we show an example simulation with the 2PFV-DEM model, in which the primary drainage test will be performed. The main objects are to obtain the capillary

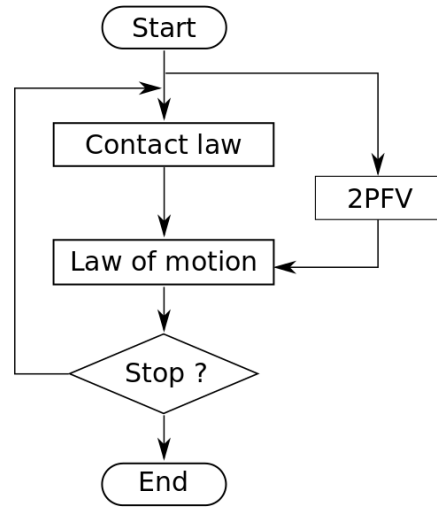


Figure 4.2: Computation cycle of 2PFV-DEM

pressure-saturation ($p^c - s^w$) curve (or termed “*water retention curve*” (*WRC*) in unsaturated soil mechanics) and to reproduce the evolution of the deformation of solid skeleton.

4.2.1 Numerical setup

The sample of the test is composed of poly-disperse spheres, which is generated by the DEM software Yade (Šmilauer et al., 2015). We assume the top and bottom boundaries of the sample are connected to the NW-reservoir and W-reservoir, respectively. There are no flux or pressure exchange between the side boundaries and the bulk. However, the NW-phase can invade the side pores through the throats near the boundaries or through the throats inside the bulk from the NW-reservoir, i.e., “open-side” drainage is performed. We also want to present the effects of the connectivity between the W-reservoir and W-phase clusters, so both “with-trap” drainage and “without-trap” drainage are simulated.

We assume the initial state for phases pressures is: $p^c = p^n - p^w = 0$, corresponding to the saturated scenarios. Drainage is carried out by decreasing p^w in a stepwise manner and keeping p^n constant. The simulation is performed under the oedometer test conditions, in which the one-dimensional deformation induced by drainage is observed. To simulate these conditions, rigid confining walls are introduced to prevent lateral displacement of the sample. The bottom is fixed. The top is a free plane, and its confining stress is kept constant as the initial state.

For more generality, the simulation results are all given in dimensionless forms hereafter. The capillary pressure p^c can be normalized by,

$$\bar{p}^c = \frac{p^c \bar{D}}{\gamma^{nw}} \quad (4.1)$$

in which, \bar{p}^c is termed normalized capillary pressure, γ^{nw} is NW-W interfacial tension and \bar{D} is the average sphere size.

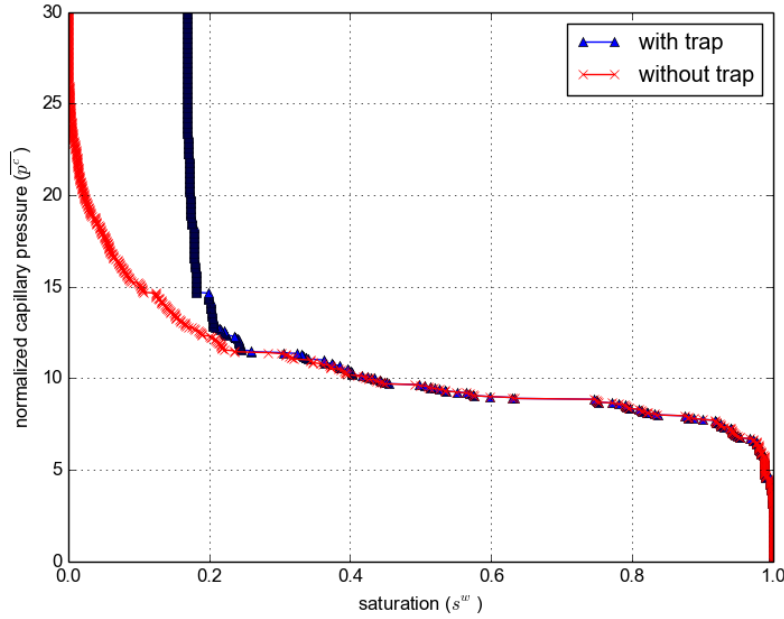


Figure 4.3: The water retention curves ($\bar{p}^c - s^w$) of drainage simulation. The sample is a dense cubic packing of 1000 spheres.

4.2.2 Results and discussions

Normalized capillary pressure - saturation relationship

A series of test on cubic packings has been performed. For both “with-trap” and “without-trap” simulations, the normalized capillary pressure - saturation ($\bar{p}^c - s^w$) curves have been achieved as shown in Fig.4.3. The evolution of W-phase retention are similar. The sample is saturated until the first entry of NW-phase. The corresponding p^c may be termed “air entry value/suction” in some macro-scale continuum-based models. Then s^w shows discontinuous reduction, because the distribution of p_e^c is heterogeneous. The gradients of s^w , i.e., the localization of s^w will be discussed in chapter 5. The sharp decrease of s^w during $6.5 < \bar{p}^c < 11.0$ can be considered as the consequence of the recursive cascade of “Haines jumps”. The main difference between two drainage simulation is the residual W-phase saturation, in which $s^w \simeq 0.18$ in “with-trap” drainage and $s^w \rightarrow 0$ in “without-trap” drainage.

Invasion characteristics

We observe the characteristics of NW-phase invasion by cutting a slice of one sample, as shown in Fig.4.4. When increasing \bar{p}^c , the invasion starts from the pore with larger throat, in which the entry capillary pressure is smaller (see slice.(a)). We can observe that the NW-phase invades the side pores first as shown in slice.(a) and (b). That is because the throats at the boundaries are composed by the regular sphere(s) and the fictitious sphere(s) with near-infinite radius (see Fig.3.9). The p_e^c of these throats is in average smaller than that of throats in the bulk. We will further analyze the boundary effects in section 5.4.

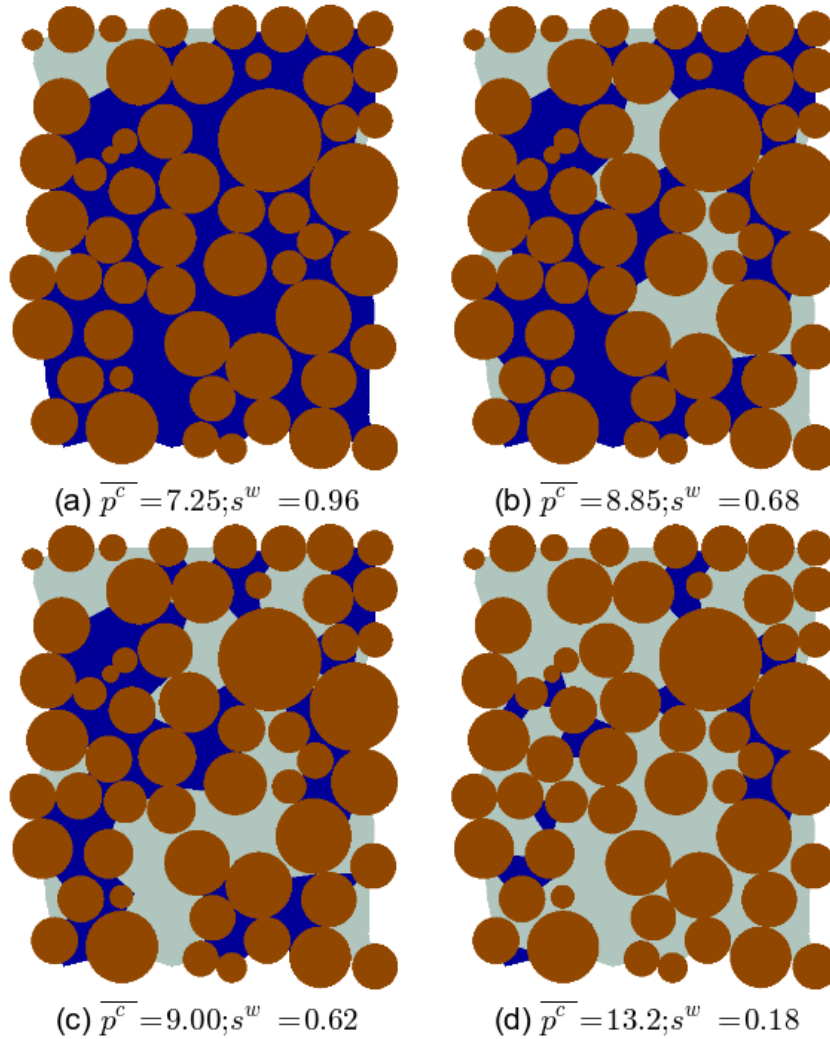


Figure 4.4: The process of drainage (400 particles), NW-phase invade from top. Brown (gray) is solid phase, blue (black) is W-phase, and light cyan (white) is NW-phase, see color version of this figure in the HTML.

Comparing slices.(b) and (c) shows that under certain circumstances even a very small change in capillary pressure can cause a significant displacement of the NW-W interfaces. For such event, Haines jumps go through large cluster of pores, causing a sharp decrease of W-phase content. Slice.(d) shows the end of the simulation in “with-trap” drainage, in which all the remaining W-phase is in the form of disconnected clusters entrapped by the NW-phase. However, the W-phase will be completely drained if the “without-trap” drainage is performed.

Distribution of fluid pressure

In “with-trap” drainage, the model is neglecting W-phase transport by film flow or evaporation, these disconnected phases will never disappear. As explained in section 3.2.2, the trapping sequences result in a different p^w in each disconnected cluster. An example of this feature is shown in Fig.4.5.

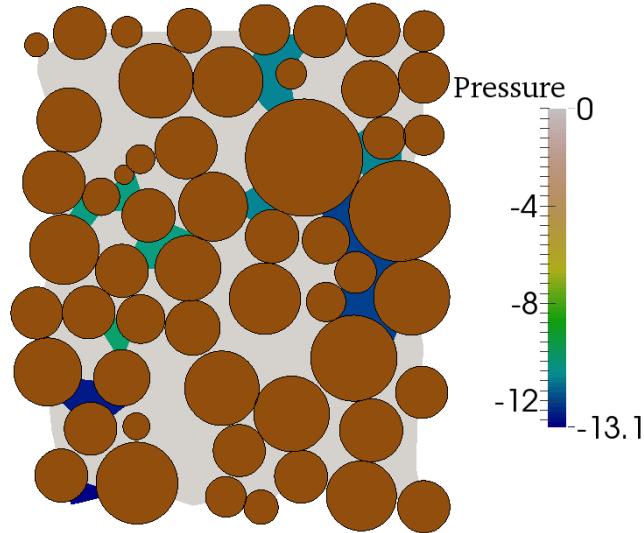


Figure 4.5: Distribution of capillary pressure in “with-trap” mode of drainage. Brown circle is solid phase, light region is NW-phase pressure p^n , dark regions are W-phase pressures p^w , see color version of this figure in the HTML.

The results lead us to conclude that the definition of capillary pressure is not only a macro-scale terminology but also has micro-scale interpretations. In most macro-scale continuum-based models, the micro-scale capillary pressure/suction is seldom mentioned. Usually, it is considered as an input parameter at macro-scale, which is only related to the reservoirs (i.e., hydraulic boundary conditions). In 2PFV model, the micro-scale capillary pressure is a consequence of the drainage. (Essentially, it is determined by the micro-structure of pore space.) In Fig.4.5, from the pressure distribution we can determine the order of the disconnections, with the larger p^w corresponding to earlier entrapment. The localization of capillary pressure is not only an important characteristic of the hydraulic evolution, but also affects the mechanical behavior of solid skeleton. We will further discuss this in chapter 6.

By contrast, a simpler case, the disconnected clusters of W-phase may be evacuated in long terms leading to complete drainage in the “without-trap” drainage simulation. In this situation, the pressure exchange and mass transfer between different W-phase clusters are allowed. Consequently, the pressures of W-phase clusters have the same value in each invasion event. A profile is shown in Fig.4.6.

Deformation of solid skeleton

The forces on solid particles induced by the fluids have been formulated in Section.3.3. Fig.4.7 depicts the effects of such fluid forces. In zoom (b), the forces are caused by the disconnected W-phase, and the involved solid particles are attracted under funicular regime by the capillary pressure. Zoom (c) shows the fluid forces near the W-phase front. Such fluid forces result in the macroscopic deformation. In this situation, there are nearly no sliding contacts and the response can be considered elastic.

The evolution of one-dimensional deformation is shown in Fig.4.8, in which the relationship between strain component - normalized capillary pressure ($\varepsilon_{11} - \bar{p}^c$) is reported.

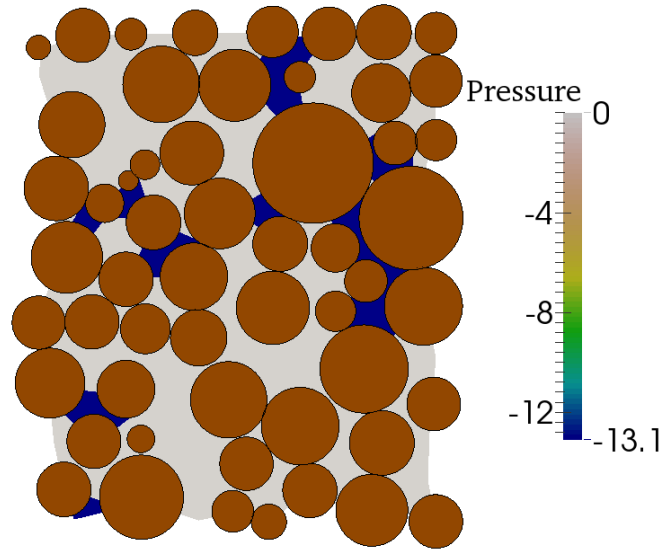


Figure 4.6: Distribution of capillary pressure in “without-trap” mode of drainage. Brown circle is solid phase, light region is NW-phase pressure p^n , dark regions are W-phase pressures p^w , see color version of this figure in the HTML.

In both “with-trap” and “without-trap” tests, the results are similar, in which the samples first shrink and then swell.

Under the elastic regime, the sample can recover its shape if the W-phase is drained completely (i.e., without-trap drainage). If the W-phase is trapped by NW-phase in the medium, the sample can not swell back to its shape even the capillary pressure grows. In general, the shape of the sample shrinks at the end in this situation. The theoretical analysis of the deformation in detail will be presented in chapter 6.

4.2.3 Comparison with experiments

We verify the model by comparing the simulation results with experimental data from a quasi-static drainage experiment in a synthetic porous medium of Culligan et al. (2004). Unfortunately, we could not find more micro-scale/pore-scale experimental data related to the deformation of solid skeleton in Culligan et al. (2004) or other literatures. Thus, the comparison mainly focus on the hydraulic results, i.e., the capillary pressure - saturation relationship.

Numerical setup

In experiment of Culligan et al. (2004), the measurements were done on packed glass beads, contained in a column of 70 mm in length and 7 mm in diameter. The particle size distribution (PSD) of the glass beads was as in Table. 4.1, and the porosity is 0.34. The drainage was carried out by pumping water out of the porous medium. X-ray tomography was used to image only a small part of the column (a cubic box of size 5 mm approximately) to determine capillary pressure-saturation ($p^c - s^w$) relationships.

Due to some properties of the regular triangulation, generating the pore-space decomposition for a column of circular cross-section (as in the experiment) would have been

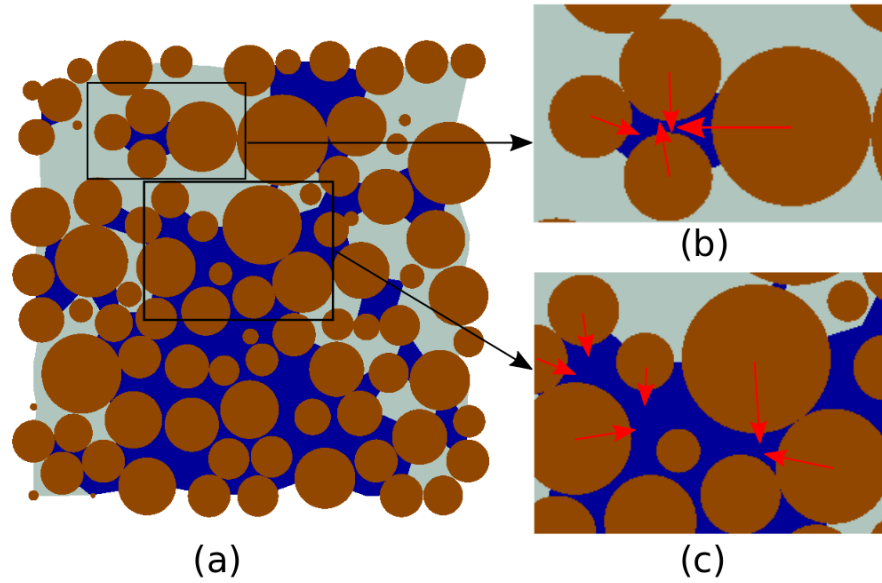


Figure 4.7: Forces acting on solid particles induced by NW-W phase pressure and surface tension. Forces are shown in red arrows. Brown (gray) is solid phase, blue (black) is W-phase, and light cyan (white) is NW-phase, see color version of this figure in the HTML. (b) forces acting from disconnected W-phase. (c) forces acting from W-phase front. (in 2D for clarity)

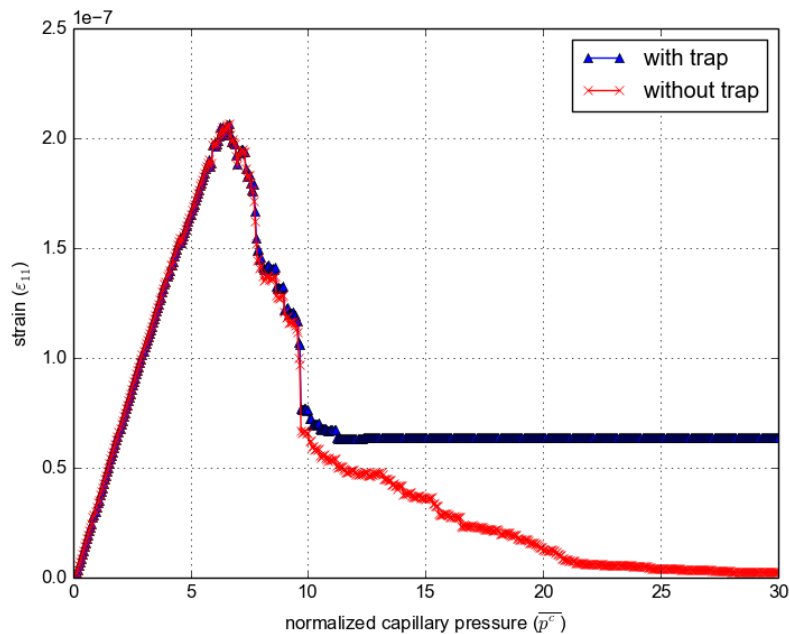


Figure 4.8: The relationship between normalized capillary pressure and one-dimensional deformation ($\bar{p}^c - \epsilon_{11}$) in drainage simulation under the oedometer test conditions. The sample is a dense cubic packing of 1000 spheres.

Weight(%)	Diameter(mm)
30	1-1.4
35	0.850
35	0.600

Table 4.1: Particle size distribution of the experiment

excessively complex in the present state of the algorithms. Instead, cuboid samples are generated, with the same average properties as the experiments in terms of PSD and porosity. The simulated packings are connected to the NW reservoir at the top, and to the W reservoir at the bottom, as in figure 3.6. The drainage process is simulated by imposing a progressive increase of the NW-phase pressure in the NW-reservoir (and keeping the W-phase pressure constant). There is no gravity in the model. Since gravitational problems are equivalent to non-gravitational ones if piezometric pressure is used in lieu of absolute pressure, it does not induce a loss of generality as long as gravity does not modify the curvature of the interfaces (a rather good approximation for air-water systems with grain size below 1 mm (Pitois et al., 2001)).

Due to capillary fingering, the situation at the boundaries of the window accessible by tomography is difficult to define precisely. In the simulation, it may be assumed that only a few large pores of the boundaries are connected to the invading phase reservoir (reflecting fingering in that part of the column not scanned, with some fingers reaching the scan region). Conversely, it may be assumed that all pores of the boundary associated to the NW-phase reservoir are occupied by the NW-phase. The two variants could lead to significant differences in the results in some circumstances (Joekar-Niasar et al., 2010b). In our case, preferential invasion along the boundaries (an effect which we will discuss in details in section 5.4) reduces significantly the influence of the reservoir connectivity. For the sake of simplicity we use the last assumption, i.e., uniform boundary conditions on the top and bottom faces of the box.

For one simulation, a cubic box of size 5.0 mm × 6.0 mm × 5.0 mm is defined in which 400 spheres are densely packed. Consistently with the experimental setup, where the boundaries are smooth and rigid, we suppose that the NW-phase can invade along the side boundaries (the “open-side” condition). According to the experimental results, the residual saturation is not zero. Thus, we apply the “with-trap” condition in the simulation.

The random packings are generated by DEM simulations. The PSD and porosity are defined as in the experiment. In order to reach the target value of porosity we employ a growth algorithm based on the REFD method (radius expansion-friction decrease) (Chareyre et al., 2002). This dynamic compaction method lets one control the porosity and it gives statistically homogeneous and isotropic microstructures. After this generation phase, the positions of the spheres are fixed. They don't move further during the drainage phase. For more generality, the data from experiment and simulations are all given in dimensionless forms, in which p^c is normalized by Eq.4.1.

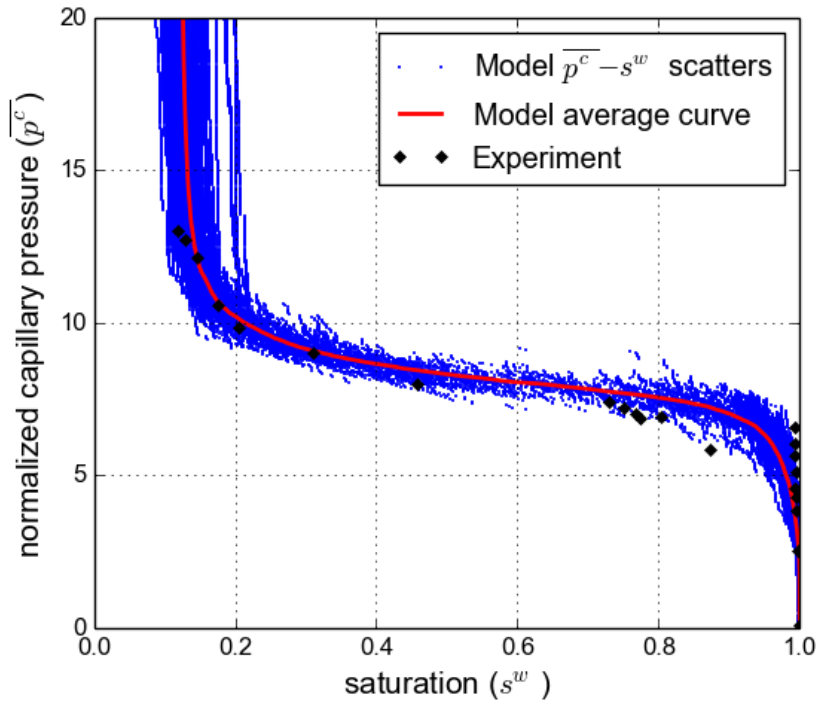


Figure 4.9: Comparison between simulation and experiment for primary drainage $\bar{p}^c - s^w$ curves. The number of observations of simulation is 100.

Results and discussion

Using the technique described above, we compute the primary drainage process for 100 random packings having the same PSD and porosity. Fig.4.9 presents the results of these simulations, in which we gather all scattered (\bar{p}^c, s^w) points of each simulation in one image. As shown in Fig.4.9, although all packings share the same macro-scale parameters, the $\bar{p}^c - s^w$ curves still have a distinct variability. Especially, the residual saturation can differ significantly from one sample to another. This erratic dispersion could be reduced by enlarging the sample size. This trend will be discussed in chapter 5. For the moment we keep the number of particles approximately equal to the number of particles in the scanned domain of the experiment.

The $\bar{p}^c - s^w$ curves show a rather good agreement between the simulations and the experiments. The experimental data points are in the range of simulation (\bar{p}^c, s^w) scatters, although the averaged curve differs slightly from the experimental one. It can be explained by the simplifications done in the drainage model, by the fact that the real conditions are not well reflected in the boundary conditions of the subdomain or of the sample itself (cubic packing versus circular cross-section).

Conclusions

In this part, we have presented a pore-scale hydromechanical coupling scheme, termed as 2PFV-DEM model. This model is devoted to simulate the quasi-static two-phase flow in deformable poly-disperse granular materials, specially for the primary drainage of initially saturated media. The idea of the model is to combine a pore-scale network and the DEM for the fluid phases and the solid phase, respectively. The network has been established using the Regular Triangulation and it explicitly links the geometry of the fluid space and the positions of the solid grains.

- In the proposed decomposition the pore throats are planar objects defined by the facets of the triangulation, while all the pore space is contained in the volume of the pore bodies. Drainage occurs by a recursive invasion of the pores when the capillary pressure exceeds the local threshold values (“entry capillary pressure”). Theoretical formulas for calculating geometrical properties and entry capillary pressure for given pores have been developed by extending the Mayer and Stowe-Princen (MS-P) theory of drainage.
- The capillary forces induced by the motion of the fluid/fluid interface have been formulated based on the topology of the network. Such forces have been directly taken into account for solving the equilibrium contact forces and displacements of the solid grains in the framework of DEM. As a consequence, the macro-scale deformation of solid structure has been obtained.
- One key model attribution is its capability to trap the receding W-phase. Considering the possible drainage procedures (under a short-term or a long-term), the model allows two options: (1) allowing that the receding W-phase is able to be trapped by the NW-phase and results in a residual saturation and a localization of capillary pressure; (2) assuming the W-phase is drained completely. Another model feature is its optional side boundary conditions. To accommodate different experimental situations, the pore throats of the side boundary can be considered open or closed.
- The model has been implemented in C++ as a module of the open-source code YADE-DEM. A series of drainage tests has been performed under the oedometer conditions. The results of the wetting phase retention curve and the one-dimensional solid deformation has been reported, in which the solid skeleton showed first shrinking and then swelling. The hydraulic component has been verified by comparing with the experimental data of Culligan et al. (2004). The simulations are in good agreement with experiments in terms of $\bar{p}^c - s^w$ relation.

Part III

Applications of the model

Chapter 5

Finite size effects and the representative elementary volume

5.1 Introduction

¹In practice one never deals with infinite systems and it is necessary to understand the effects of sample size, sample shape, and gradients of state variables. This difficulty exists in both experiments and numerical simulations of - so called - representative element volume (REV). It is amplified in the context of microscale experiments and simulations since they tend to study domains of smaller size compared to conventional lab or field experiments.

REV often refers to a sample size sufficiently large to provide statistical robustness to an averaging procedure (Bear, 1972). This definition is rather clear and its application is straightforward if the variable of interest is the average porosity of a statistically homogeneous material, for instance. In such case statistics generated by sub-sampling a large domain are enough to determine variance reduction as a function of size: the variance σ^2 decreases as α/V as soon as $V \gg \alpha$, where α depends on the size of the heterogeneities and V is the sampled volume (σ is the standard deviation). Defining the volume by the number of spheres it contains leads to an equivalent proportionality between σ and $1/\sqrt{N}$. Knowing α , the REV size depends only on the decision of which variance it tolerated for a single measurement. Moreover, the excessive variability of results on small samples can always be mitigated by averaging the results on many samples.

It is very important to note that in the above context the minimal REV size is not a fixed value. It depends strongly on the tolerated deviation (a tolerated standard deviation decreased by 10 results in REV volume multiplied by 100). This is overlooked in many papers in which some differences are said “negligible” without a clear definition of how small “negligible” is, which makes the determination of α impossible.

Two phase flow (among other processes) adds complexity to the problem in a way which is not always very well acknowledged. The question is not only to control the scattering of results, but also to make sure that the drainage process itself is not influenced by the size (and shape) of the sample. In other words there is a need to know if, for a particular p^c imposed on samples, the saturation will be simply distributed around a

¹This chapter has been published as part of journal paper Yuan et al. (2015b)

unique size-independent mean value, or if the mean value itself can be biased by the sample size. In this chapter we examine both aspects, *i.e.*, 1) how samples of different sizes result in different values in average and 2) how the results on sub-samples fluctuate around the mean. The effect of sample shape is analyzed in the last part.

5.2 Sample size

We report a series of drainage tests with different sizes of cubic samples using 2PFV-DEM model. The number of spheres (N) ranges from 100 to 40,000, and for every N the simulations are repeated on 100 different sphere assemblies. For a given N the samples only differ in the positions of individual spheres. Porosity and PSD are the same as in the previous section. We assume the receding W-phase can be disconnected from its reservoir by the NW-phase, *i.e.*, “with-trap” drainage is performed. Both “open-side” and “closed-side” modes are considered in the tests for comparisons. The same averaging technique as shown in section 4.2.3 is used to manipulate the statistical results, *i.e.*, for each size of sample, an averaged $\bar{p}^c - s^w$ curve is achieved based on the 100 observations. For each \bar{p}^c value the standard deviation $\sigma(s^w)$ of saturation is calculated.

As seen in Fig.5.1 and Fig.5.2, the averaged $\bar{p}^c - s^w$ curves for different sizes are clearly distinct. In open-side drainage, the shift of the $\bar{p}^c - s^w$ curve with N is monotonic. Under the same \bar{p}^c , a larger N results in a larger s^w . In closed-side mode, the effect of N is more complex. The curves are not simply shifted as they intersect each other. Drainage starts for smaller \bar{p}^c values in small samples. There is a transition near $\bar{p}^c = 10$ (corresponding to $s^w \simeq 0.7$), after which the ordering of the curves is reverted and small samples have larger degrees of saturation. A second inversion occurs before reaching the residual saturation ($\bar{p}^c \simeq 16$). The shapes of the curves are clearly different between Fig.5.1 and Fig.5.2 for $0.9 > s^w > 0.2$. In open-side drainage, all curves have very similar slopes while in closed-side drainage smaller samples have more shallow slopes.

In both drainage modes larger samples have larger residual saturation. A result which might be explained by the possibility to form clusters of trapped W-phase of larger sizes in larger samples (it may also explain the shift of the curves in Fig.5.1).

In Fig.5.1 and Fig.5.2, the $\sigma(s^w) - N$ curves show how larger samples narrow the distribution of s^w on different samples. The peaks of $\sigma(s^w)$ correspond to the major evolution of s^w , when small changes of \bar{p}^c lead to the recursive invasion of many pores. This dispersion is much smaller in open-side mode. The decreasing trend of $\sigma(s^w)$ and N in open-side mode is illustrated for selected values of saturation, $s^w = 0.4$ and $s^w = 0.2$. The $\sigma(s^w) - \sqrt[3]{N}$ curves are reported on Log-Log axes in Fig.5.3. $\sqrt[3]{N}$ can be interpreted as the edge length of a cubic domain containing N spheres. In the figure, fitting equations following conventional variance reduction are superimposed. They agree with the data in a satisfying manner for the larger sizes.

$$\sigma(s^w) = \frac{0.6}{\sqrt{N}} \quad (5.1)$$

when $\bar{s}^w = 0.2$; and

$$\sigma(s^w) = \frac{2.4}{\sqrt{N}} \quad (5.2)$$

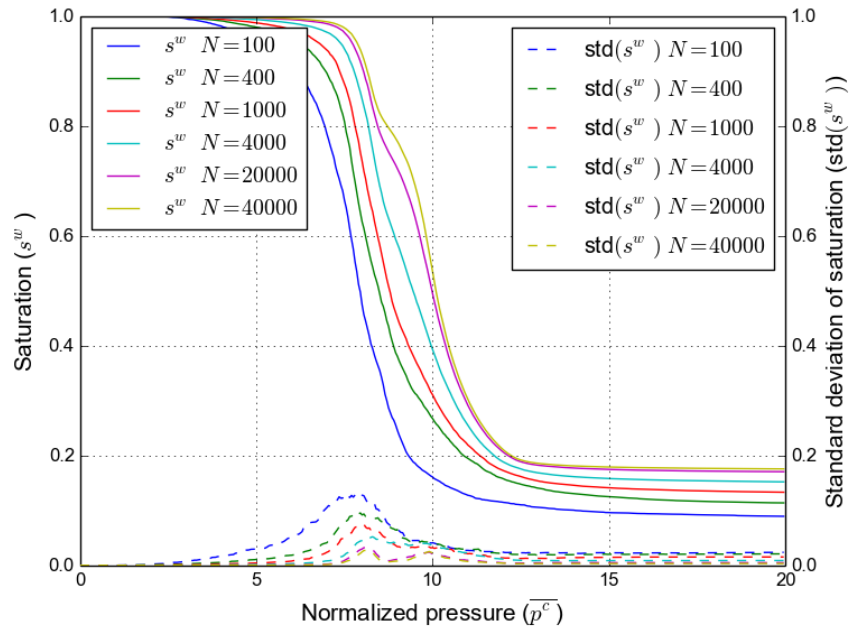


Figure 5.1: Average $\overline{p^c} - s^w$ curve as a function of sample size in open-side mode (100 repeated simulations for each case). See colour version of this figure online.

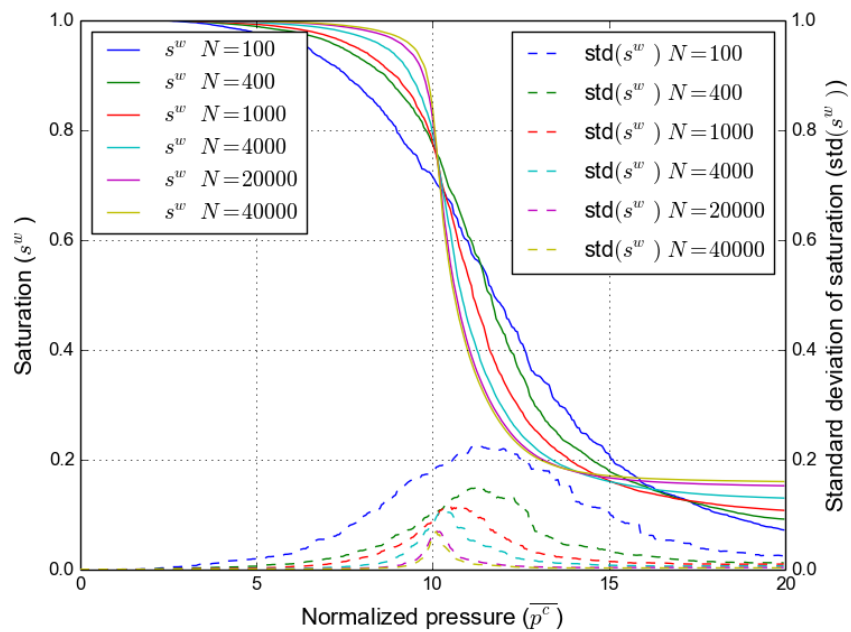


Figure 5.2: Average $\overline{p^c} - s^w$ curve as a function of sample size in closed-side mode (100 repeated simulations for each case). See colour version of this figure online.

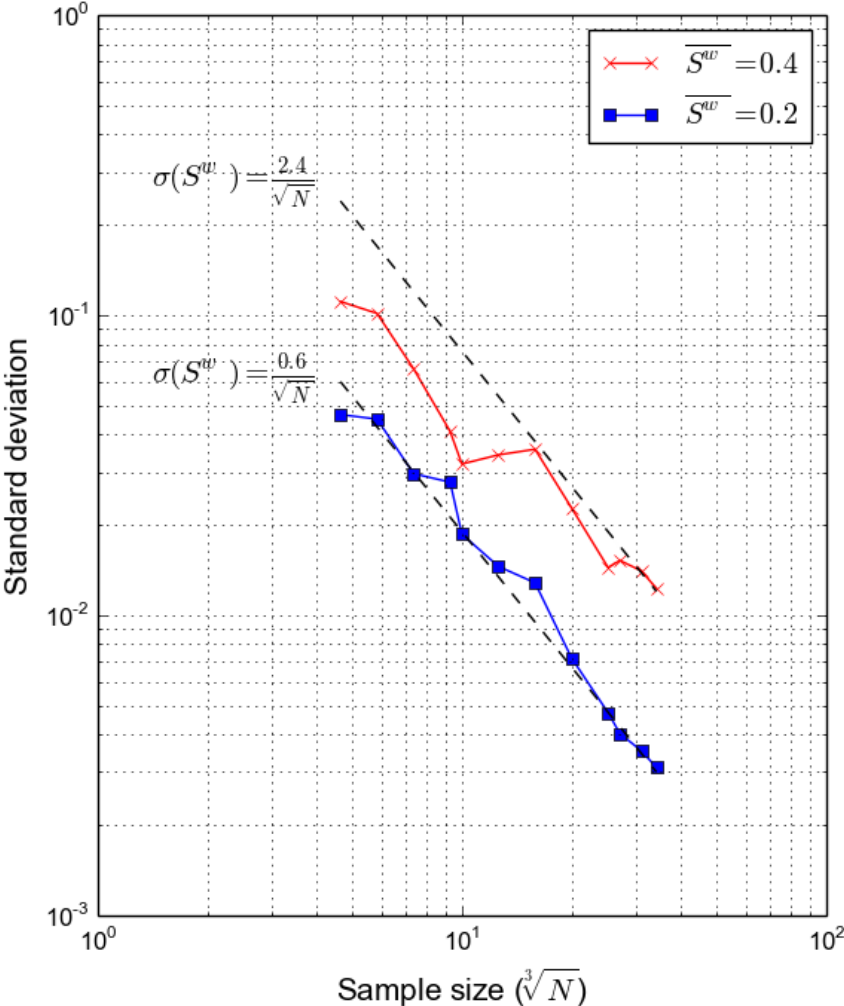


Figure 5.3: The relationship between standard deviation of saturation and packing size (in open-side drainage mode).

when $\overline{s^w} = 0.4$.

Regardless of the drainage mode at the boundaries, it can be concluded that the average s^w is significantly biased for $N < 20,000$, and the bias is significantly larger than the standard deviation. For instance, the standard deviation of residual saturation for $N = 100$ is of the order of 0.02 (0.13 when $s^w = 0.4$) while the difference with $N = 40000$ in terms of the average residual saturation is about 0.1 (0.34 for the value of $\overline{p^c}$ corresponding to $s^w = 0.4$ in the large sample). The difference in s^w between $N = 20,000$ and $N = 40,000$ is 0.002 at residual saturation, and 0.02 near $s^w = 0.4$. Open-side conditions seem to give more robust measurements. They preserve the general shape of the $\overline{p^c} - s^w$ curves for every N and the standard deviation is decreased. Interestingly, it suggests that the simulations compared well with the experiments (previous section) only because they were both biased in the same way ($N \approx 400$ spheres in both cases), while simulating larger samples would have led to a worse agreement.

5.3 Subsampling

In order to examine the sub-sampling problem, we used a large sample of 64,000 spheres in which we defined a set of points (64 vertices of a cubic $4 \times 4 \times 4$ array) to be the centers of subdomains. The porosity and saturation per subdomain are analyzed for different sizes of the subdomains. The PSD and average porosity are the same as in previous sections. Like before the subdomain size is defined by $\sqrt[3]{N}$ where N is the number of sphere per subdomain (in average). Based on the conclusion of previous section, we examine only the open-side drainage mode.

The average quantities obtained in each subdomain are plotted as functions of $\sqrt[3]{N}$ and superimposed in Fig.5.4 and Fig.5.5. As expected, the porosity of every subdomain converges steadily to the global porosity of the sample as N increases. The evolution of the s_{sub}^w values is more erratic. It shows strong oscillations for the smaller sizes, much more scattering than porosity, and some subdomains hardly converge to a general trend even for 10^3 spheres. Obviously this can be explained by large single-phase clusters.

Fig.5.6 reports the evolution of $\sigma(\phi_{sub})$ and $\sigma(s_{sub}^w)$ as functions of $\sqrt[3]{N}$. The fact that $\sigma(\phi_{sub}) < \sigma(s_{sub}^w)$ implies that the minimal REV size for saturation is clearly much larger than what could be used for estimating porosity. A conclusion also reached by Hilpert and Miller (2001), in which standard deviations of similar magnitude are reported. Fig.5.6 also shows trend lines of the form α/\sqrt{N} , where α is adjusted for each series of points. The $\sigma(s_{sub}^w) - \sqrt[3]{N}$ is very well described by

$$\sigma(\phi_{sub}) = \frac{0.065}{\sqrt{N}}. \quad (5.3)$$

The evolution of $\sigma(s_{sub}^w)$ does not follow such a simple form. Trying to adjust α using the data from the largest samples (fig.5.6) suggests

$$\sigma(s_{sub}^w) = \frac{2.3}{\sqrt{N}} \quad (5.4)$$

for $\overline{s_{sub}^w} = 0.4$, and

$$\sigma(s_{sub}^w) = \frac{0.68}{\sqrt{N}} \quad (5.5)$$

when $\overline{s_{sub}^w} = 0.2$. The expressions are very close to the ones found in previous section.

The large differences between those standard deviations are easily explained. At higher saturation ($\overline{s_{sub}^w} = 0.4$), capillary fingerings results in large single-phase patches (see Fig.5.7). Hence the average saturation computed in a particular subdomain is strongly influenced by the position of its center. If the subdomain is too small, it may even be entirely occupied by one of the phases cluster. The condition that the sampled volume must be larger than the heterogeneities is never satisfied, which leads to the poor agreement with the $1/\sqrt{N}$ trend. This does not happen for porosity, since every solid particle is surrounded by a certain amount of pore space (especially for spherical shapes).

At lower saturation ($\overline{s_{sub}^w} = 0.2$) the receding W-phase is present mainly in the form of disconnected patches (Fig.5.8). These patches are larger than a particle diameter but smaller than the patches observed at $\overline{s_{sub}^w} = 0.4$. The standard deviation is clearly reduced and the $1/\sqrt{N}$ trend is nearly acceptable for the largest samples. The α -values which appear in the fitting equations (0.065 for $\sigma(\phi_{sub})$ versus 0.68 for $\sigma(s_{sub}^w)$ for $\overline{s_{sub}^w} = 0.2$) suggest that the heterogeneities of the phase distribution have a characteristic volume one hundred times larger than the heterogeneities of the void space. A result consistent with the image of Fig.5.8 where we may accept 5 particle diameters ($5^3 \simeq 100$) to reflect the typical distance separating the disconnected patches. The poor fit obtained with $1/\sqrt{N}$ evolution suggests that even the largest subsample (1000 spheres) is far below an acceptable REV size when $\overline{s_{sub}^w} > 0.4$. We did not proceed to larger sizes since the subdomains would overlap each other or reach the boundaries. The strong size dependency of saturation near the percolation threshold (the value of $\overline{p^c}$ for which the NW-phase reaches the W-reservoir) is actually a known issue: the size of the largest patch tend to increase as the sample size is increased (de Gennes and Guyon, 1978; Lenormand and Bories, 1980; Wilkinson and Willemsen, 1983), hence the REV question in itself is ill-posed. This is a rather challenging problem for defining macroscale properties. We shall not enter this debate here as it would need more investigation (possibly using our model). The reader may refer to Hilpert and Miller (2001) for a fractal approach of the problem. Here we retain that the standard deviation seems to reach a normal trend at least at low saturation.

5.4 Boundary conditions and aspect ratio

In this section, we analyze the effects of the side boundary conditions and the sample shape. Since circular columns are out of reach of our current algorithm we only discuss the shape effect in terms of the aspect ratio of rectangular boxes. The samples are made of 40000 spheres with the same porosity and PSD as before. They are prepared with different ratio of cross-sectional side-length L over height H ($H/L = 0.5, 1.0$ and 5.0).

A sub-sampling is done by dividing the column in 10 layers perpendicular to the drainage direction. These layers are indexed from ID-1 (connected to W-phase reservoir) to ID-10 (connected to NW-phase reservoir), as shown in Fig.5.9. Since the random positioning of spheres can influence the results, as illustrated in section 4.2.3 (see Fig.4.9), we report results averaged in each layer for different samples. In order to describe the invasion of the NW-phase, we define the NW-phase penetration depth D^p as the maximum vertical distance between the NW-reservoir and the NW-W interface. This penetration

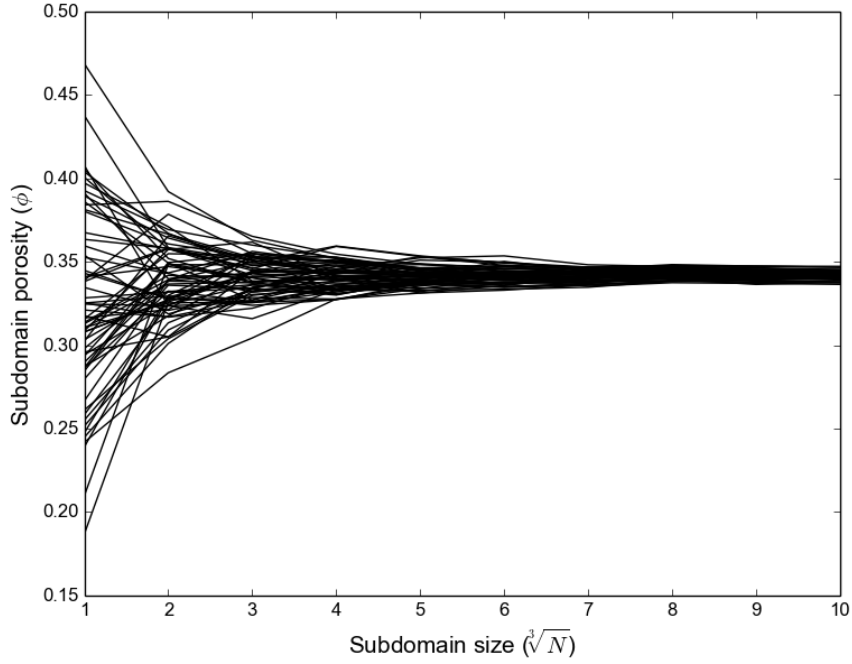


Figure 5.4: Micro-porosity versus averaging subdomain size. $\overline{\phi_{sub}} = 0.34$

depth is normalized as

$$D^* = \frac{D^p}{H} \quad (5.6)$$

in which H is the height of specimen. Both open-side and closed-side drainage modes are simulated. The $\overline{p^c}$ and s^w values are recorded for the entire packing and per layer.

5.4.1 Effect of side boundary connectivity

In open-side drainage, the NW-phase can invade all pores, including the pores in contact with the side boundaries of the container. In closed-side conditions, the invasion is only allowed in the inner part of the sample. Examining early stages of the open side drainage reveals a preferential invasion starting along the boundaries (Fig.5.10(a)). This tendency has been also observed in experiments on glass beads (Khaddour et al., 2013), as shown in Fig.5.10(b). Simply, the throats formed by two spheres in contact with a flat surfaces tend to be larger than the throats found in the rest of the microstructure (*i.e.*, between 3 spheres). It is consistent with previous findings on anomalous porosity due to wall effects (Marketos and Bolton, 2010) and it leads to lower values of p_e^c along the boundaries, hence preferential invasion. In a second step the invading phase percolate to the inner part starting from all boundaries of the samples (W-reservoir excepted).

It is worth noting that this drainage sequence may not be generalized to every granular material since the experiments in Khaddour et al. (2013) did not show the same evolution with grains of irregular shapes (Fig.5.10(c), Hostun sand). Angular or elongated grains thus seem less prone to form large throats near the walls of the container.

The effect of side boundary conditions can be further investigated by comparing the invasions under different assumptions. At the beginning of invasion, the layer saturation

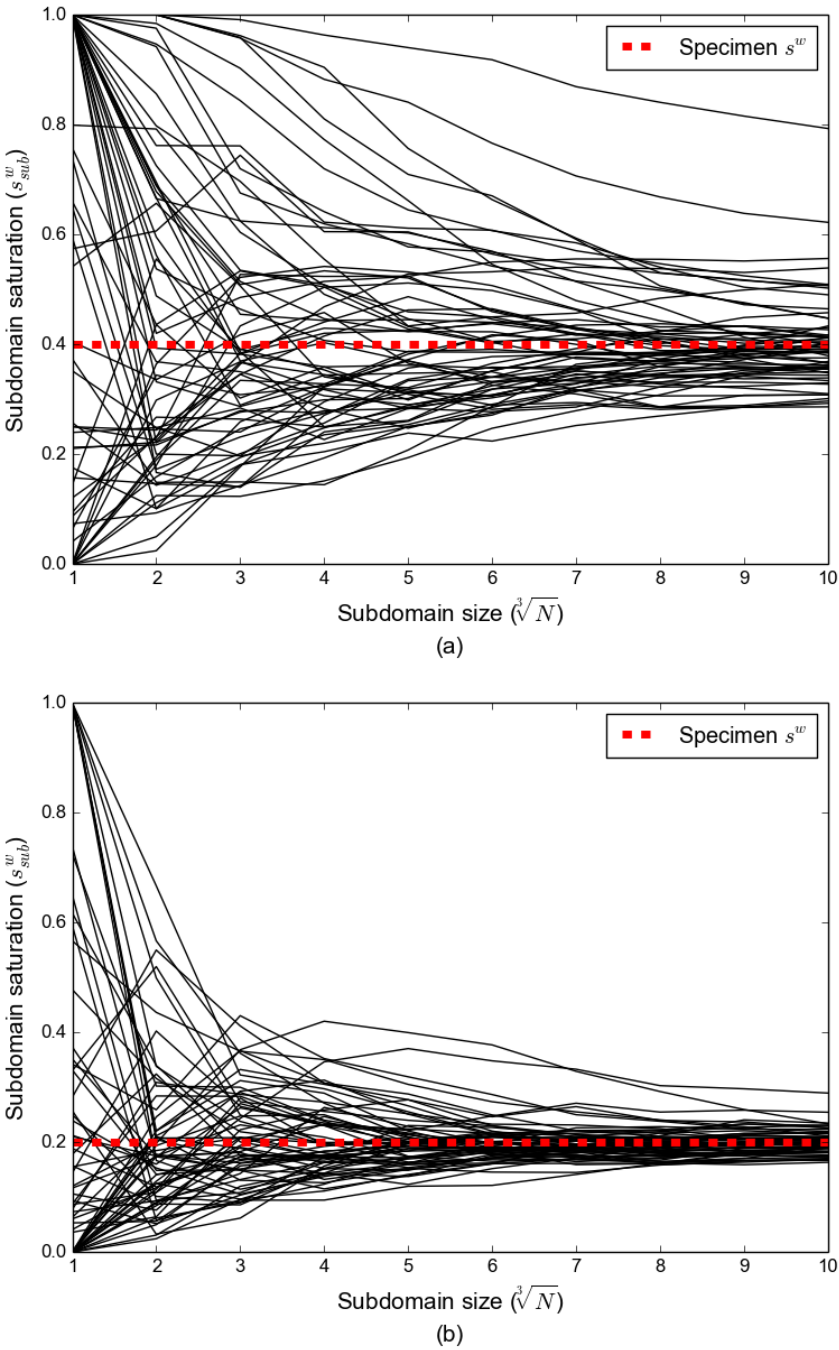


Figure 5.5: Micro-saturation versus averaging subdomain size. (a): $\overline{s_{sub}^w} = 0.4$, (b): $\overline{s_{sub}^w} = 0.2$.

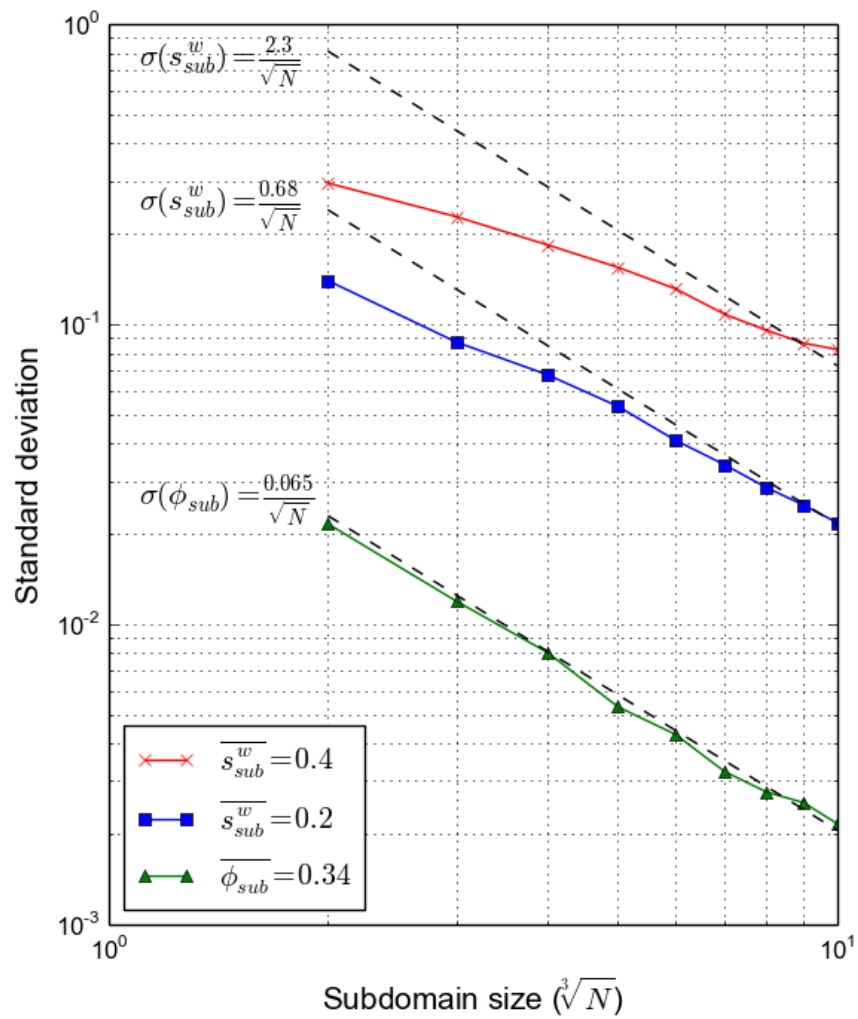


Figure 5.6: Statistics of saturation and porosity versus size of the averaging subdomain.

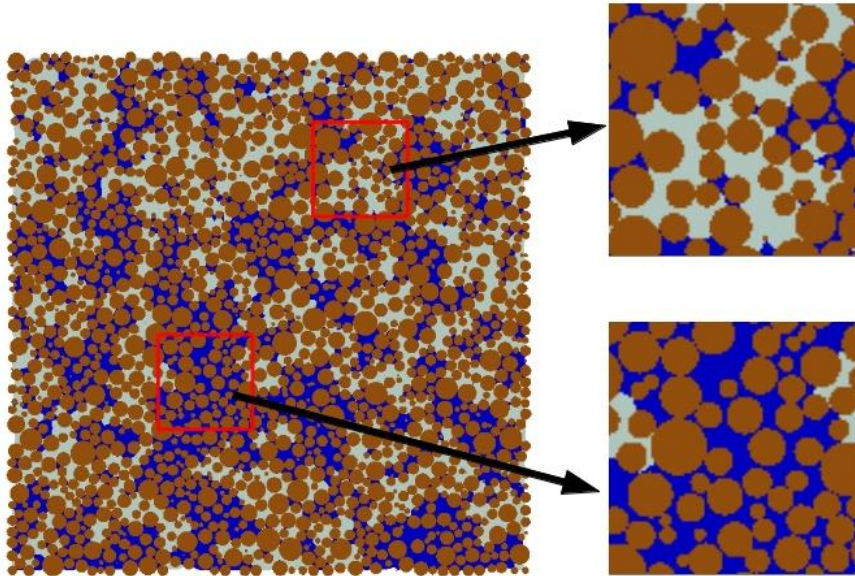


Figure 5.7: Right: a slice through a sample at $s_{sub}^w = 0.4$ (the top boundary is connected to the NW reservoir), in which strong capillary fingering can be observed. Left: zoom on two subdomains used in the averaging procedure.

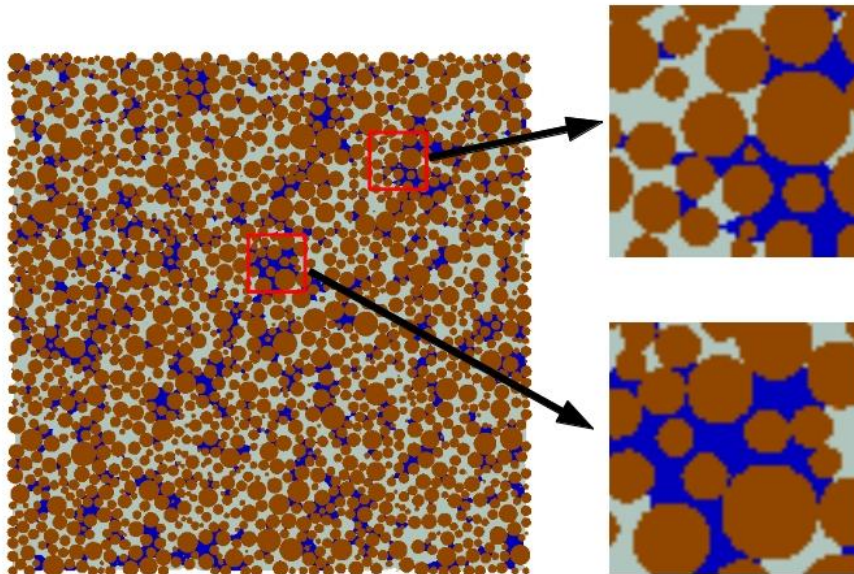


Figure 5.8: Right: a slice through a sample at $s_{sub}^w = 0.2$ (the top boundary is connected to the NW reservoir), in which patches of trapped W-phase are visible. Left: zoom on two subdomains used in the averaging procedure.

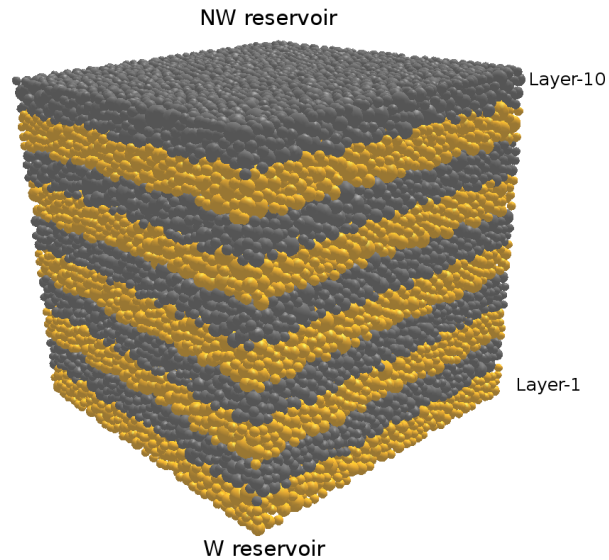


Figure 5.9: Numerical setup and indexed layers. The bottom of Layer-01 is connected to the W-phase reservoir, the top of Layer-10 is connected to the NW-phase reservoir.

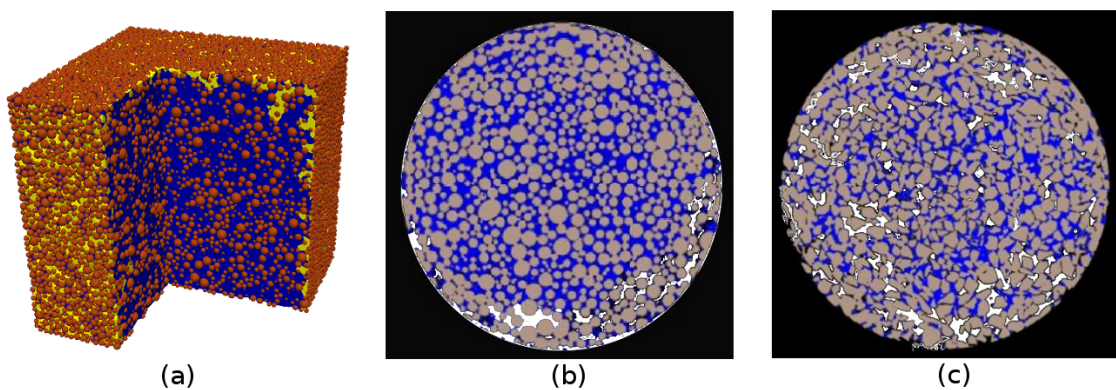


Figure 5.10: Comparison of invasion between a simulation in open-side drainage and the experiments of Khaddour et al. (2013). (a) Simulation (dark blue: W-phase, yellow: NW-phase). (b) experiment on glass beads. (c) experiment on Hostun sand (gray: glass beads/sand, dark blue: water, white: air).

is very heterogeneous, with low saturation near the NW reservoir and high saturation near the W reservoir. This phenomenon can be observed in both drainage modes as shown in Fig.5.11 ($\bar{p}^c = 8.0$) and Fig.5.12 ($\bar{p}^c = 9.0$), where saturation decreases almost only in the top layer. This effect is less pronounced in open-side mode. By comparing the distribution of s^w for the same aspect ratio of specimens, *i.e.*, Fig.5.11(a) vs Fig.5.12(a), Fig.5.11(b) vs Fig.5.12(b), and Fig.5.11(c) vs Fig.5.12(c), it is found that the W-phase retention is much more homogeneous if the side boundaries can be invaded, as could be expected from the aforementioned two-step sequence of invasion. In closed-side mode, the NW-phase can only invade layer by layer, leading to a stronger saturation gradient in intermediate steps. Finally, the residual saturation is approximately homogeneously distributed in all layers.

The evolution of saturation and penetration with capillary pressure are shown in Fig.5.13 and Fig.5.14. It is found that the NW-phase invasion in open-side mode starts at lower values of \bar{p}^c , this is due to large pores along the boundaries. The evolution of D^* confirms the two-step sequence in open-side drainage: the main evolution of saturation happens after NW-phase percolation through the entire sample, *i.e.*, after $D^* = 1.0$. With closed-side drainage the main evolution of s^w is accompanied by the increase of D^* . Again, the results are less scattered when the side boundaries can be invaded.

5.4.2 Effect of aspect ratio

In Fig.5.13 or Fig.5.14, for a given \bar{p}^c , the NW-phase invade more deeply for smaller H/L ratio. This is consistent with the W-phase profiles of Fig.5.11 and Fig.5.12, which show a lower saturation for smaller aspect ratio. This applies equally well to residual saturation, which suggests more W-phase trapping for larger H/L .

This effect is less significant in open-side drainage for the layers 3-7 (Fig.5.11). In this case most of the difference in sample saturation comes from those layers within a short distance from the reservoirs. A large H/L tends to reduce the fraction of the total volume which is exposed to this near-reservoir situation, hence for $H/L = 5$ even layers 1 and 10 only slightly deviate from the global average.

In closed-side drainage, on the other hand, a smaller H/L tends to produce slightly more homogeneous phase distribution - even though it remains rather heterogeneous for $0.4 < S_r < 1$ (Fig.5.12). This evolution is dominated by a main percolation event, corresponding to large gradients of saturation. After the first percolation (*i.e.*, as soon as $D^* = 1$) a progressive homogenization of the phases distribution occurs until residual saturation is reached. As percolation occurs a bit earlier at low H/L , the homogenization phase starts earlier too. In any case, closed-side boundary conditions do not provide a robust base for evaluating the $\bar{p}^c - s^w$ relation for $s^w > 0.4$ in primary drainage, given the large heterogeneity of the phase distribution.

Conclusions

The goal of this chapter was to assess size effects and boundary effects on primary drainage when testing small samples - a key question when designing small scale experiments and simulations. We examined separately the statistics from samples of different sizes, then those from subsamples of a single large sample. The main conclusions are:

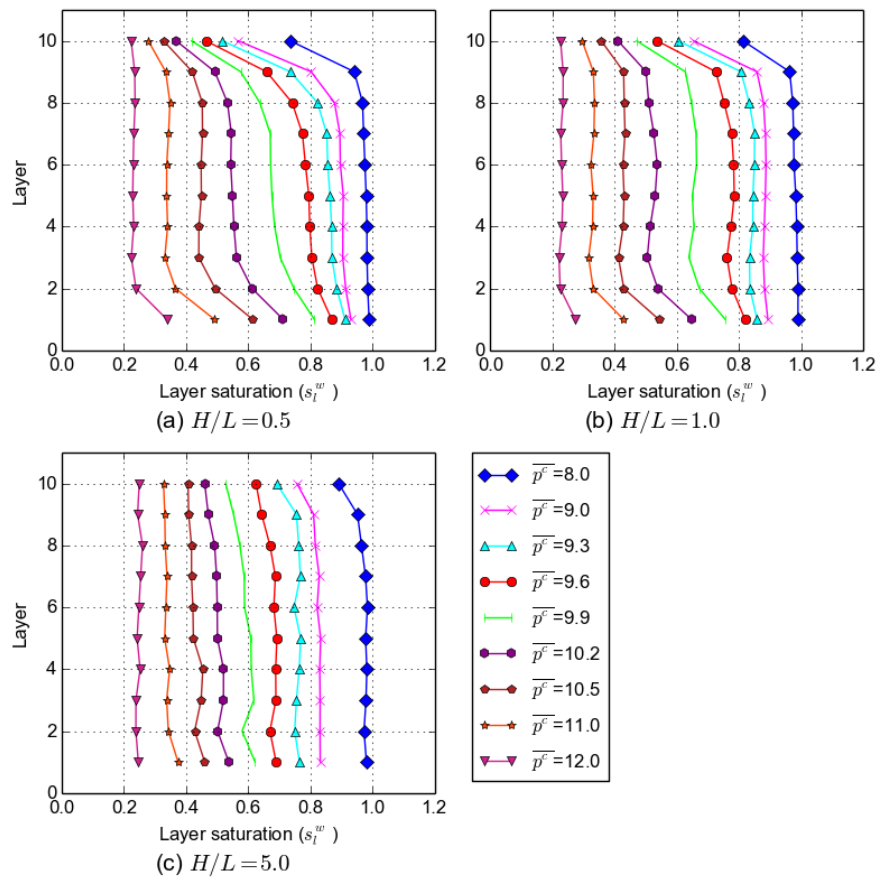


Figure 5.11: Saturation distribution of different layers under certain capillary pressures in open-side drainage.

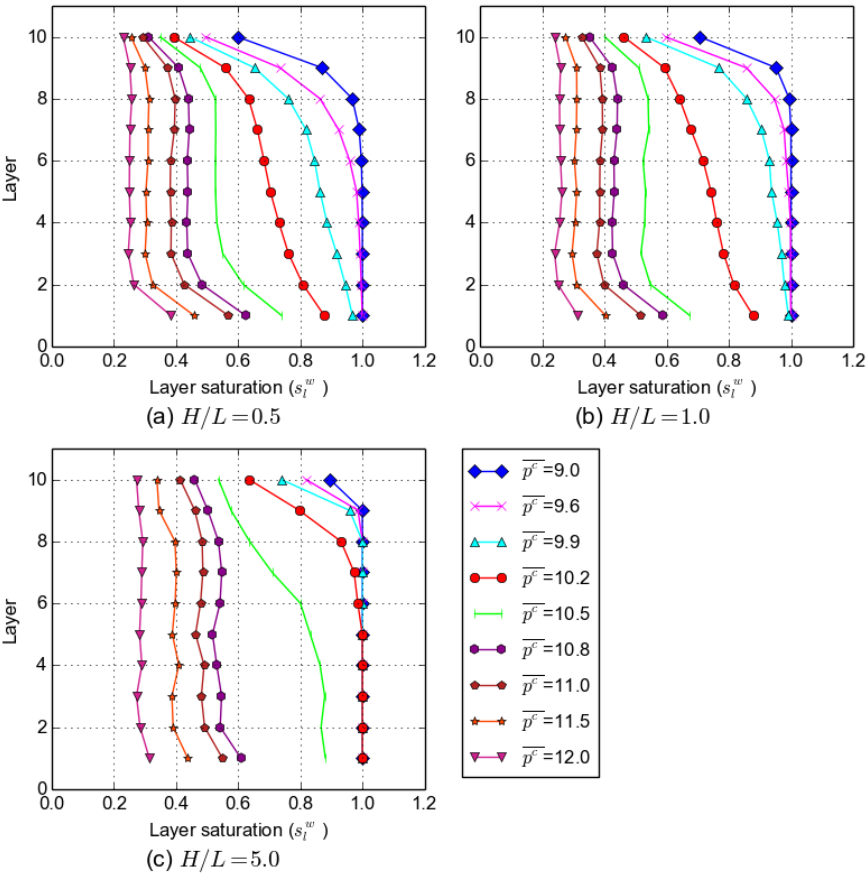


Figure 5.12: Saturation distribution of different layers under certain capillary pressures in closed-side drainage.

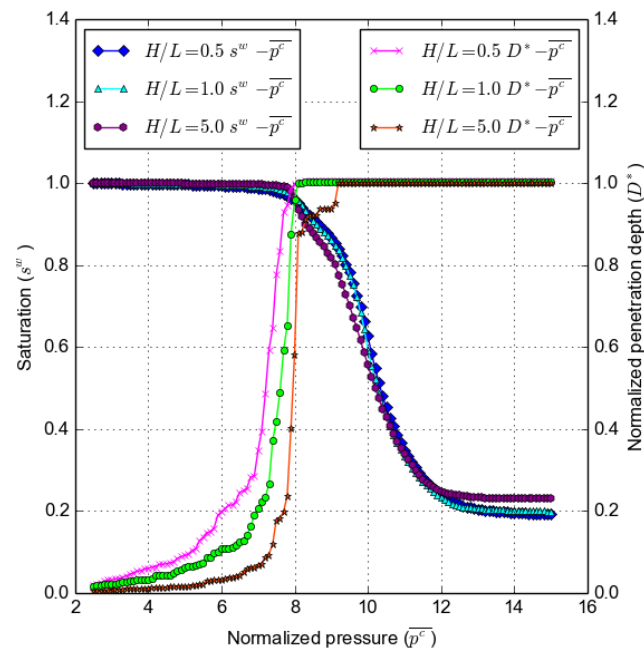


Figure 5.13: Comparison between different aspect ratios of simulations for $s^w - \bar{p}^c$ curves and $D^* - \bar{p}^c$ curves in open-side drainage

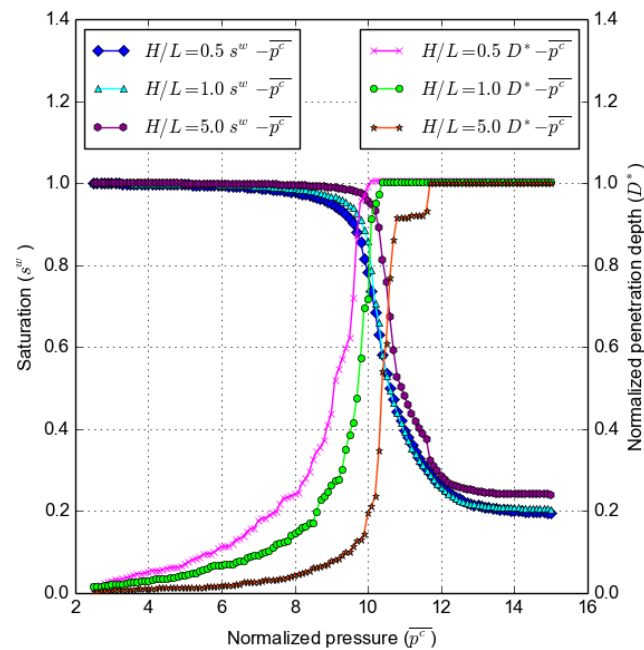


Figure 5.14: Comparison between different aspect ratios of simulations for $s^w - \bar{p}^c$ curves and $D^* - \bar{p}^c$ curves in closed-side drainage

- The standard deviation of s^w in repeated simulations of primary drainage roughly follow a simple variance reduction law with increasing sample size, *i.e.*, $\sigma(s^w) \simeq 2.4/\sqrt{N}$ for the maximum deviation (when s^w is close to 0.4) and $\sigma(s^w) \simeq 0.6/\sqrt{N}$ at residual saturation. The orders of magnitude of $\sigma(s^w)$ are in agreement with Hilpert and Miller (2001) in which 2500 was suggested as a sufficient number of spheres, corresponding to a maximum deviation of $\sigma(s^w) = 0.048$ with our expression.
- Standard deviation should not be the unique criterion for evaluating the representativity. Indeed the sample size can be the cause of significant bias in the average result. The saturation decreases with decreasing sample size. For 2500 spheres for instance, the difference may reach 0.3 based on our results (for $s^w \simeq 0.4$), *i.e.*, much more than the standard deviation found for this particular size. We found that at least 20000 spheres must be used in order to reduce the bias below 0.02.
- Boundary conditions also affect the result significantly. The paradox is that the strong boundary effects observed when preferential invasion occurs along the boundaries lead to more robust evaluations of the $\overline{p^c} - s^w$ relation overall. When this phenomenon is not present the shape of the $\overline{p^c} - s^w$ curve is more sensitive to sample size and the phase distribution always show strong gradients of saturation. A similar problem would most likely appear with periodic boundary conditions.

The need to compute large samples clearly shows the need for efficient numerical techniques such as the pore-network methods. It justifies *a posteriori* our attempt to develop a fast pore-scale method for coupled hydromechanical problems.

We suggest a few guidelines for further attempts to compare simulations and small scale experiments:

- The comparisons should be done on samples of similar sizes, ideally similar shapes, and with the same boundary conditions. Even below the REV size, this can lead to relevant model validations provided that the inherent variability is kept in mind.
- The experiments should be designed and reported in such a way that the boundary conditions can be accurately reproduced in a model. Scanning a small window in a long column is detrimental for this reason.
- Ideally, the position and size of each grain should be provided to eliminate the main source of variability, this is within reach of recent techniques (Andò et al., 2012).

The above conclusions apply to well controlled small-sized specimen of granular material with statistically homogeneous distribution of porosity. The extrapolation to conventional lab or field experiments should be done with care. Preferential boundary invasion may occur in some real tests but it could be a peculiar feature of spherical (or well-rounded) grains only. If this boundary invasion is not present, then the lab tests may be more similar to our closed-boundary case, which suggest the occurrence of strong gradients of saturation in the samples. It raises difficult questions on the interpretation of lab tests: is an average s^w relevant when strong gradients of s^w are present? More generally, our results underline a known feature: the key role of heterogeneities (in our case the boundaries) in the drainage process. Every heterogeneity of a soil sample (be it intrinsic

or due to a particular sampling technique) may strongly influence its water retention properties. Likewise, heterogeneities at the field scale (soil composition, roots, wormholes,...) may play a dominant role in the transfers.

Chapter 6

Bishop's effective stress parameter

As reviewed in section 2.2, the debate on the most appropriate stress frame work for unsaturated soils has lasted for several decades. Several forms of adequate stress variables, either in single-variable form or independent variables form, are still possible. The expression of Bishop's effective stress parameter χ also have been established in various forms, for instance, Eq.2.4-2.6. The uniqueness of relationship between χ and saturation s^w has often been questioned. Most of these expressions are based on the results of experimental tests, in which both the test sample and the measured variables are at macro-scale. The effects of heterogeneity might be concealed. Besides, the deformation induced by loading/unloading or drying/wetting is often in elastoplastic regime, which introduces more uncertainties.

In this chapter, we will examine χ from the simplest case using the 2PFV-DEM model. A drainage test will be performed under the oedometer test conditions, in which only one-dimensional elastic deformation will be generated. χ will be derived and analyzed from macro and micro viewpoints. The relationship between χ and s^w will be analyzed in detail.

6.1 Simulation setup

The simulation follows the setup of model test in section 4.2, i.e., the drainage is performed under the oedometer test conditions, in which only one-dimensional deformation of the solid skeleton is allowed. However, based on the conclusions of previous chapter, the size of sample for testing in this chapter is relative larger than previous ones, in which we consider the cubic packing contains 40,000 particles. (In section 4.2, the test aims to show the basic functions of the model, thus the sample only contains < 1000 particles for efficiency.) The initial porosity of the sample is 0.34. The particle size distribution (PSD) follows Tab.4.1. The top and bottom of the sample connect to the NW-reservoir and W-reservoir, respectively. The sample is initially saturated, assuming $p^c = p^n - p^w = 0$. Drainage is controlled by decreasing p^w and keeping p^n constant. We assume the W-phase can be trapped by the NW-phase, i.e., "with-trap" drainage is performed.

6.2 Recall $\overline{p^c} - s^w - \varepsilon_{11}$ relationship

Let us recall the hydraulic and mechanical response as reported in section 4.2. Similarly, we obtain the results for the large packings. We superpose them in one figure, where the evolution of normalized capillary pressure-saturation-one dimensional strain ($\overline{p^c} - s^w - \varepsilon_{11}$) is reported, as shown in Fig.6.1.

A water retention curve has been achieved by the model, in which $\overline{p^c}$ is controlled to increase gradually. The saturation s^w shows discontinuous reduction, because the distribution of p_e^c is heterogeneous. The sharp decrease of s^w during $9.5 < \overline{p^c} < 11.5$ can be considered as the consequence of ‘‘Haines jumps’’.

From the evolution of ε_{11} , we can observe that the sample first shrinks and then swells. In the beginning, before the first entry of NW-phase (i.e., $\overline{p^c} < 8.0$), the $\varepsilon_{11} - p^c$ relationship is linear. It can be explained by Terzaghi's effective stress principle for saturated conditions (i.e., Eq.2.2). The decrease of p^w leads to the increase of σ'_{ij} . Then the sample keeps shrinking until reaching the peak during $8.0 < \overline{p^c} < 9.8$. In this stage, the porous media is still highly saturated, and most of the solid particles are immersed in the W-phase. Thus, the deformation is still mainly dominated by the σ' of saturated macroscopic scenario. However, the relationship of $\overline{p^c} - \varepsilon_{11}$ is not linear any more.

In the third stage ($9.8 < \overline{p^c} < 14.2$), with the W-phase receding, the solid skeleton becomes dry. We assume p^n is constant, the effective stress for dry scenario is,

$$\sigma'_{ij} = \sigma_{ij}^{net} \quad (6.1)$$

where σ_{ij}^{net} is the ‘‘net’’ stress, $\sigma_{ij}^{net} = \sigma_{ij} - p^n$. It is the same as in the initial state (i.e., when $p^n = p^w$). Thus, the sample is swelling. The nonlinear relationship of $\overline{p^c} - \varepsilon_{11}$ can be explained by the heterogeneous NW-phase invasion (also see Fig.5.7). In the last stage ($\overline{p^c} > 14.2$), clusters of disconnected W-phase are formed because of entrapment. Since we assume there are no flux/pressure exchanges between separated clusters, ε_{11} will be constant. The deformation induced by capillary effects will not be completely eliminated.

6.3 Reproducing the expression of effective stress parameter

Karl Terzaghi introduced the concept of effective stress for the particular case of saturated soil mechanics. Considerable efforts have been made to extend this concept to the unsaturated porous media. Retrospectively, such extension work was pioneered by Bishop (1960) and Bishop and Blight (1963), who extended Eq.2.2 to a general form, Eq.2.3. As a matter of fact, lots of following modified approaches can be consider as the extensions of Eq.2.3.

Experimentally, no unique relationship between χ and s^w can be found for all porous media (Bishop et al., 1960; Bishop and Blight, 1963; Jennings, 1961; Zerhouni, 1991). Also, different deformation regimes (i.e., elastic or elastic-plastic) can lead to different relationships. We will base on Bishop's equation and derive the expression of χ from the macroscopic and microscopic views. Since we only focus on the one dimensional deformation, Eq.2.3 can be simplified by,

$$\sigma'_{11} = (\sigma_{11} - p^n) + \chi(p^n - p^w) = \sigma_{11}^{net} + \chi p^c \quad (6.2)$$

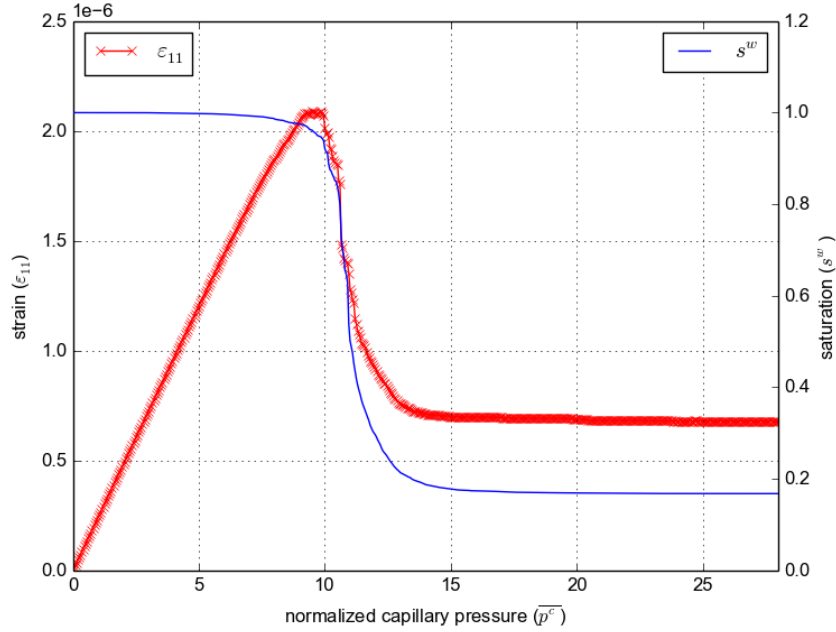


Figure 6.1: The relationship between normalized capillary pressure-saturation-strain ($\bar{p}^c - s^w - \varepsilon_{11}$) during drainage simulation under the oedometer conditions.

6.3.1 Macroscopic view

For Terzaghi, the term “effective” meant the calculated stress that was effective in moving soil, or causing displacement. Following this definition, the effective stress σ' for unsaturated regime can be expressed by the macroscopic deformation, i.e.,

$$\sigma'_{11} = E\varepsilon_{11} \quad (6.3)$$

where E is the elastic modulus. Thus, χ in Eq.6.2 can be expressed by,

$$\chi^M = \frac{E\varepsilon_{11} - \sigma_{11}^{net}}{p^c} \quad (6.4)$$

where χ^M is the macroscopic view of χ .

6.3.2 Microscopic view

The effective stress can also be investigated by microscopic analysis (Catalano et al., 2014; Scholtès et al., 2015). For porous media, the microscopic stress associated to one particle is defined as a sum over the contacts on the basis of particle-centered volumes V_{σ^*} (see Fig.6.2) (Bagi, 1996; Drescher and De Jong, 1972),

$$\sigma^* = \frac{1}{V_{\sigma^*}} \sum_k \mathbf{X}^{c,k} \otimes \mathbf{f}^{c,k} \quad (6.5)$$

where $\mathbf{X}^{c,k}$ is a contact point, $\mathbf{f}^{c,k}$ is the corresponding force and V_{σ^*} is the reference volume associated to the particle in the Voronoi tessellation. Note that σ^* does not reflect

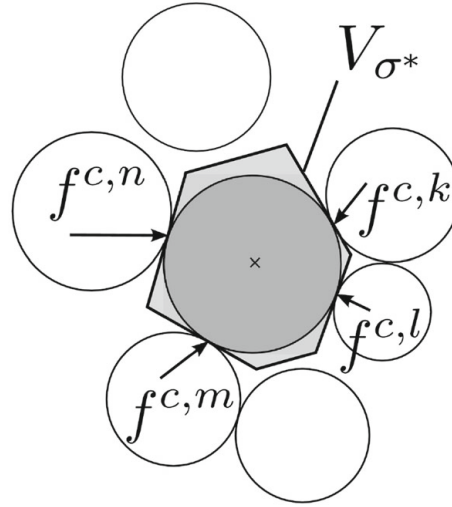


Figure 6.2: Particle-centered domain for the definition of effective stress σ^* at the particles scale

the average stress in this solid particle. To obtain the average stress of one particle, we should divide by the volume of the particle instead of V_{σ^*} in Eq.6.5. In addition, the stress applied by the fluid(s) on the contour(s) and the interfacial tension (if exists) on the contact line should be accounted for. Instead, σ^* reflects the external loading that acts through the contact network. It can be considered as the micro-scale analogy of Terzaghi's effective stress. For saturated scenarios, the equivalence between them has been evaluated in the oedometer test simulation and the results are in good agreement (Catalano et al., 2014). Following this strategy, we also consider σ^* as the micro-scale analogy of Terzaghi's effective stress for unsaturated porous media. Then the stress tensor for entire sample, σ^c , can be calculated by averaging σ^* of all particles. Hence,

$$\sigma'_{11} \approx \sigma^c_{11} \quad (6.6)$$

Finally, another expression of χ can be given from the point view of the contact forces of particles,

$$\chi^m = \frac{\sigma^c_{11} - \sigma^{net}_{11}}{p^c} \quad (6.7)$$

6.3.3 Results

Effective stress parameter

We report the results of χ^M and χ^m and compare them with the original expression $\chi = s^w$ in Fig.6.3. As is shown, the variations of both forms of χ are very similar. (The normalized error $\frac{\chi^M - \chi^m}{\chi^M}$ is less than 1%; for without-trap simulation, the error is less than 10%, see the details in the next chapter Fig.7.14 and Fig.7.16.) We can not explicitly claim that the both expressions are exactly equivalent, but the micromechanical contact forces indeed can be verified as another way for describing the effective stress of unsaturated porous media.

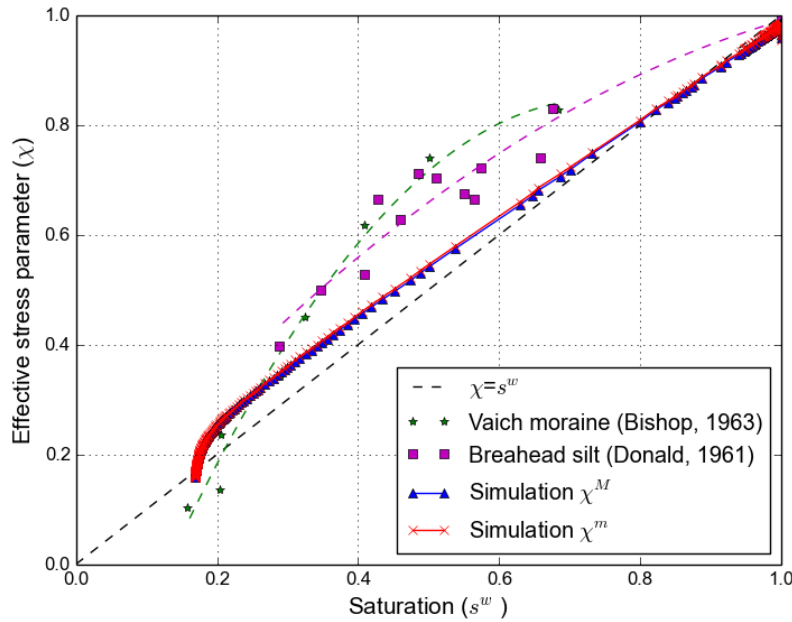


Figure 6.3: Variation of effective stress parameter χ with saturation for simulation results and experimental data. Simulation values are calculated from drainage test of a dense packing (40,000 spheres) under the oedometer test conditions.

The simulated values of χ^M and χ^m lie above the $\chi = s^w$ line. They show a trend of breaking down when the s^w is in a low level. That is because at this stage the W-phase mainly exists in the form of trapped clusters in the pore space. A large amplitude of increase of p^c will not significantly change the deformation of the solid skeleton. Such simulation results are qualitatively similar to the experimental data of Breahhead silt (Donald, 1961) and Vaich moraine (Bishop and Blight, 1963).

Elastic regime confirmation

It is worthwhile to emphasize that the high equivalence of χ^M and χ^m (or, $E\varepsilon_{11}$ and σ_{11}^c) is on basis of a strong assumption. In 2PFV-DEM model, we assume the deformation of solid skeleton is of small amplitude in order to ensure that the assumption of static RT network is valid. This is also the precondition of Eq.6.3. It is necessary to confirm the mechanical evolution is in elastic regime. We plot the evolution of strain and contact stress in Fig.6.4. As is shown, their relationship is linear and reversible.

A similar simulation is performed on a loose packing of sample, in which the sample consists of the same size of particles. The drainage is controlled under the same conditions. We repeat the calculation of χ^M and χ^m following the same method of the previous section. The results are reported in Fig.6.5. As is shown, χ^M and χ^m are clearly not equivalent any more. That is because the deformation of the solid skeleton is not reversible in this case (see Fig.6.6). A constant value of oedometric modulus is not valid, thus Eq.6.3 is violated. Consistently, the result of χ^m can not be objectively evaluated through χ^M .

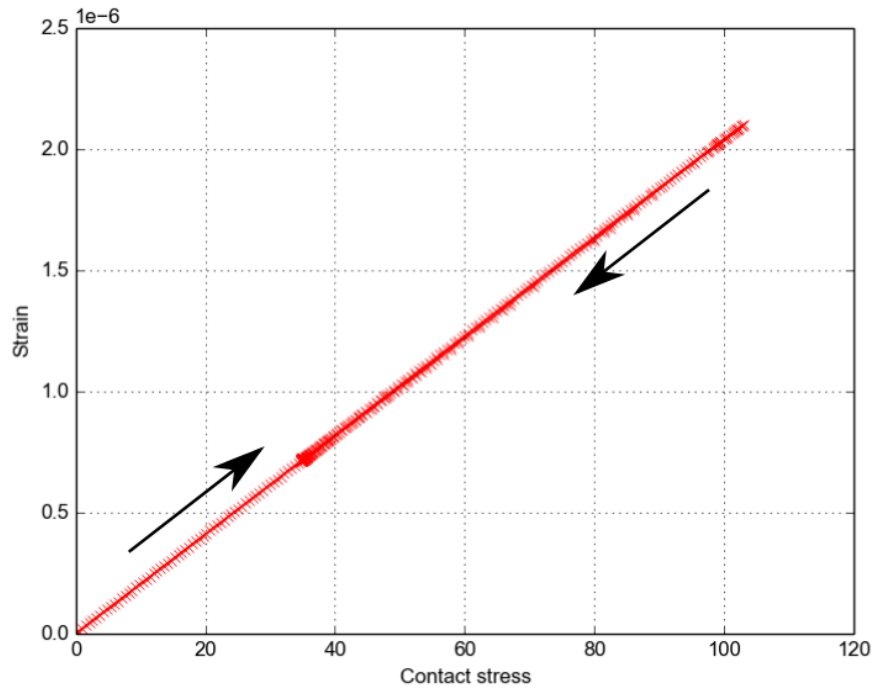


Figure 6.4: A linear and reversible evolution of strain and contact stress during the drainage. The sample first shrinks, then swells.

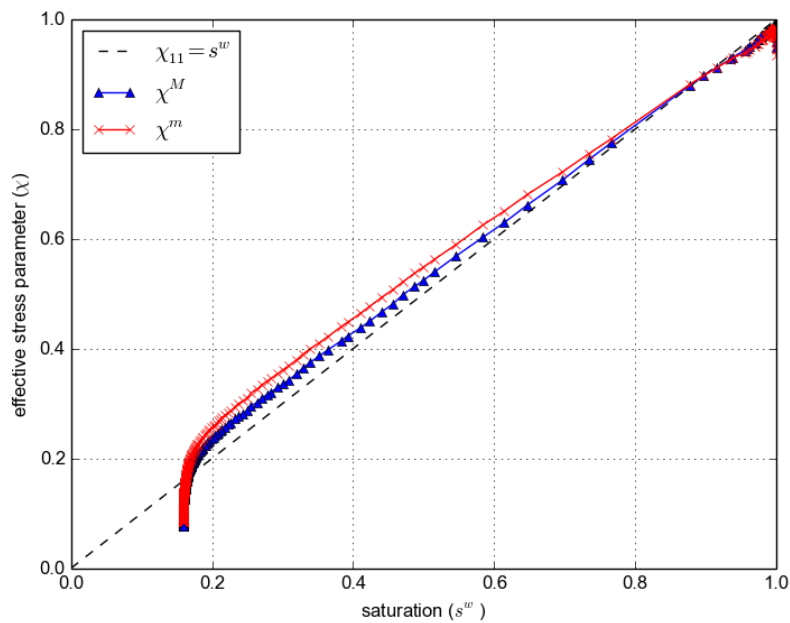


Figure 6.5: Variation of effective stress parameter χ with saturation for simulation results. Simulation values are calculated from drainage test of a loose packing (40,000 spheres) under the oedometer test conditions.

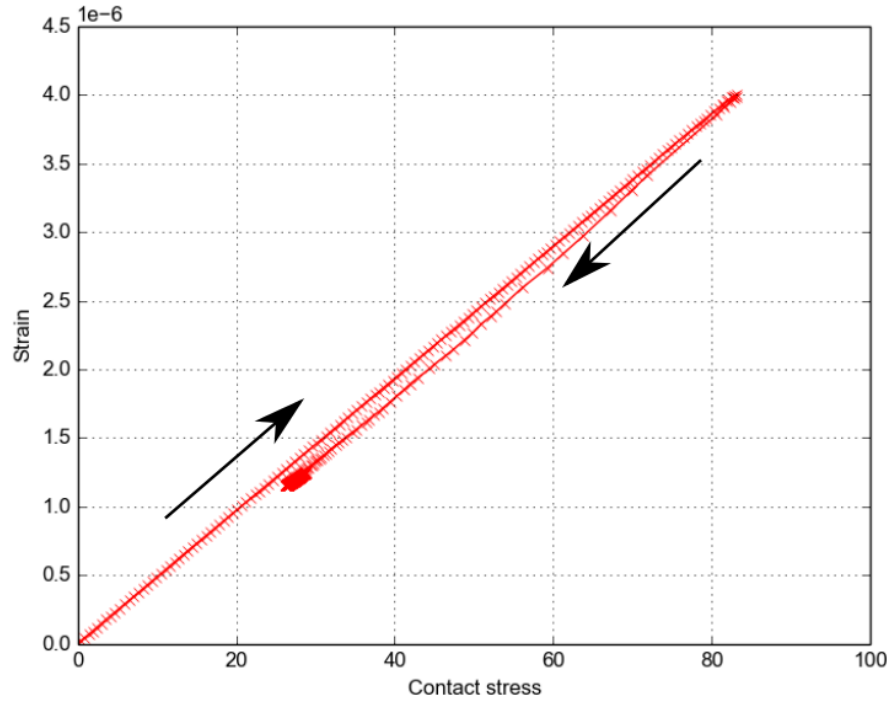


Figure 6.6: An irreversible evolution of strain and contact stress during the drainage. The sample first shrinks, then swells.

6.4 Micromechanical investigation on the effective stress parameter and saturation

In this section, we investigate the relationship between the effective stress parameter and saturation at micro scale, where micro-scale effective stress parameter is denoted as $\underline{\underline{\chi}}$ and micro-scale saturation is denoted as $\underline{\underline{s}}^w$. The results are on basis of elastic deformation of the solid skeleton.

We estimate the effective stress at a certain depth by averaging the stress tensors of solid phase located near this depth with Eq.6.5. Such local stress tensor is denoted by $\underline{\underline{\sigma}}^c$, i.e., $\sigma'_{11} \approx \underline{\underline{\sigma}}^c_{11}$. The micro-scale expression of effective stress parameter can be written as,

$$\underline{\underline{\chi}} = \frac{\underline{\underline{\sigma}}^c_{11} - \sigma_{11}^{net}}{p^c} \quad (6.8)$$

Similarly, the micro saturation $\underline{\underline{s}}^w$ (local saturation at a certain depth) can also be obtained using the average technique.

We report the results of $\underline{\underline{\chi}}$ and $\underline{\underline{s}}^w$ in Fig.6.7. From the evolution of $\underline{\underline{s}}^w$, we can clearly see the propagation of NW-phase invasion. In the beginning, the distribution is very heterogeneous, with low $\underline{\underline{s}}^w$ near the NW reservoir and high $\underline{\underline{s}}^w$ near the W reservoir (see Fig.6.7(a) and (b)). The main evolution of $\underline{\underline{s}}^w$ happens after NW-phase percolation through the entire sample, which leads to the small heterogeneity of the phase distribution. But the localization is still notable (see Fig.6.7(c), also Fig.5.7). This is mainly due to the various geometry of the pore throats, which result in various p_e^c . With the increase of $\overline{p^c}$,

clusters of W-phase are formed. They are disconnected from the W-reservoir and will be accounted as the residual saturation. As shown in Fig.6.7(d), at the end, the distribution of residual saturation is roughly homogeneous, except for the boundary ranges.

If we observe the evolution of $\underline{\underline{\chi}}$, it is quite similar to $\underline{\underline{s}}^w$. In the initial stage, the $\underline{\underline{\chi}}$ of top layer is smaller than the rest parts. Then major evolution appears with a strong localization. Finally, $\underline{\underline{\chi}}$ tends to homogeneous. Such correlation can be explained by the physical interactions of the fluids and solid. $\underline{\underline{\chi}}$ is expressed in term of contact stress, which is affected by the capillary effects (i.e., fluids and interfacial tension) under the equilibrium states. Mathematically, the capillary effects are the consequences of the variations of geometrical items (i.e., W/NW-S contact areas, W-NW-S contact lines) and physical items (i.e., p^w and p^n). The evolution of $\underline{\underline{s}}^w$ leads to such variations. Thus, they change consistently. To conclude, the macro-scale correlation of effective stress parameter and W-phase saturation can be interpreted from the micro-scale perspective.

Since we assume the saturations of the reservoirs are kept constant, the boundary effects can be observed in the top and the bottom domains of the sample, as shown in Fig.6.7c and d. We neglect such effects by filtering out the data of top and bottom domains, then the relationship between $\underline{\underline{\chi}}$ and $\underline{\underline{s}}^w$ can be reported by following the evolution of $\overline{p^c}$, as shown in Fig.6.8. From the results, we can see the similar evolution to Fig.6.3.

It is worthwhile to note that the current expression of $\underline{\underline{\chi}}$ is based on macro-scale p^c , where p^c is the pressure difference between reservoirs. However, the micro-scale capillary pressure is localized as well because of the entrapment of W-phase at different time. If we use $\underline{\underline{p}}^c$ to denote the micro-scale capillary pressure, in order to keep the consistency of the microscopic analysis, Eq.6.8 should be corrected by,

$$\underline{\underline{\chi}} = \frac{\underline{\underline{\sigma}}_{11}^c - \underline{\underline{\sigma}}_{11}^{net}}{\underline{\underline{p}}^c} \quad (6.9)$$

Then we can revise the microscopic evolution of effective stress parameter and saturation as shown in Fig.6.9. From the results, we can observe a unique trend in the evolution of the effective stress parameter as a function of saturation.

Conclusions

This chapter was devoted to investigate the relationship between Bishop's effective stress parameter χ and the saturation of the wetting phase s^w . A primary drainage test has been performed on a large dense sample under oedometer conditions. The results of normalized capillary pressure - saturation - one dimensional deformation ($\overline{p^c} - s^w - \epsilon_{11}$) have been recalled in detail.

From macroscopic view, χ has been derived on basis of the average (macroscale) deformation. From microscopic view, χ has been expressed in terms of the contact stress between solid grains. Their values are quite similar. The strain is consistent with the change of the contact stress. Thus, this feature highlighted by Scholtès et al. (2009a), can be extended to some extent to the intermediate range of saturation, i.e., using the contact stress to calculate the effective stress.

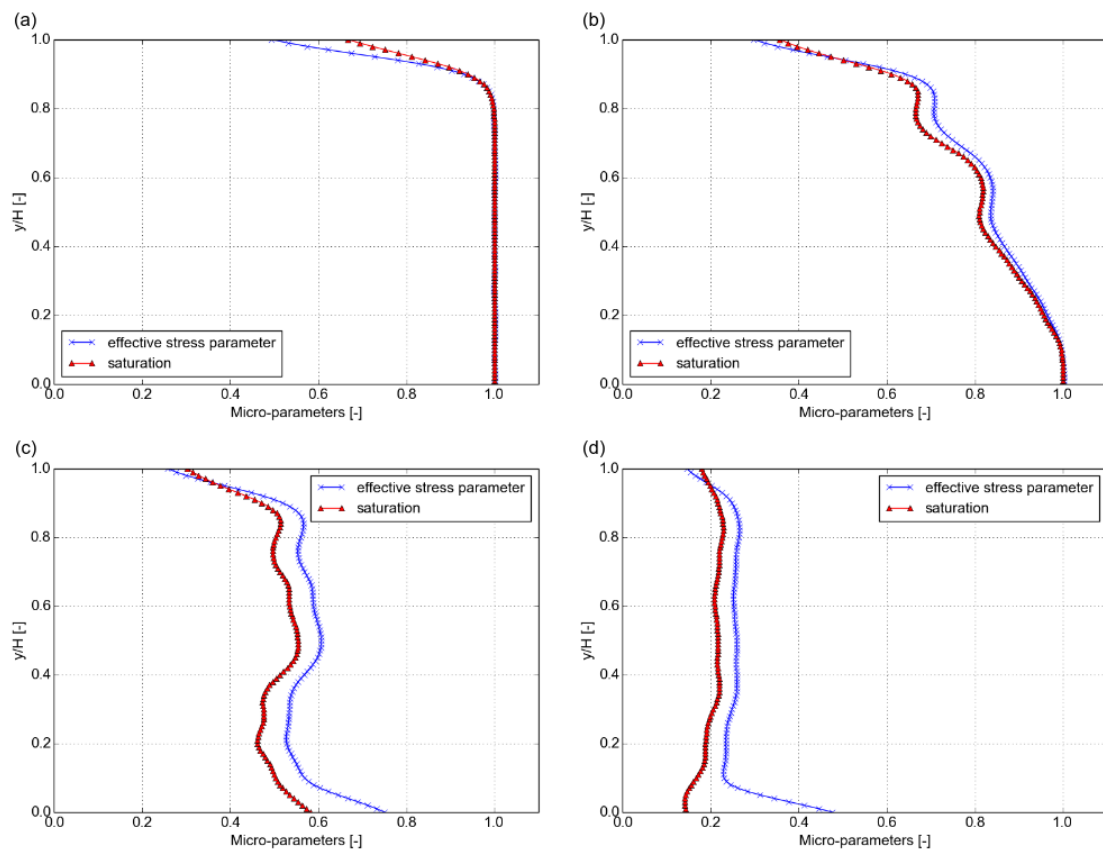


Figure 6.7: Drainage simulation under oedometer test conditions. Evolution of local normalized effective stress and local saturation. (a) $\bar{p}^c = 9.05$; (b) $\bar{p}^c = 11.35$; (c) $\bar{p}^c = 11.90$; (d) $\bar{p}^c = 16.20$.

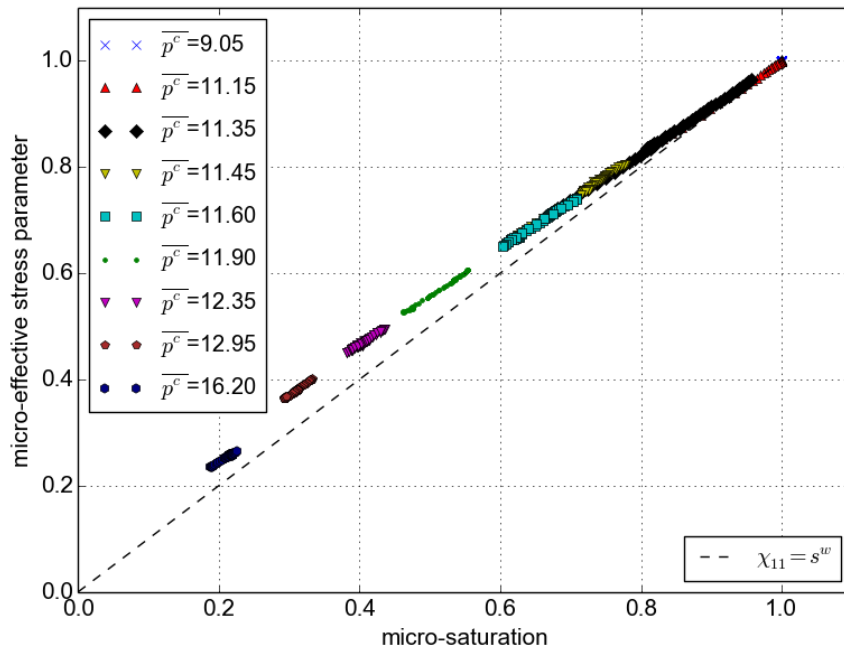


Figure 6.8: The relationship between micro effective stress parameter and micro saturation. Derivation is based on macro p^c , i.e., the pressure difference between reservoirs.

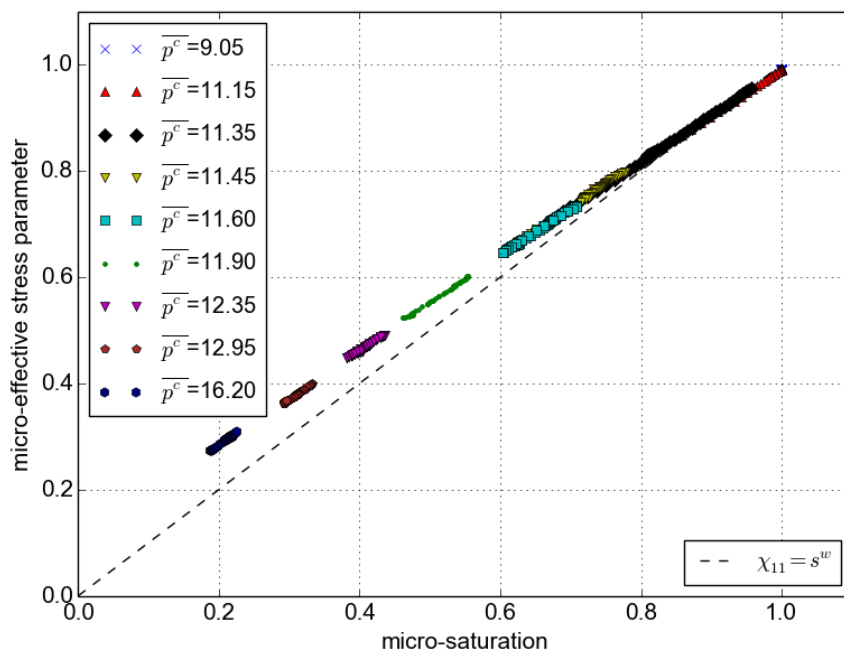


Figure 6.9: The relationship between micro effective stress parameter and micro saturation. Derivation is based on the local capillary pressure.

Further more, the local effective stress parameter and local saturation have been obtained by local averaging. We can observed a unique trend in the evolution of the effective stress parameter as a function of saturation.

Chapter 7

Toward the pendular regime

7.1 Introduction

Let us recall the physics of drainage. In the quasi-static regime, capillary pressure p^c is applied into the porous media to result in the motion of W-NW interface from one equilibrium state to another. The invasion of a local pore depends on the local entry capillary pressure p_e^c , which is to be compared to the present capillary pressure p^c . If $p^c > p_e^c$, the pore is drained and W-NW interface reaches new throats. It possibly triggers a recursive cascade of Haines jumps and more than one pores will be drained, until no more throats satisfy $p^c > p_e^c$. During the invasion events, the W-phase clusters may be disconnected from the W-reservoir by the NW-phase.

- On short timescales, each disconnected cluster is stationary. The value of p^c in the cluster is independent of the imposed p^c . Its volume is fixed.
- On long timescales, the mass transfer between individual clusters through the wetting film or by vapor transport is possible. p^c is uniform.

In previous chapters, we have already presented the “with-trap” and “without-trap” simulations corresponding to the short-term and long-term cases, respectively. Therein, we assumed until now that the saturation of one pore is simply binary, i.e., it equals 0 or 1 depending on which phase is present. The W-phase clusters exist exclusively under the funicular regime.

Practically, after the NW-phase invading a pore, a certain amount of W-phase can be left between solid grains in the form of pendular rings (see the difference in Fig.7.1, from (a) to (b) and from (a) to (c)). The rings follow above rules for the short and long terms, i.e., in short terms (with-trap simulations), each pendular ring is also independent, its volume is constant and p^c is localized; in long terms (without-trap simulations), the rings are connected with each other by the film flow and p^c is uniform. The pendular bridge modeling has been extensively used to simulate the rings by many researchers (Hotta et al., 1974; Ennis et al., 1990; Lian et al., 1993; Li, 2003; Scholtès et al., 2009; Scholtès et al., 2009a), as reviewed in section 1.2.2.

In this chapter, we will extend the 2PFV-DEM model to pendular regime and implement the pendular bridge model based on Scholtès et al. (2009), Scholtès et al. (2009a) and Chalak (2016). The content is organized as follows. We first briefly introduce the

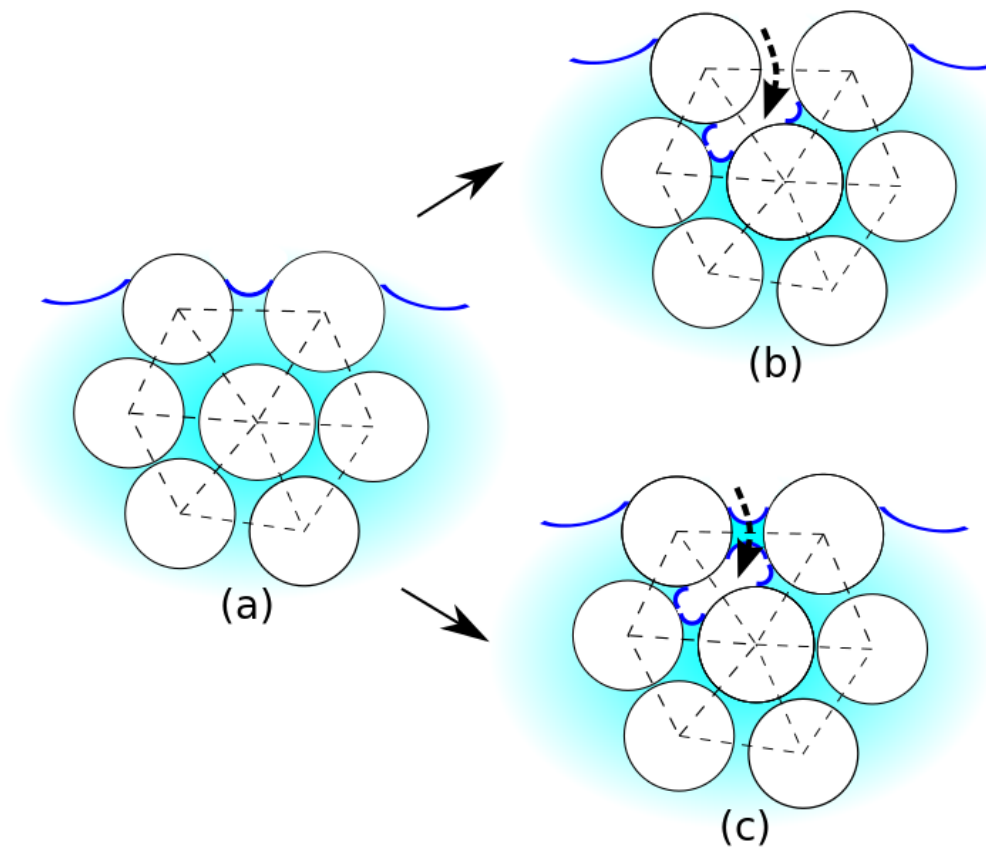


Figure 7.1: The displacement of NW-W interface between two equilibrium states. From (a) to (b), the pendular bridge is not considered in previous chapters; from (a) to (c), the pendular bridge exists, practically. (in 2D for clarity).

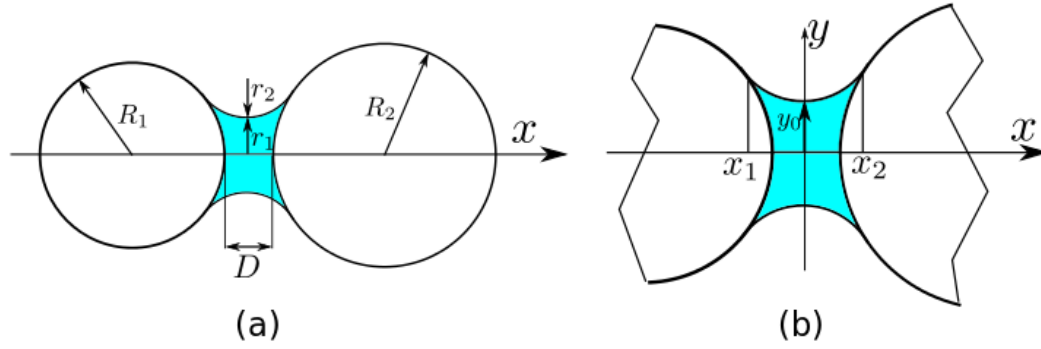


Figure 7.2: Illustration of a liquid bridge between two particles in pendular regime model. (a) global geometry and (b) details of the bridge, following Scholtès et al. (2009) and Scholtès et al. (2009a)

pendular bridge model. The key governing equations and assumptions will be reviewed. Then the logic of the extension and implementation will be elaborated. At last, we will apply the extended model to repeat the simulation of previous chapters and the effective stress parameter will be re-examined briefly.

7.2 Description of the pendular bridge model

In, namely, Soulie et al. (2006), Scholtès et al. (2009) and Chalak (2016), the unsaturated granular material is assumed in the pendular state, in which the W-phase inside the sample is exclusively composed by discontinuous menisci (i.e., liquid bridges). As mentioned in Section 3.2.2, the Young-Laplace equation describes the capillary pressure difference sustained across the interface between two static fluids, due to the phenomenon of surface tension. Combining Eq.3.1 and Eq.3.2 gives:

$$p^c = \gamma^{nw} \left(\frac{1}{r_1} + \frac{1}{r_2} \right) \quad (7.1)$$

where the principal radii r_1 and r_2 are formulated $\frac{1}{r_1} = \frac{1}{y(x)\sqrt{1+y'^2(x)}}$ and $\frac{1}{r_2} = \frac{y''(x)}{(1+y'^2(x))^{3/2}}$ in the Cartesian coordinates of Fig.7.2b. $y(x)$ defines the profile of the W-NW interface, and the x axis coincides with the axis of symmetry of the liquid bridge, passing through the centres of the connected sphere. The corresponding liquid bridge volume V and intergranular distance D can be defined by Soulie et al. (2006),

$$V = \pi \int_{x_1}^{x_2} y^2(x) dx - \frac{1}{3} \pi R_1^3 (1 - a \cos(x_1))^2 (2 + a \cos(x_1)) - \frac{1}{3} \pi R_2^3 (1 - a \cos(x_2))^2 (2 + a \cos(x_2)) \quad (7.2)$$

and

$$D = R_2(1 - a \cos(x_2)) + x_2 + R_1(1 - a \cos(x_1)) - x_1 \quad (7.3)$$

The capillary force F_{cap} due to a pendular bridge consists of two components: a force due to the surface tension acting on the W-NW-S contact line and a force due to suction

effects on the W-S interface. (A buoyancy force due to the partial submersion of the spheres may be considered, but it is negligible for spheres less than 1 mm in diameter (Princen, 1968).) It can be calculate by,

$$F_{cap} = \pi y^2 p^c + \frac{2\pi y}{\sqrt{1+y^2}} \gamma^{nw} \quad (7.4)$$

The pendular bridge model is based on solving Eq.7.1 numerically to determine the secondary variables (Eqs.7.2-7.4). The system can be expressed by,

$$\begin{cases} F_{cap} = F_{cap}(D, R_1, R_2, \gamma^{nw}, p^c) \\ V = V(D, R_1, R_2, \gamma^{nw}, p^c) \end{cases} \quad (7.5)$$

or

$$\begin{cases} F_{cap} = F_{cap}(D, R_1, R_2, \gamma^{nw}, p^c) \\ p^c = p^c(D, R_1, R_2, \gamma^{nw}, V) \end{cases} \quad (7.6)$$

Two modeling assumptions are possible:

(1) For the short-term/with-trap simulation, the volume of a pendular bridge V is assumed constant since the bridge is formed. The initial local p^c is subjected to the invasion sequence. Subsequently, the evolution of local p^c can be solved using Eq.7.6.

(2) For the long-term/without-trap simulation, mass transfer between the bridges is allowed. p^c is uniform and equals to the pressure difference of the reservoirs. V can be solved using Eq.7.5.

The model has already been implemented as part of Yade by Scholtès et al. (2009), Scholtès et al. (2009a) and Chalak (2016). For the implementation, in order to efficiently solve the above equations, an interpolation scheme on a set of discrete solutions of the Laplace equation has been developed to link directly p^c to F_{cap} and V for a given sphere-pair configuration (R_1, R_2, D) . Fig.7.3 illustrates the evolution of the capillary force with the relative displacement between two interacting particles. F_{cap} is maximum for particles strictly in contact ($D = 0$), and F_{cap} is considered constant for the range of elastic deformation ($D \leq 0$), assuming D to be very small compared with the particles radii. The maximum distance $D_{rupture}$ corresponds to the minimum D value from which the Young-Laplace equation has no solution.

7.3 Extending 2PFV to the pendular regime model

7.3.1 Algorithm

As mentioned in section 3.2.1, after the NW-phase invading a pore, we assumed the pore was completely drained in 2PFV-DEM model. Now we consider that a certain amount of W-phase is left between solid grains in the form of pendular rings. Fig.7.4 illustrates the extensions, in which the pendular bridge model is superposed on the network of 2PFV.

Sequence of drainage events

The drainage logic of extended 2PFV is the same as that of 2PFV, i.e., the invasion of single pore is determined by the relationship between p^c and p_e^c , and the invasion sequence

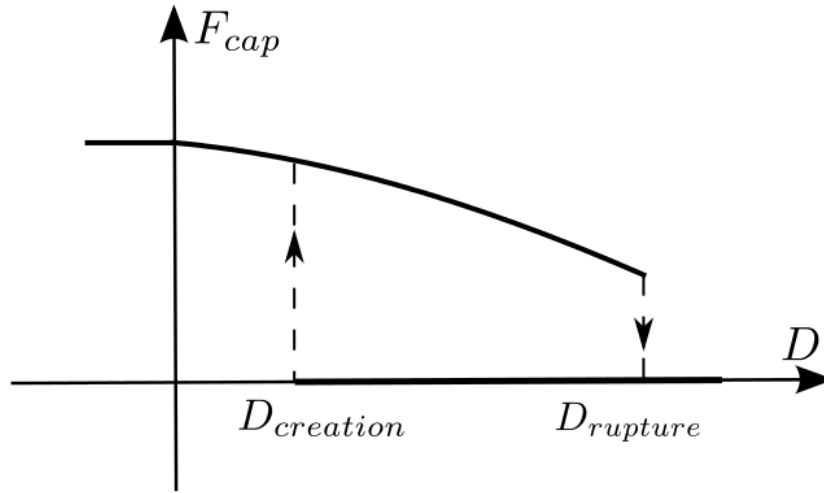


Figure 7.3: Evolution of the capillary force F_{cap} with the inter-granular distance D for a given capillary pressure value: a meniscus can form for $D < D_{creation}$ and breaks off for $D > D_{rupture}$, following Scholtès et al. (2009a)

is based on the topology of network. After each invasion event, a search algorithm is ran to find out the potential sphere-pair, which is may form a pendular bridge. The algorithm is operated on the edges of the tetrahedra of the network, which links the centers of two neighboring spheres (sphere-pair), for instance, O_1O_2 , O_1O_3 , O_2O_3 etc. in Fig.7.4. The sphere-pair leads to a potential bridge if all the neighboring pores have been invaded by the NW-phase. For example, in Fig.7.4 O_1O_2 is a potential sphere-pair, but O_2O_3 and O_3O_4 are not. Then the algorithm of the pendular bridge model (see previous section) is performed on each potential sphere-pair to determine if the liquid bridge can exist for the particular set $\{p^c, D, R_1, R_2, \gamma\}$. The evolution of the volume and the pressure of the pendular bridges and funicular clusters follow the same rules, i.e., a long-term (with-trap) drainage or a short-term (without-trap) drainage.

Mechanical component

In mechanical aspect, the capillary force F_{cap} of the pendular regime can be solved by following the algorithm of the previous section (Eq.7.5 and 7.6) . F_{cap} is taken into account in the time-integration by adding a pendular term to Eq.3.22, i.e.,

$$m\ddot{x}_i = F_i^c + mg + F_i^{fun} + F_i^{pen} \quad (7.7)$$

where F_i^{fun} and F_i^{pen} are the capillary forces of the funicular regime and pendular regime, respectively.

7.3.2 Implementation

We have implemented the extended model in Yade-DEM. Fig.7.5 shows the flow chart describing the extended 2PFV algorithm. The logic is similar with the flow chart of Fig.4.1.

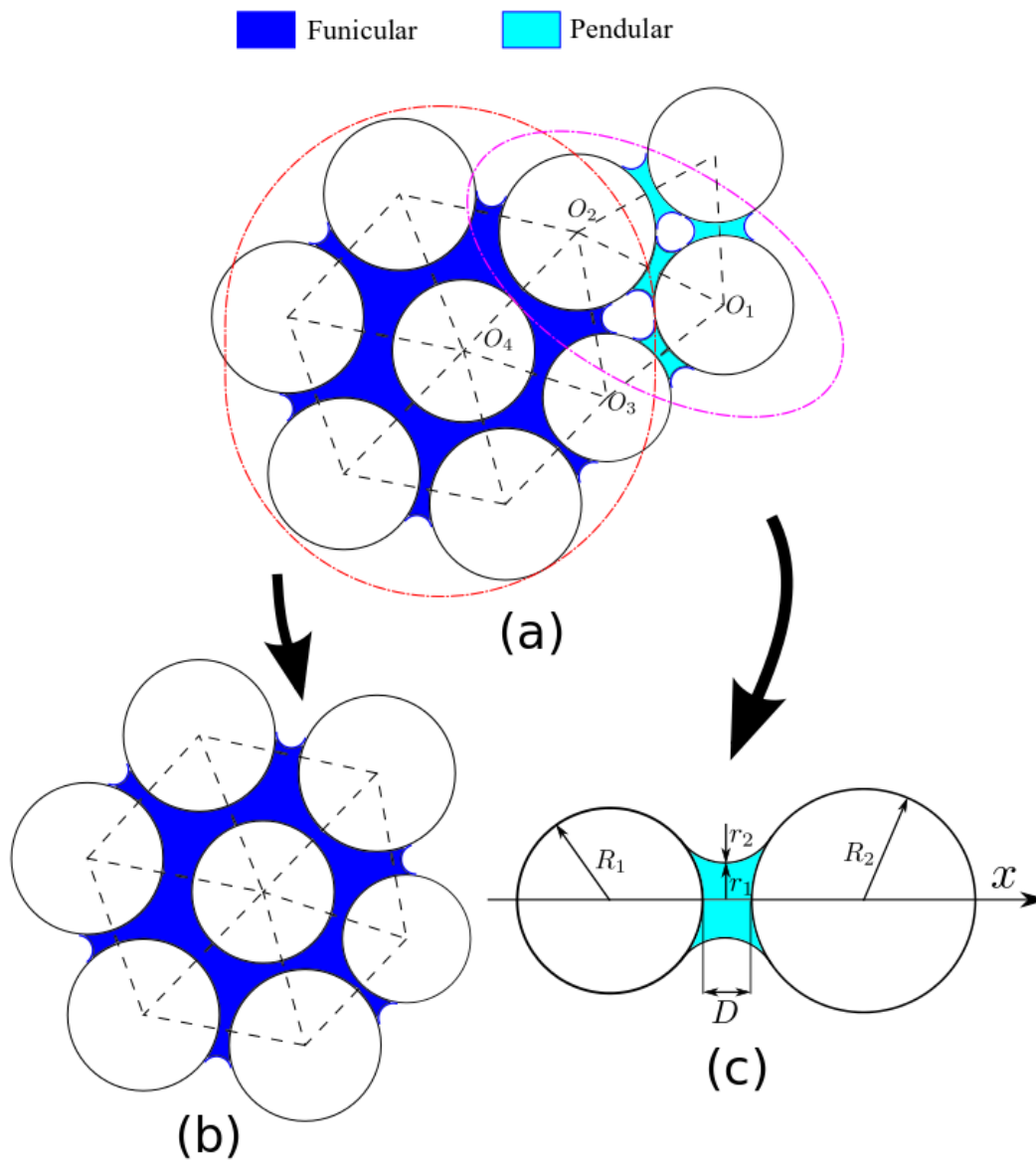


Figure 7.4: Illustration of the extended 2PFV model with the pendular bridge model, in 2D for clarity. (a) unsaturated granular material and the pore network of pore space. (b) the funicular cluster is modeled by 2PFV method. (c) the pendular bridge is modeled by Scholtès et al. (2009) and Chalak (2016)

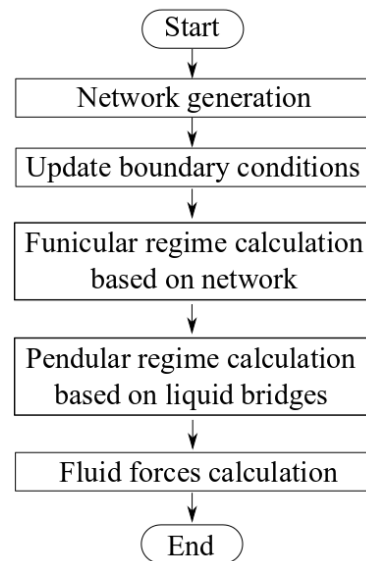


Figure 7.5: The extended 2PFV algorithm (one invasion step)

The following code fragment (Listing 7.1) shows how the extended 2PFV model is introduced in a simulation.

Listing 7.1: Introducing the extended 2PFV engine in a coupled DEM simulation

```

# The preamble of the script should setup a regular DEM simulation,
  defining particles properties and boundary conditions

# Instantiate a pendular liquid bridge model engine, which can be defined
  inside the calculation cycle.
O.engines=[
  #...
  Law2_ScGeom_CapillaryPhys_Capillarity1(label='pen'),
  #...
]

# Instantiate a funicular model engine.
fun=UnsaturatedEngine()

##set boundary conditions for the fluid phases, the drainage is controlled
  by decreasing W-phase pressure (pw) and keeping NW-phase pressure (pn
  ) constant.
fun.bndCondIsPressure=[0,0,1,1,0,0]
fun.bndCondValue=[0,0,pw_initial,pn,0,0]
fun.isPhaseTrapped=True #if True, "with-trap" drainage; if False, "without
  -trap" drainage.
fun.initialization()
fun.surfaceTension = surfaceTension
pen.imposePressure=False #If True, the pressure is imposed on all liquid
  bridges, i.e., "without-trap"; if False, the volume is assigned on
  each liquid bridge and is kept constant, i.e., "with-trap".

```

```

##create a list for handling the sphere-pairs
pairLists=[]
countPair=0

##start the invasion, the data of pc-sw-strain will be written into
pc_sw_strain.txt
file=open('pc_sw_strain.txt',"w")
for pw in arange(pw_initial,pw_end,pw_step): #decrease pw progressively
from pw_initial to pw_end, with a step of pw_step
    fun.bndCondValue=[0,0,pw,pn,0,0]
    #calculation the two-phase flow of funicular regime
    fun.invasion()
    #calculation the two-phase flow of pendular regime, by searching the
potential sphere-pair and assgining a liquid bridge
    pairLists.append(fun.getPotentialPendularSpheresPair())
    countPair+=1
    newList=list(set(pairLists[countPair]).difference(set(pairLists[
countPair-1])))
    for pair in newList:
        if 0.interactions.has(pair[0],pair[1]):
            if pair[0]>5 and pair[1]>5:
                0.interactions[pair[0],pair[1]].phys.computeBridge=True
                0.interactions[pair[0],pair[1]].phys.capillaryPressure=-fun.
                    bndCondValue[2]

    fun.computeCapillaryForce()
    # Add the fluid and interfacial forces (of the funicular regime) to the
total force on each body
    for b in 0.bodies:
        0.forces.addF(b.id, fun.fluidForce(b.id), True)
    # then integrate the dynamics with these additional forces, where the
capillary forces of the pendular regime will be calculated, until a
new equilibrium state is reached
    while 1:
        0.run(1000,True)
        unb=unbalancedForce()
        if unb<0.01:
            break
    file.write(str(pn-pw)+"_"+ str(fun.getSaturation(True)+getPenSaturation
        ())+ "_"+str(-triax.strain[1]-ei1_initial)+"\n")
file.close()

```

7.4 Numerical simulation

In this section we apply the extended 2PFV-DEM model to simulate a series of drainage process in order to investigate the effects of pendular bridges. The original 2PFV-DEM model and the pendular bridge model are also applied for comparison. The numerical

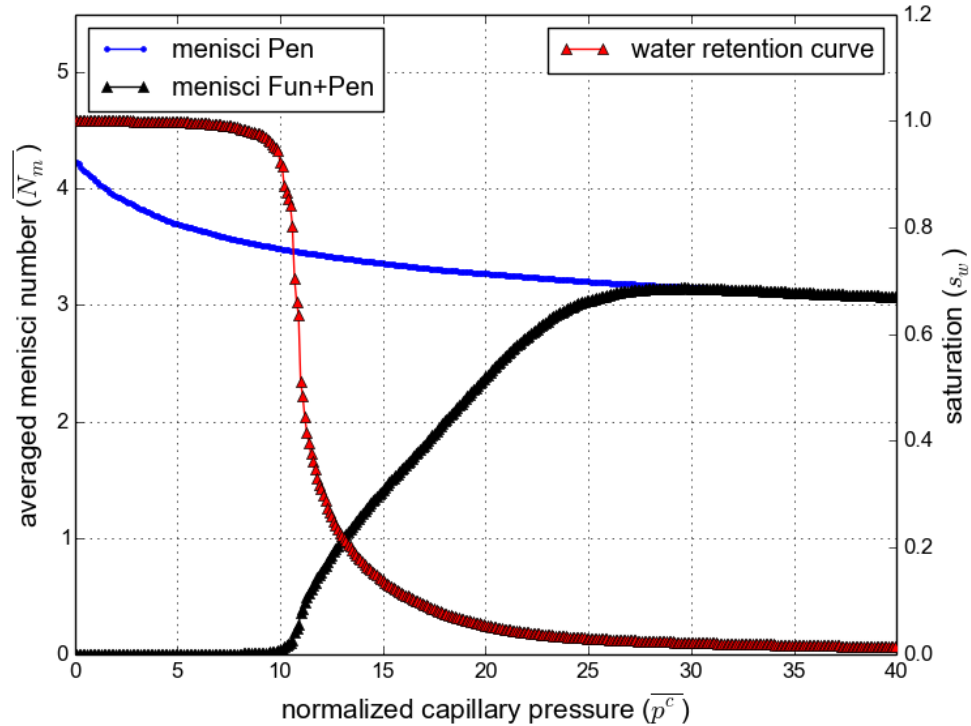


Figure 7.6: The evolution of menisci number of different models and water retention curve. Pen denotes pendular regime model (i.e., the liquid bridge in previous section); Fun+Pen denotes the extended 2PFV model, which includes funicular and pendular regimes. The water retention curve is corresponding to the Fun+Pen model.

setup follows section.4.2.3. The sample contains 40,000 particles. The drainage is under oedometer test conditions. Both “without-trap” and “with-trap” simulations are performed. The results are reported as follows, in which the 2PFV model is marked as “Fun” (funicular regime only), the pendular bridge model is marked as “Pen” (pendular regime only) and the extended 2PFV model is marked as “Fun+Pen” (funicular and pendular regimes), respectively.

7.4.1 Hydraulic results

Liquid bridge density

The amount of liquid bridges inside the sample not only affects the W-phase retention, but also plays an important role for the mechanical response, such as the macroscopic hysteresis in wetting and drying (Scholtès et al., 2009b). Thus the evolution of bridge number with capillary pressure is reported in the results, as shown in Fig.7.6, in which the average number of menisci per particle \bar{N}_m (i.e., liquid bridge density) is obtained. We perform the without-trap drainage tests using “Pen” model and “Fun+Pen” model for comparison. The water retention curve of the “Fun+Pen” model is superposed in the results for clarity of the evolution.

In the “Pen” model, the pendular bridges are superposed for all possible sphere-pairs.

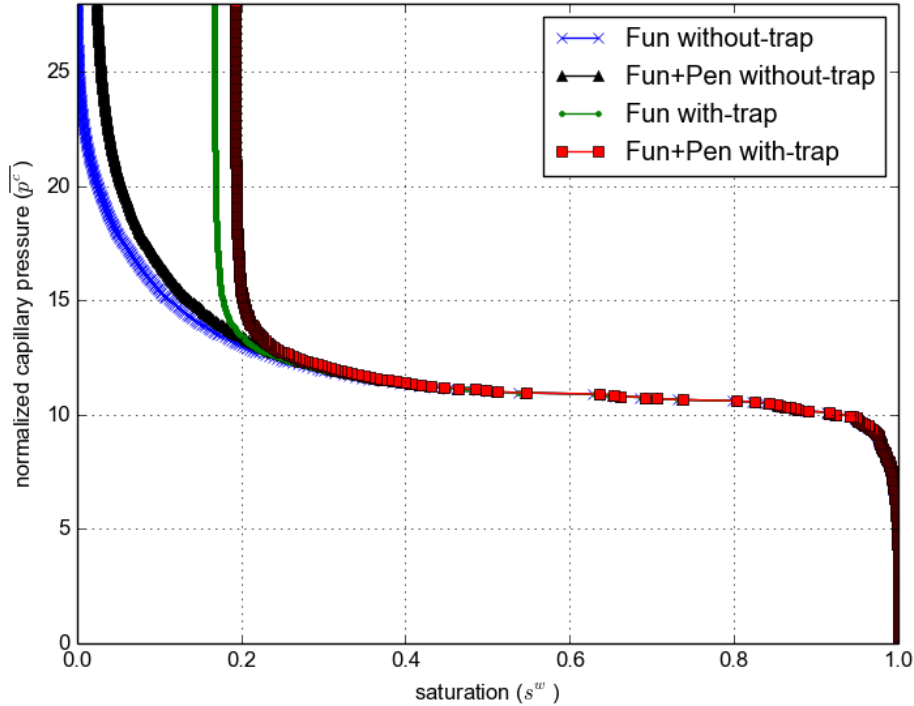


Figure 7.7: Water retention curves of different drainage models.

Thus, in the beginning \overline{N}_m is relative high. With increasing \overline{p}^c , \overline{N}_m decreases. That can be explained by the rupture of bridges. In the “Fun+Pen” model, the bridges appear only after the pores being drained. Thus, in the beginning no sphere-pairs are available for pendular rings (i.e., $\overline{N}_m = 0$). Then \overline{N}_m increases rapidly when $s_w < 0.2$. The curve merges with “Pen” model when $s^w \approx 0.03$. That means the sample is completely under the pendular regime. The simulations of “Pen” model and “Fun+Pen” model are exactly the same scenario. Finally, \overline{N}_m decreases as well because of the ruptures. But the liquid bridge between two contact particles will never be erased.

Water retention curve

The water retention curves (WRC) are obtained with the different assumptions and reported in Fig.7.7. For both “without-trap” and “with-trap” simulations, the effects of pendular bridges are negligible as long as $s^w > 0.25$. Since in this stage, very few bridges can be formed between solid grains. Even when s^w is relatively low, $0.25 < s^w < 0.5$, for instance, most of the W-phase is in the funicular regime (see the liquid bridge density in Fig.7.6). The remarkable effects of pendular bridges can only be found at the end of drainage ($s^w < 0.2$), in which more and more sphere-pairs are available for the formation of bridges. At residual saturation, the volume of bridges contributes approximately to 0.03-0.05 in the total saturation.

Discussions

The pendular bridge modeling has been widely used for the hydromechanical couplings of unsaturated granular materials. Usually, in the initial state, the bridges are superposed randomly for all possible sphere-pairs of the specimen (e.g., Scholtès et al., 2009; Chalak, 2016). Then different loading/unloading, or drying/wetting paths can be proceeded. But how to obtained experimentally the initial state of the specimen is rarely mentioned. The calibration of the pendular bridge model is usually focused on only a single sphere-pair.

If we compare the evolution of liquid bridge density for “Pen” model and “Fun+Pen” model, we can find that before the collapse of both cases, the results of “Pen” model is not realistic. The liquid bridge density is highly overestimated. Mathematically, we can superposed the liquid bridges for all possible sphere-pairs, but the distribution may never be obtained experimentally. This problem is rarely noticed in previous pendular bridge models.

To conclude, the “Pen” (pendular only) model is only suitable for a pure pendular regime, in which the overlap of menisci should not happen and the funicular cluster of W-phase should not exist. We recommend the “Pen” model can only be valid for the sample with a saturation $s^w < 0.05$. The “Fun+Pen” model considers the funicular wetting phase clusters and pendular rings separately, thus it can reproduce the entire evolution of the W-phase.

7.4.2 Mechanical results

Deformation of solid skeleton

The relationship between capillary pressure and deformation are reported in Fig.7.8 and Fig.7.9. For clarity, the WRC is also superposed in the figures. For both “with-trap” and “without-trap” drainage, the evolution of deformation of “Fun+Pen” model is similar with that of “Fun” model, i.e., the sample first shrinks then swells. The physical explanation is also similar, as narrated in section 4.2.2. Here we only focus on the effects of pendular bridges.

We also first identify the deformations of solid phase in two models are of small amplitude and elastic in order to ensure the simulation results are valid. The confirmation is shown in Fig.7.10, in which the strain-stress relationship (i.e., shrinking and then swelling) during the drainage is linear and reversible.

The effects of pendular bridges can be found in the swelling stage of the drainage when s^w is less than 0.5. The capillary forces induced by pendular bridges (see Eq.3.22 and Eq.7.7) keeps the particles together. Comparing with the effects on WRC, i.e., the volume of bridges contributes 0.03-0.05 of the saturation, the mechanical effects are more remarkable, especially for “without-trap” simulation. In “with-trap” simulation, at the end of drainage, the deformation induced by the pendular liquid bridges takes up approximately 30%. In “without-trap” simulation, at the end of drainage, the deformation is entirely controlled by the liquid bridges, and such deformation is clearly not negligible.

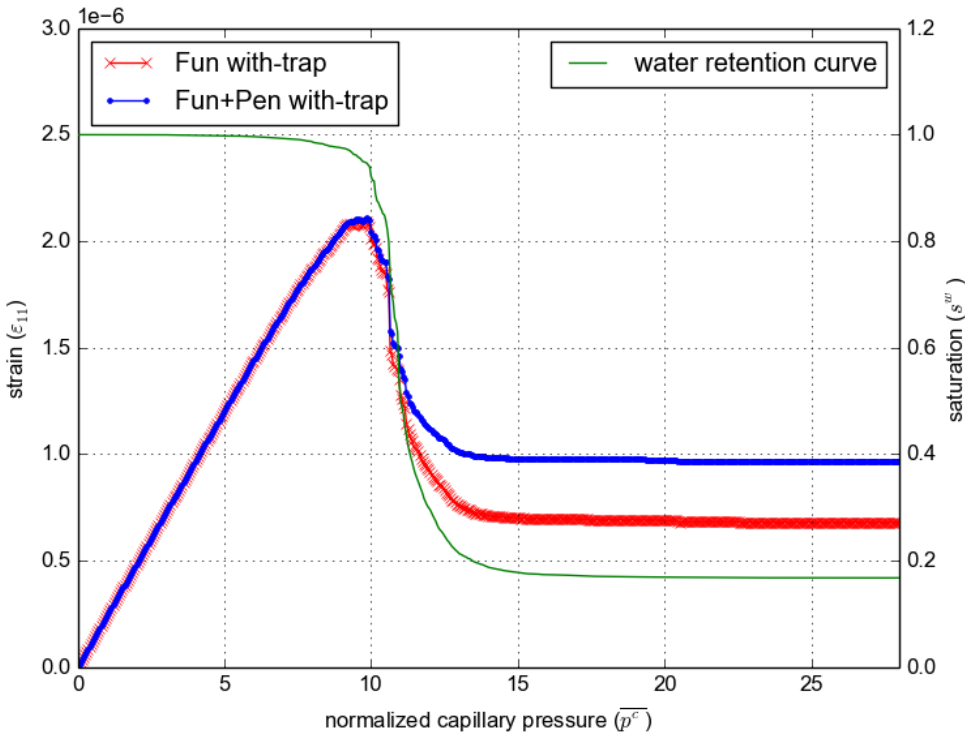


Figure 7.8: The relationships between normalized capillary pressure, saturation and one-dimensional deformation (\bar{p}^c - s^w - ϵ_{11}) in with-trap model, under the oedometer test conditions. The WRC corresponds to the Fun+Pen model.

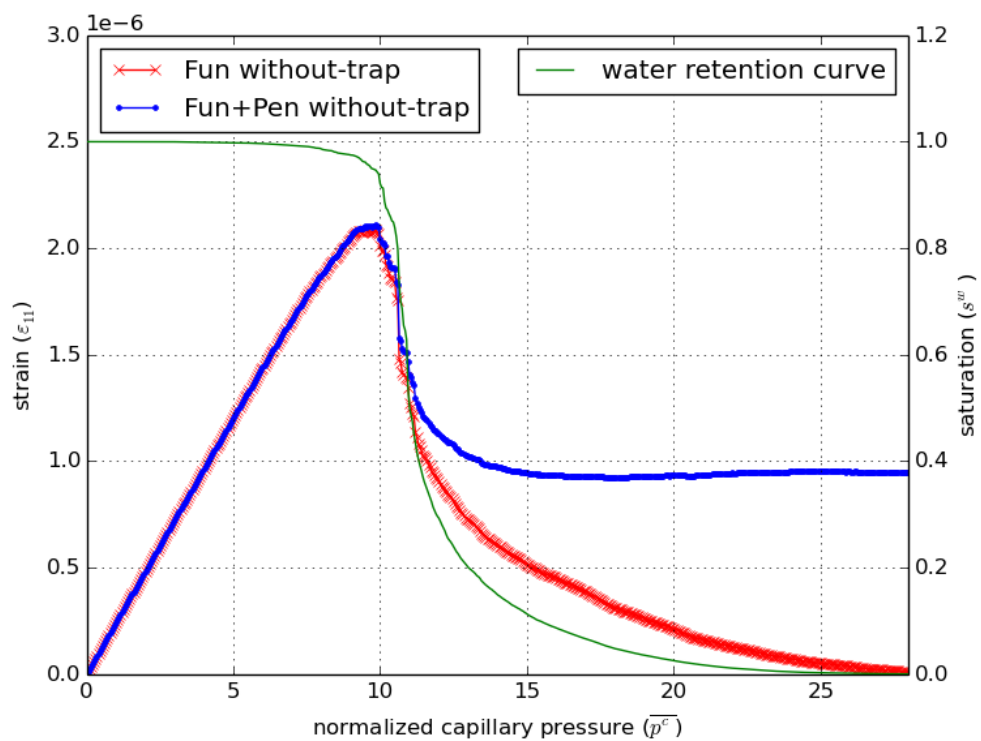


Figure 7.9: The relationships between normalized capillary pressure, saturation and one-dimensional deformation (\bar{p}^c - s^w - ϵ_{11}) in without-trap model, under the oedometer test conditions. The WRC corresponds to the Fun+Pen model.

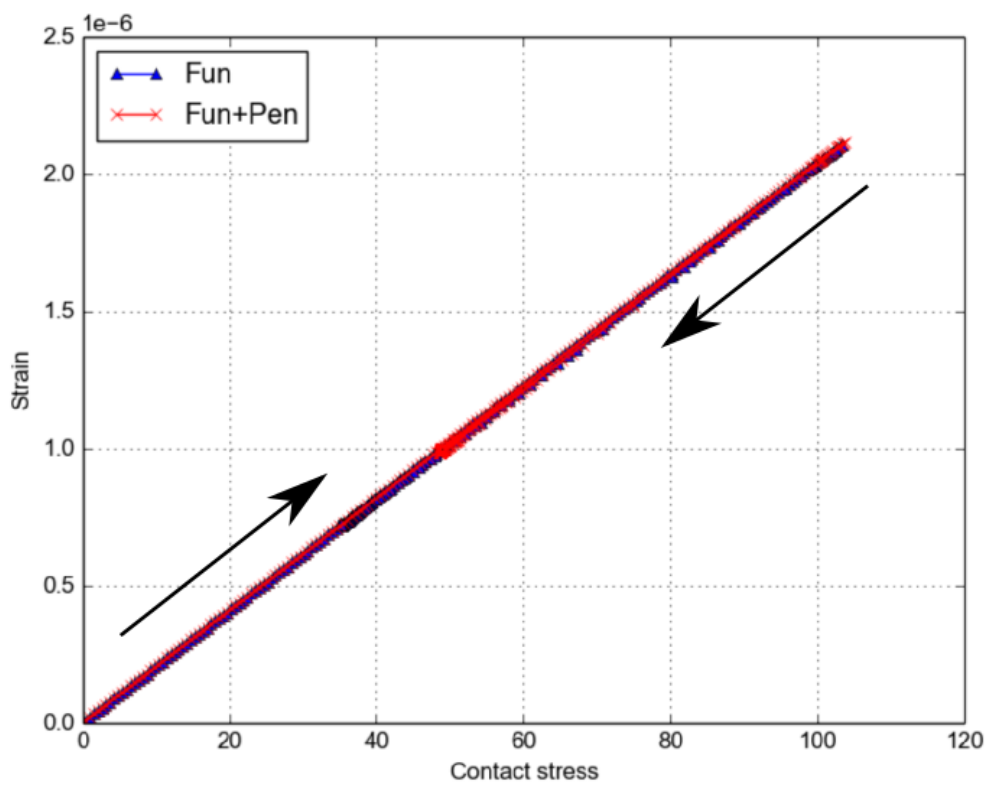


Figure 7.10: The linear and reversible evolution of strain and contact stress during the drainage using “Fun” model and “Fun+Pen” model. The samples first shrink, then swell.

Microscopic interpretation

The effects of liquid bridges can also be analyzed from the microscopic point of view. We calculate the capillary stress induced by the fluids on the basis of particle-centered volumes using the method of Eq.6.5. The contributions from funicular W-phase clusters and pendular W-phase bridges are calculated separately. The results are presented with the same normalization as p^c (see Eq.4.1), i.e.,

$$\overline{\sigma_{11}^{fun}} = \frac{\sigma_{11}^{fun} \overline{D}}{\gamma^{nw}}, \overline{\sigma_{11}^{pen}} = \frac{\sigma_{11}^{pen} \overline{D}}{\gamma^{nw}} \quad (7.8)$$

where σ_{11}^{fun} and σ_{11}^{pen} are the capillary stress components caused by funicular clusters and pendular bridges, respectively; $\overline{\sigma_{11}^{fun}}$ and $\overline{\sigma_{11}^{pen}}$ are their normalized values; \overline{D} is the average sphere size, and γ^{nw} is interfacial tension. The results of “with-trap” and “without-trap” simulations are reported in Fig.7.11 and Fig.7.12, respectively.

In “with-trap” simulation, when the sample is saturated, the total of capillary stress always equals to the capillary pressure (see Fig.7.11, the slope of the curve equals to 1 in the beginning of drainage.). It can be explained by Terzaghi’s effective stress principle. At this stage, $\overline{\sigma_{11}^{pen}} = 0$, since there are no pendular bridges. $\overline{\sigma_{11}^{fun}}$ keeps growing until reaching the peak value. Then $\overline{\sigma_{11}^{fun}}$ decreases and $\overline{\sigma_{11}^{pen}}$ increases. At the end of drainage, $\overline{\sigma_{11}^{fun}}$ and $\overline{\sigma_{11}^{pen}}$ are constant, and the funicular component is larger than pendular.

In “without-trap” simulation, the evolutions of $\overline{\sigma_{11}^{fun}}$ and $\overline{\sigma_{11}^{pen}}$ are quite similar for the beginning stages. But at the end, $\overline{\sigma_{11}^{fun}}$ is approaching to 0 and the pendular component is dominant, since only pendular bridges left.

To sum up, since the deformations of the solid phase in “Fun” model and “Pen” model are both assumed elastic and the strain-stress relationship is linear (see Fig.7.10), the evolution of the capillary stresses which are obtained on basis of micromechanical contact forces can reflect the macro-scale deformation of the solid skeleton. Although the pendular liquid bridges contribute a small content of saturation, the induced capillary pressure (i.e., $\overline{\sigma_{11}^{pen}}$) is remarkable.

Re-examination of Bishop’s effective stress parameter

By following the procedures of section 6.3, we re-examine Bishop’s effective stress parameter χ using the extended 2PFV (Fun+Pen) model. Both with-trap and without-trap simulations are performed. The macro expression χ^M and micro expressions χ^m are obtained on basis of Eq.6.4 and Eq.6.7. We superpose the results of 2PFV (Fun) model for comparison. The experimental data of Breahed silt (Donald, 1961) and Vaich moraine (Bishop and Blight, 1963) is also included.

The results are reported in Fig.7.13 and Fig.7.15. In all cases, the values of χ^M and χ^m are very similar. Both parameters are above the $\chi = s^w$ line. Adding pendular bridges increases χ .

In with-trap simulation, the parameters show a trend of breaking down at a low s^w . Without-trap, there is no such breakdown. Such difference is mainly induced by the different scenarios of capillary effects. As explain in section.6.3.3, when saturation is low,

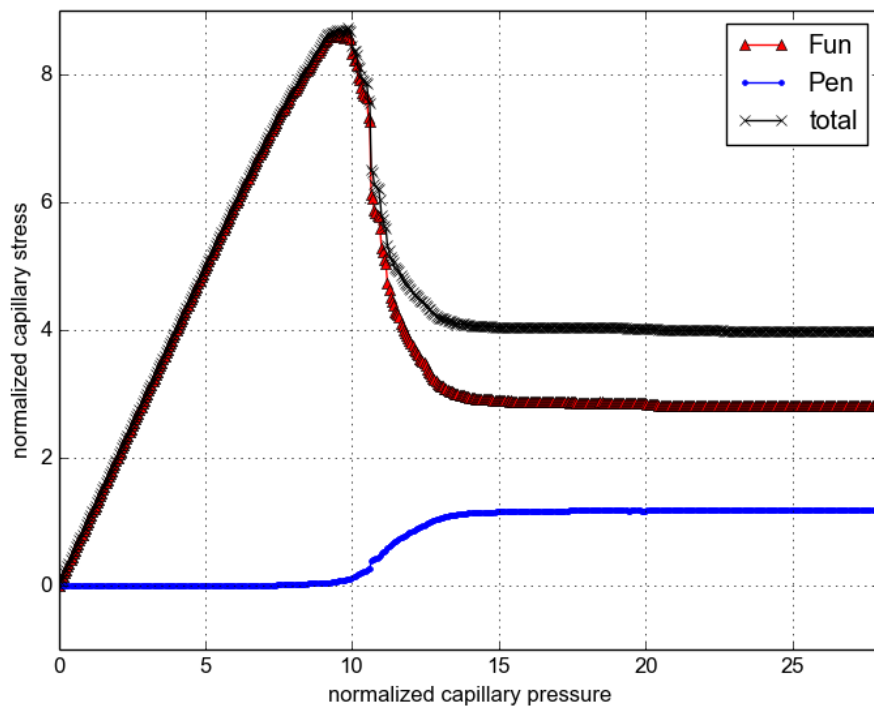


Figure 7.11: The relationship between the capillary stress and capillary pressure in with-trap drainage. All variables have been normalized.

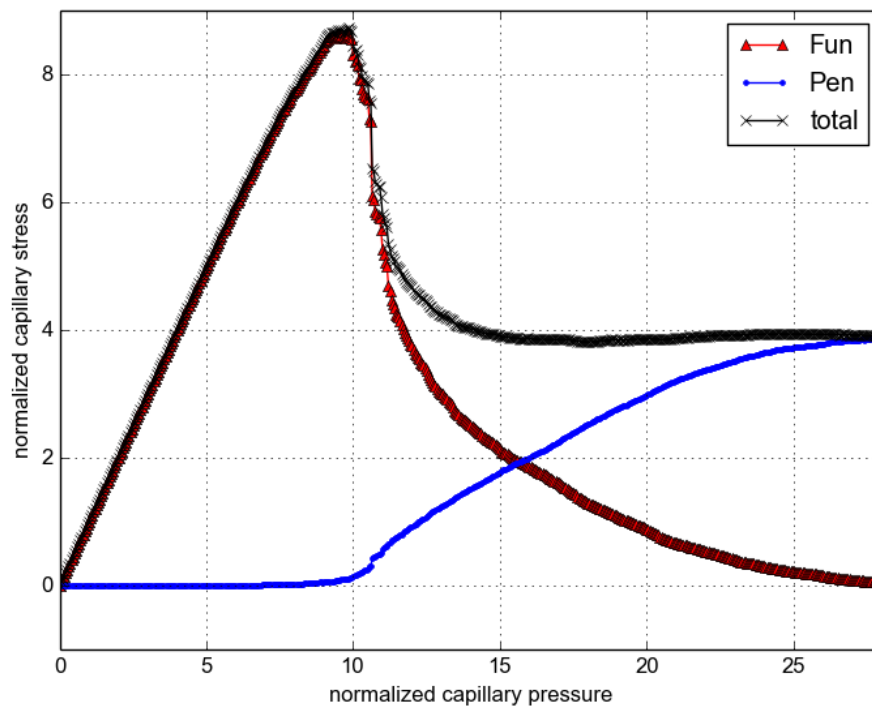


Figure 7.12: The relationship between the capillary stress and capillary pressure in without-trap drainage. All variables have been normalized.

the increase of p^c will not significantly change the deformation of the solid skeleton in with-trap model, since it does not change the capillary pressure of the disconnected W-phase. But if we assume the individual W-phase cluster/bridge always connects to the W-reservoir (i.e., the without-trap model), then the capillary forces will always be affected by the changes of p^c , consequently, leading to a deformation.

We present the normalized difference, $\frac{\chi^M - \chi^m}{\chi^M}$, for “Fun” and “Fun+Pen” models. The difference $\frac{\chi^M - s^w}{\chi^M}$ for $\chi = s^w$ is also superposed in the results, as show in Fig.7.14 and Fig.7.16. We find out that,

- When $s^w > 0.3$, in the funicular regime dominated scenarios (since few pendular bridges can be formed, see Fig.7.6), the maximum error is less than 1% (for both “Fun” and “Fun+Pen” models). When $s^w < 0.3$, the error grows, but its maximum value is less than 10% (for “Fun+Pen” model, in without-trap simulation the error is less than 5%; in with-trap it is less than 1%). Thus, we conclude that the micromechanical contact stress can be used to estimate the effective stress under the pendular and funicular regimes. Even in a pendular regime dominated scenario, such estimation is still acceptable.
- The results suggest that $\chi = s^w$ might be an acceptable approximation when the saturation level is high. The error is increasing as p^c increases and it reaches 70% (35% for with-trap simulation) at low level of saturation.

Conclusions

In this chapter, we have extended the 2PFV-DEM scheme to the pendular regime, using the pendular bridge model of Scholtès et al. (2009), Scholtès et al. (2009a) and Chalak (2016).

- The pendular bridge model has been briefly reviewed, and, namely, the difference between constant suction and constant volume assumptions have been commented. They combine consistently with the “without-trap” and “with-trap” assumptions of the 2PFV-DEM scheme, respectively. The implementation has been done within YADE platform.
- We have repeated the primary drainage tests under the oedometer conditions similar to the tests of previous chapters in order to learn the effects of pendular liquid bridges. The results show that the volume of liquid bridges contributes approximately 0.03-0.05 of the residual saturation (the residual saturation ≈ 0.2), and the induced deformation is remarkable. For a “with-trap” drainage, the deformation from pendular regime takes up 30%. For a “without-trap” drainage, the deformation from pendular regime dominates.
- Further more, we have re-examined Bishop’s effective stress parameter from macroscopic and microscopic views using the extended model. A noticeable increase of χ compared with the “Fun” model has been observed due to the pendular bridges. The values of χ^M and χ^m are not exactly the same, but the difference is very small

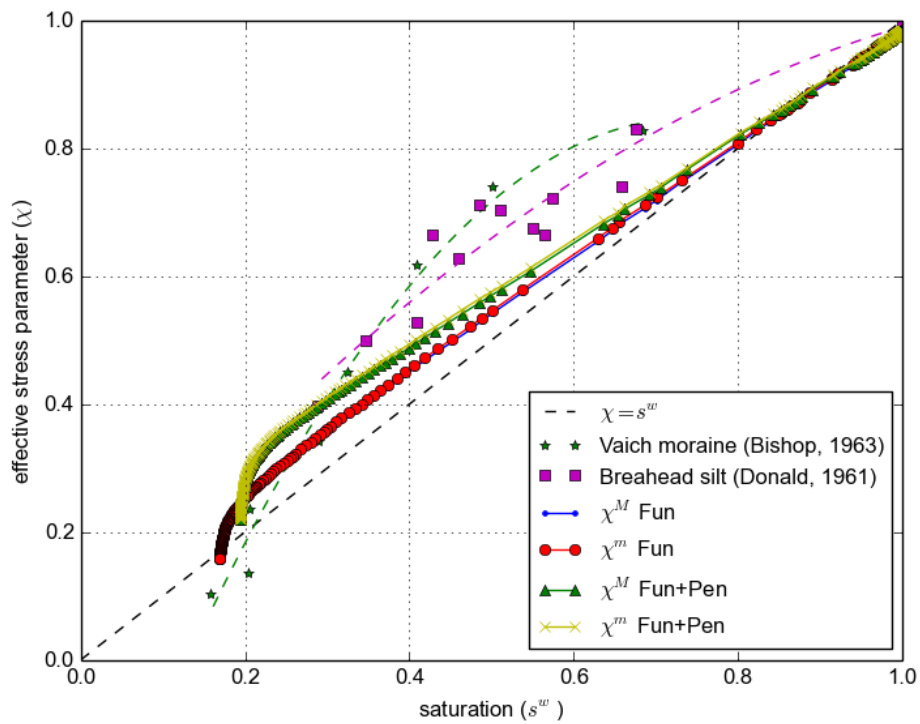


Figure 7.13: Comparison of effective stress parameter between funicular regime model and pendular+funicular regime model. The simulation is controlled by with-trap drainage.

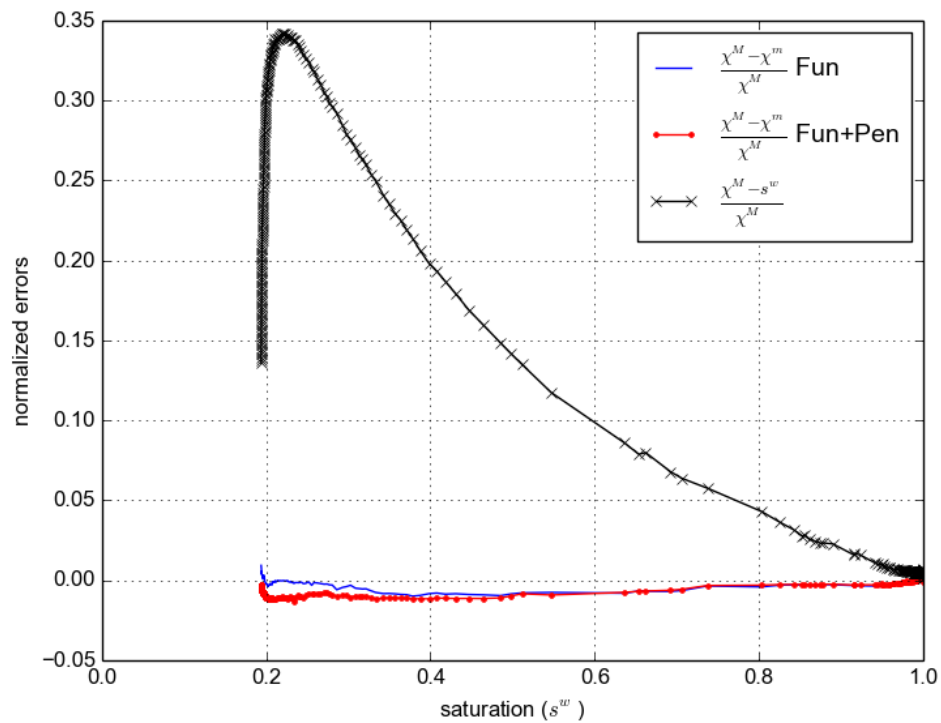


Figure 7.14: Variation of $\chi^M - \chi^m$ with saturation in with-trap simulations.

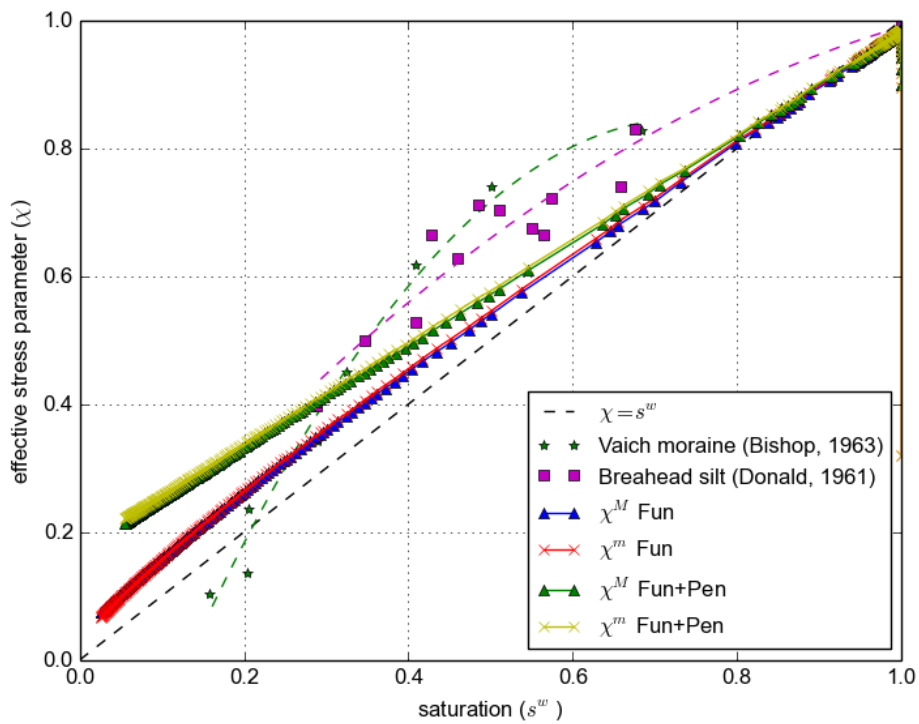


Figure 7.15: Comparison of effective stress parameter between funicular regime model and pendular+funicular regime model. The simulation is controlled by without-trap drainage.

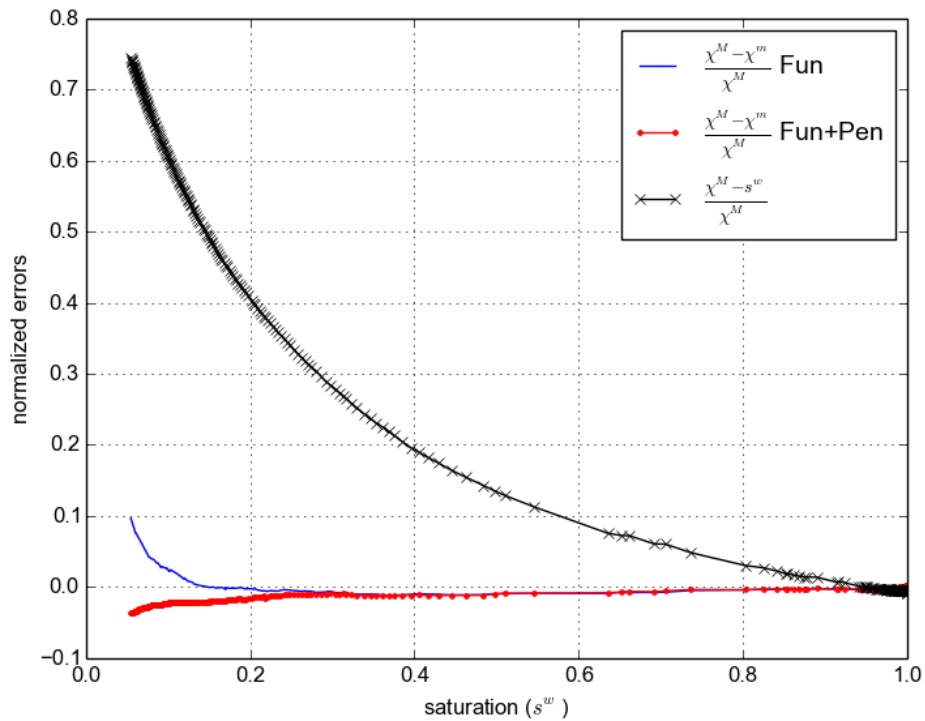


Figure 7.16: Variation of $\chi^M - \chi^m$ with saturation in without-trap simulations.

(the error is less than 10%). We conclude that in the “funicular + pendular” regime the micromechanical stress can be used to estimate the effective stress of the unsaturated granular materials. In the pure pendular regime, the error grows (this point is highlighted by (Chalak, 2016)), but the estimation is still acceptable.

Conclusions and Perspectives

The main objective of this thesis was to provide an efficient numerical methodology for reproducing the hydraulic and mechanical behaviors of the partially saturated granular media. We focused on a pore-scale coupled scheme, in which a decomposition technique and the discrete element method (DEM) have been combined for the fluids and the solid grains, respectively. An explicit link has been established between the geometry of the pore space and the position of the grains. The model was specifically designed for simulating the quasi-static drainage of large random poly-disperse sphere packings. By “large” we imply problem with more than 10^4 solid grains, i.e., a size beyond reach of most conventional coupled methods (DEM-LBM, DEM-SPH, etc.). This final chapter covers the main conclusions of the research described in the thesis, together with perspectives for future work on the improvement and extension of the current implementation.

Conclusions

In part 1, the literature review has presented the theoretical background relevant to complex multiphase systems, in which each component phase has been introduced. We concluded that the pore-scale modeling was an efficient and promising approach for hydraulic simulations.

In part 2, we have presented the pore-scale approach in details, where the model was termed “two-phase pore-scale finite volume - discrete element method” coupling scheme, or “2PFV-DEM”. The solid phase has been idealized as a random dense packing of poly-disperse spheres, which was generated with the discrete element method (DEM). The decomposition of the pore space has been obtained using Regular Triangulation method. Under the quasi-static regime, the model simulates only equilibrium states along a drainage path with a uniform pressure field in each fluid. The drainage thus occurs through a recursive invasion of the pores when the capillary pressure exceeds the local entry values. The criterion for invading a local pore has been formulated based on Mayer-Stowe-Princen (MS-P) method, which employed the balance of forces on the fluids interface. The receding wetting phase can either be disconnected from its reservoir by the nonwetting phase, leading to a residual saturation or be drained completely at the end. We have considered both situations. The capillary forces induced by the fluids pressure and interfacial tension have been evaluated and taken into account when solving the motion of the solid grains with the DEM. The macro-scale deformation of simulated materials finally can be obtained. We assumed that the deformation was of small amplitude and that it was not causing great changes in the network. The current implementation is a one-way coupling.

Under oedometer conditions, a series of primary drainage tests has been performed. Taking the experimental data as reference, the capillary pressure - saturation curves (water retention curves) obtained with the model are well predicted. During drainage, the solid skeleton showed first shrinking then swelling.

With our current implementation the complete network generation is achieved in less than 10 s for 64,000 spheres on a standard workstation (Intel Xeon 2.80GHz, executed on one single core); the cost of an invasion step (finding the stable phase distribution corresponding to one value of capillary pressure and calculating the fluid forces) depends on the number of invaded pores hence fluctuates during a simulated drainage. For 64,000 spheres it never exceeds 1.0 s.

In part 3, we have applied the 2PFV-DEM model to approach two hydromechanical issues.

- We assessed size effects and boundary effects on primary drainage when testing small samples. Repeated simulations showed that the standard deviation of the saturation follows a simple variance reduction law with increasing sample size. Standard deviation should not be the unique criterion for evaluating the representativity. The sample size can be the cause of significant bias in the average result. We found that at least 20,000 spheres must be used in order to reduce the bias below 0.02 in terms of the saturation for a give capillary pressure. For the boundary effects, we found that the preferential invasion occurring along the boundaries led to more robust evaluation of the capillary pressure - saturation relations, else the phase distribution always showed a strong gradient of saturation.
- We examined Bishop's effective stress parameter χ . The evolution of χ has been derived from macroscopic deformation and microscopic variables, where the macroscopic expression uses the definition of effective stress and the microscopic expression is based on the contact stress between solid grains. The results show that both ways lead to very similar results. We conclude that the micromechanical intergranular stress can be considered as the micro-scale expression of effective stress. The local effective stress parameter and local saturation have been obtained by local averaging. A unique trend in the evolution of the effective stress parameter as a function of saturation has been observed.

Lastly, the 2PFV-DEM scheme has been extended to include pendular bridges. The capillary effects of liquid bridges have been systematically evaluated. The fluid in pendular state contributed to a small amount to the total saturation but the induced deformation of the solid skeleton is remarkable. In this "funicular + pendular" regime, the microscopic stress and effective stress have been found to be quite close again.

Perspectives

Our coupling scheme that combines a pore-scale network and the DEM for the fluid(s) and solid grains respectively can be considered as an extensible platform for simulating multiphase systems. In fact, our coupling is itself for a large part an extension of the PFV-DEM coupling for one phase flow, introduced by earlier authors. The PFV-DEM model

has been found to be an effective approach for one-phase flow in deformable granular materials (PhD of Emanuele Catalano, Catalano (2012); Chareyre et al. (2012); Catalano et al. (2014) and Donia Marzougui Marzougui et al. (2015); Marzougui (2014) in Laboratoire 3SR). The current 2PFV-DEM has been applied to the quasi-static drainage in this work, but it is not a strong requirement. Regarding the possible extensions of the current implementation, several aspects can be mentioned.

Improvements, Extensions and Applications of 2PFV-DEM itself

Boundary conditions. The current boundary conditions of invasion consider that the fluid can either go through the throats along the boundary or only flow inside the solid bulk. The implementation of periodic boundary conditions is in progress and will offer an interesting alternative to simulate boundary effects.

Dynamic regime. We assumed the drainage in quasi-static regime. This assumption could be relaxed including dynamic situations, where the motion of fluids themselves (both wetting and nonwetting phases) can be considered. For each individual fluid, its motion (flux through pores) and the fluid pressure gradient can be obtained by the one-phase PFV-DEM model without major difficulties. Significant steps in this direction have been done already at Utrecht Environmental Hydrology group (PhD of Thomas Sweijen, partly in collaboration).

Imbibition. The local motion of fluids interface can cause drainage or imbibition of a pore. The local criteria are different. In drainage, the invasion is controlled by the entry value of pore throat; in imbibition, it is decided by the entry value of pore body. Thus if we adapt the local criterion, the 2PFV-DEM is able to simulate the imbibition. Also the dynamic imbibition is possible. Again, this work is in progress at Utrecht University (Sweijen et al., 2016).

Applications. We have applied the model to simulate the primary drainage under the oedometer test conditions. In the future, we will employ the model or its extensions to learn more hydromechanical evolutions, such as the volumetric and shear strength behaviors under different loading/unloading or drying/wetting paths (especially the wetting collapse behavior). Many interesting phenomena can now be approached by DEM simulations, namely the capillary shrinkage cracking of particle aggregates can be reproduced.

Combinations with other approaches

Chapter 7 has presented a possible combination with the pendular bridge models, as developed by Scholtès et al. (2009); Scholtès et al. (2009a) and Chalak et al. (2016); Chalak (2016) (former doctors of Laboratoire 3SR). Other pore-scale/grain-scale or micro-scale continuum based methods can also be introduced for the combinations.

Local criteria We estimated the local threshold value (entry capillary pressure) for a pore by following Mayer-Stowe-Princen (MS-P) method. Though qualitatively acceptable based on comparisons with experimental water retention measurements, those local values remain to be validated at the very small scale. The same remark applies for the expressions of the forces exerted on each solid grain. In the future, these local rules may also be defined numerically by using Lattice-Boltzmann (LB) method (PhD of Puig Montella Eduard in Laboratoire 3SR and Universitat Politècnica de Catalunya) or experimentally

using tomography techniques (post-doc of Khan Faisal in Laboratoire 3SR). The invasion logic is the same, but at micro-scale the entry value will be defined precisely based on the geometry of the throat with LB method. This work is in progress by Puig Montella Eduard.

Appendix

Calculation of capillary force and tension force for a pore throat

¹In this appendix, we give explicit expressions of the capillary force \mathbf{F}^c and tension force \mathbf{F}^t acting at a pore throat.

We consider a pore throat (see Fig.7.17) defined by the radii and positions of neighboring solid particles. For a particular radius of curvature r^c of the NW interfaces and in perfectly wetting condition (contact angle $\theta = 0$) the contact line between NW and W phases is tangent to the solid surface.

The area of the triangle ΔABC can be written as follows:

$$A_{\Delta ABC} = \frac{1}{2}bc \sin \alpha \quad (7.9)$$

Using laws of cosines, we can write the following equations to solve α , β and γ in ΔABC ,

$$a^2 = b^2 + c^2 - 2bc \cos \alpha \quad (7.10)$$

$$b^2 = a^2 + c^2 - 2ac \cos \beta \quad (7.11)$$

$$c^2 = a^2 + b^2 - 2ab \cos \gamma \quad (7.12)$$

Likewise, the areas and φ_{ij} in ΔAO_3B , ΔBO_1C and ΔAO_2C can be obtained.

The total area of liquid bridge A_{lb} within the throat's section (the part occupied by the W-phase) is

$$\begin{aligned} A_{lb} = & (A_{\Delta AO_3B} - 0.5R_1^2\varphi_{31} - 0.5R_2^2\varphi_{32} - 0.5r_c^2\varphi_{33}) \\ & + (A_{\Delta BO_1C} - 0.5R_2^2\varphi_{12} - 0.5R_3^2\varphi_{13} - 0.5r_c^2\varphi_{11}) \\ & + (A_{\Delta AO_2C} - 0.5R_1^2\varphi_{21} - 0.5R_3^2\varphi_{23} - 0.5r_c^2\varphi_{22}) \end{aligned} \quad (7.13)$$

The area A^{eff} corresponding to the invading NW-phase, and on which p^c is exerted can finally be evaluated as:

$$A^{eff} = A_{\Delta ABC} - A_{lb} - 0.5R_1^2\alpha - 0.5R_2^2\beta - 0.5R_3^2\gamma \quad (7.14)$$

Combining Eq.(3.4), (3.6) and (7.14), an explicit expression of \mathbf{F}^c is obtained.

¹The algorithm of this section has been published as part of the conference proceeding Yuan et al. (2015a)

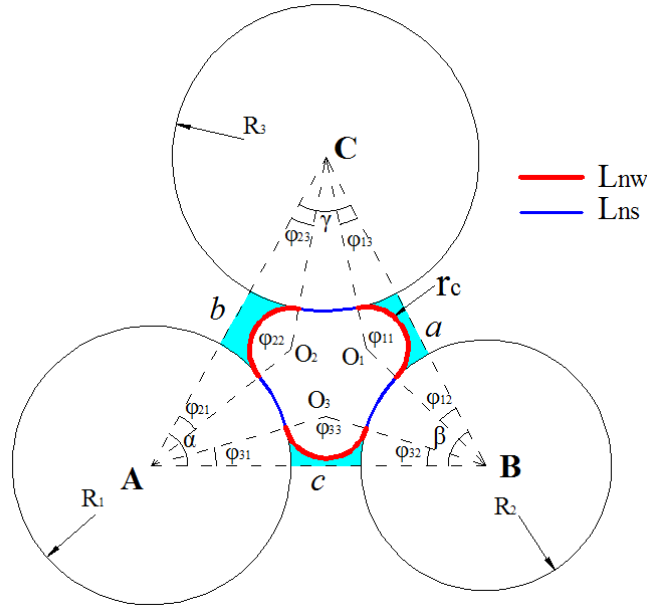


Figure 7.17: Cross section geometry of pore throat, the pore throat radius r^c is determined based on the balance of forces for non-wetting/wetting interface.

We now evaluate the force coming from the interfaces. Since $\theta = 0$ in Eq.(3.9) for perfect wetting, the total force on the interface line is

$$\mathbf{F}^t(r^c) = (L_{nw} + L_{ns})\gamma^{nw}\mathbf{n} \quad (7.15)$$

The contact lines L_{nw} and L_{ns} can be obtained as follows:

$$L_{nw} = r_c\phi_{11} + r_c\phi_{22} + r_c\phi_{33} \quad (7.16)$$

$$L_{ns} = R_1(\alpha - \phi_{21} - \phi_{31}) + R_2(\beta - \phi_{32} - \phi_{12}) + R_3(\gamma - \phi_{13} - \phi_{23}) \quad (7.17)$$

Combining equations (7.15), (7.16) and (7.17) gives an explicit expression of $\mathbf{F}^t(r^c)$.

Determination of lower and upper bounds of r^c

For a particular geometry, we define lower and upper bounds for r^c , denoted by $[r_{min}, r_{max}]$. The maximum value r_{max} is defined as the radius the circle inscribed between the solid particles, i.e. the solution of Apollonius's problem in Euclidean plane geometry. We solve for r_{max} by using the algorithm of Chareyre et al. (2012).

The minimum value r_{min} is locally determined by the maximum distance between two neighboring particles, which is obtained by:

$$r_{min} = \frac{1}{2}\max\{(a - R_2 - R_3), (b - R_1 - R_3), (c - R_1 - R_2)\} \quad (7.18)$$

The bounds are used to initialize an iterative algorithm (dichotomy) which approximates r_e^c the value of r^c which satisfies Eq.3.10. In a few cases (very flat triangles, for instance), it can happen that the solution is out of the bounds, in which case we retain r_{min} to evaluate r_e^c .

Bibliography

- Aitchison, G. (1965). Soil properties, shear strength and consolidation. In *proceeding 6th Interational Conference Soil Mechanic Foundations Engineering*, volume 3, pages 318–321.
- Aitchison, G. et al. (1985). Relationships of moisture stress and effective stress functions in unsaturated soils. *Golden Jubilee of the International Society for Soil Mechanics and Foundation Engineering: Commemorative Volume*, page 20.
- Aitchison, G. and Martin, R. (1973). A membrane oedometer for complex stress–strain studies in expansive clays. In *Proc. 3rd Int. Conf. Expansive Soils*, pages 83–88.
- Aitchison, G. D. and Donald, I. B. (1956). Some preliminary studies of unsaturated soils. In *2nd ANZ Conf. SMFE, Technical Publications for the New Zealand Institution of Engineers*. Wellington, New Zealand.
- Al-Gharbi, M. S. and Blunt, M. J. (2005). Dynamic network modeling of two-phase drainage in porous media. *Phys. Rev. E*, 71:016308.
- Al-Sharrad, M. A. (2013). *Evolving anisotropy in unsaturated soils: experimental investigation and constitutive modelling*. PhD thesis, University of Glasgow.
- Alonso, E. (1993). Constitutive modelling of unsaturated soils. *Civil Engineering European Course, Programe of Continuing Education*. UPC.
- Alonso, E., Gens, A., and Hight, D. (1987). Special problem soils. general report. In *Proceedings of the 9th European conference on soil mechanics and foundation engineering, Dublin*, volume 3, pages 1087–1146.
- Alonso, E. E., Gens, A., and Josa, A. (1990). A constitutive model for partially saturated soils. *Géotechnique*, 40(3):405–430.
- Alonso, E. E., Pereira, J.-M., Vaunat, J., and Olivella, S. (2010). A microstructurally based effective stress for unsaturated soils. *Géotechnique*, 60(12):913–925.
- Andò, E., Hall, S. A., Viggiani, G., Desrues, J., and Bésuelle, P. (2012). Grain-scale experimental investigation of localised deformation in sand: a discrete particle tracking approach. *Acta Geotechnica*, 7(1):1–13.
- Aslyng, H. (1963). Soil physics terminology. *Int. Soc. Soil Sci. Bull.*, 23:7–10.

- Aurenhammer, F. (1991). Voronoi diagrams - a survey of a fundamental geometric data structure. *ACM Comput. Surv.*, 23(3):345–405.
- Bagi, K. (1996). Stress and strain in granular assemblies. *Mechanics of materials*, 22(3):165–177.
- Bagi, K. (2006). Analysis of microstructural strain tensors for granular assemblies. *Int. J. of Solids and Structures*, 43(10):3166–3184.
- Barden, L. (1965). Consolidation of compacted and unsaturated clays. *Geotechnique*, 15(3):267–286.
- Bear, J. (1972). *Dynamics of fluids in porous media*. American Elsevier, New York.
- Biot, M. A. (1941). General theory of three-dimensional consolidation. *Journal of applied physics*, 12(2):155–164.
- Bishop, A. and Donald, I. (1961). The experimental study of partly saturated soil in the triaxial apparatus. In *Proceedings of the 5th international conference on soil mechanics and foundation engineering, Paris*, volume 1, pages 13–21.
- Bishop, A. W. (1960). *The principles of effective stress*. Norges Geotekniske Institutt.
- Bishop, A. W., Alpan, I., Blight, G., and Donald, I. (1960). Factors controlling the strength of partly saturated cohesive soils. In *Conference Shear Strength Cohesive Soils*, pages 503–532. American Society of Civil Engineers: New York.
- Bishop, A. W. and Blight, G. (1963). Some aspects of effective stress in saturated and partly saturated soils. *Géotechnique*, 13(3):177–197.
- Blunt, M. and King, P. (1991). Relative permeabilities from two- and three-dimensional pore-scale network modelling. *Transport in porous media*, 6(4):407–433.
- Boissonnat, J.-D., Devillers, O., Teillaud, M., and Yvinec, M. (2000). Triangulations in cgal (extended abstract). In *Proceedings of the Sixteenth Annual Symposium on Computational Geometry, SCG '00*, pages 11–18, New York, NY, USA. ACM.
- Bolzon, G., Schrefler, B., and Zienkiewicz, O. (1996). Elastoplastic soil constitutive laws generalized to partially saturated states. *Géotechnique*, 46(2):279–289.
- Brackley, I. (1971). Partial collapse in unsaturated expansive clay. In *Proceedings of the 5th Regional Conference for Africa on Soil Mechanics and Foundation Engineering, [Luanda]*, volume 1, pages 23–30.
- Brooks, R. H. and Corey, A. T. (1964). Hydraulic properties of porous media and their relation to drainage design. *Transactions of the ASAE*, 7(1):26–0028.
- Brutsaert, W. (1967). Some methods of calculating unsaturated permeability. *Transactions of the ASAE*, 10(3):400–0404.
- Bryant, S. and Blunt, M. (1992). Prediction of relative permeability in simple porous media. *Phys. Rev. A*, 46:2004–2011.

-
- Bryant, S., King, P., and Mellor, D. (1993a). Network model evaluation of permeability and spatial correlation in a real random sphere packing. *Transport in Porous Media*, 11(1):53–70.
- Bryant, S. L., Mellor, D. W., and Cade, C. A. (1993b). Physically representative network models of transport in porous media. *AIChE Journal*, 39(3):387–396.
- Buckley, S. E., Leverett, M., et al. (1942). Mechanism of fluid displacement in sands. *Transactions of the AIME*, 146(01):107–116.
- Burland, J. (1965). Some aspects of the mechanical behaviour of partly saturated soils. *Moisture Equilibria and Moisture Change in Soils Beneath Covered Areas*, 270:10–20.
- Calvetti, F., Combe, G., and Lanier, J. (1997). Experimental micromechanical analysis of a 2d granular material: relation between structure evolution and loading path. *Mech. Cohes.-Frict. Mater.*, 2(2):121–163.
- Campbell, G. S. (1974). A simple method for determining unsaturated conductivity from moisture retention data. *Soil science*, 117(6):311–314.
- Catalano, E. (2012). *A pore-scale coupled hydromechanical model for biphasic granular media*. PhD thesis, Grenoble INP.
- Catalano, E., Chareyre, B., and Barthélémy, E. (2014). Pore-scale modeling of fluid-particles interaction and emerging poromechanical effects. *International Journal for Numerical and Analytical Methods in Geomechanics*, 38(1):51–71.
- Chalak, C. (2016). *Multi-phase and multi-material interactions in granular media*. PhD thesis, Grenoble INP.
- Chalak, C., Chareyre, B., Nikooee, E., and Darve, F. (2016). Partially saturated media: from dem simulation to thermodynamic interpretation (accepted). *European Journal of Environmental and Civil Engineering*.
- Chandler, R., Koplik, J., Lerman, K., and Willemsen, J. F. (1982). Capillary displacement and percolation in porous media. *Journal of Fluid Mechanics*, 119:249–267.
- Chareyre, B., Briançon, L., and Villard, P. (2002). Theoretical versus experimental modeling of the anchorage capacity of geotextiles in trenches. *Geosynthetics International*, 9(2):97–123.
- Chareyre, B., Cortis, A., Catalano, E., and Barthélemy, E. (2012). Pore-scale modeling of viscous flow and induced forces in dense sphere packings. *Transport in Porous Media*, 92(2):473–493.
- Chen, S. and Doolen, G. D. (1998). Lattice boltzmann method for fluid flows. *Annual Review of Fluid Mechanics*, 30(1):329–364.
- Chou, P. C. and Pagano, N. J. (1967). *Elasticity*. D. Van Nostrand.
-

- Colagrossi, A. and Landrini, M. (2003). Numerical simulation of interfacial flows by smoothed particle hydrodynamics. *Journal of Computational Physics*, 191(2):448–475.
- Coleman, J. D. (1962). Stress/strain relations for partly saturated soils. *Géotechnique*, 12(4):348–350.
- Croney, D. (1952). The movement and distribution of water in soils. *Géotechnique*, 3(1):1–16.
- Cui, Y. and Delage, P. (1996). Yielding and plastic behaviour of an unsaturated compacted silt. *Géotechnique*, 46(2):291–311.
- Culligan, K. A., Wildenschild, D., Christensen, B. S. B., Gray, W. G., Rivers, M. L., and Tompson, A. F. B. (2004). Interfacial area measurements for unsaturated flow through a porous medium. *Water Resources Research*, 40(12):n/a–n/a. W12413.
- Cundall, P. A. and Strack, O. D. L. (1979). A discrete numerical model for granular assemblies. *Géotechnique*, 29(1):47–65.
- de Gennes, P.-G. and Guyon, E. (1978). Lois générales pour l’injection d’un fluide dans un milieu poreux aléatoire. *J. Mec*, 17(3):403–432.
- Di, Y., Li, R., Tang, T., and Zhang, P. (2007). Level set calculations for incompressible two-phase flows on a dynamically adaptive grid. *Journal of Scientific Computing*, 31(1-2):75–98.
- Dias, M. M. and Payatakes, A. C. (1986). Network models for two-phase flow in porous media part 1. immiscible microdisplacement of non-wetting fluids. *Journal of Fluid Mechanics*, 164:305–336.
- Donald, I. B. (1961). *The mechanical properties of saturated and partly saturated soils, with special reference to the influence of negative pore water pressures*. PhD thesis, Imperial College London.
- Drescher, A. and De Jong, G. D. J. (1972). Photoelastic verification of a mechanical model for the flow of a granular material. *Journal of the Mechanics and Physics of Solids*, 20(5):337–340.
- Edelsbrunner, H. and Shah, N. (1996). Incremental topological flipping works for regular triangulations. *Algorithmica*, 15(3):223–241.
- Ennis, B. J., Li, J., Robert, P., et al. (1990). The influence of viscosity on the strength of an axially strained pendular liquid bridge. *Chemical Engineering Science*, 45(10):3071–3088.
- Escario, V. and Saez, J. (1986). The shear strength of partly saturated soils. *Geotechnique*, 36(3).
- Fatt, I. (1956). The network model of porous media i. capillary pressure characteristics. *Trans AIME*, 207:144–159.

- Fenwick, D. H., Blunt, M. J., et al. (1998). Network modeling of three-phase flow in porous media. *SPE Journal*, 3(01):86–96.
- Fisher, R. (1926). On the capillary forces in an ideal soil; correction of formulae given by W.B. Haines. *The Journal of Agricultural Science*, 16(03):492–505.
- Fredlund, D. and Morgenstern, N. (1976). Constitutive relations for volume change in unsaturated soils. *Canadian Geotechnical Journal*, 13(3):261–276.
- Fredlund, D., Morgenstern, N., and Widger, R. (1978). The shear strength of unsaturated soils. *Canadian geotechnical journal*, 15(3):313–321.
- Fredlund, D., Rahardjo, H., and Gan, J. (1987). Non-linearity of strength envelope for unsaturated soils. In *Proc. 6th Int. Conf. Expansive Soils, New Delhi*, volume 1, pages 49–54.
- Fredlund, D., Xing, A., and Huang, S. (1994). Predicting the permeability function for unsaturated soils using the soil-water characteristic curve. *Canadian Geotechnical Journal*, 31(4):533–546.
- Fredlund, D. G. (2005). Terzaghi lecture: "unsaturated soil mechanics in engineering".
- Fredlund, D. G. and Morgenstern, N. R. (1977). Stress state variables for unsaturated soils. *Journal of Geotechnical and Geoenvironmental Engineering*, 103(ASCE 12919).
- Fredlund, D. G. and Rahardjo, H. (1993). *Soil mechanics for unsaturated soils*. John Wiley & Sons.
- Fredlund, D. G., Rahardjo, H., and Fredlund, M. D. (2012). *Unsaturated soil mechanics in engineering practice*. John Wiley & Sons.
- Fredlund, D. G. and Xing, A. (1994). Equations for the soil-water characteristic curve. *Canadian geotechnical journal*, 31(4):521–532.
- Fulk, D. A. and Quinn, D. W. (1996). An analysis of 1-d smoothed particle hydrodynamics kernels. *Journal of Computational Physics*, 126(1):165–180.
- Fung, Y. (1965). *Foundation of soil mechanics*.
- Gan, J., Fredlund, D., and Rahardjo, H. (1988). Determination of the shear strength parameters of an unsaturated soil using the direct shear test. *Canadian Geotechnical Journal*, 25(3):500–510.
- Gardner, W. (1958). Some steady-state solutions of the unsaturated moisture flow equation with application to evaporation from a water table. *Soil science*, 85(4):228–232.
- Gens, A., Alonso, E., and Josa, A. (1989). Elastoplastic modelling of partially saturated soils. *proc. 3rd int. sym. on numerical models in geomechanics (NUMOG), Niagara Falls*, pages 163–170.
- Gens, A., Sánchez, M., and Sheng, D. (2006). On constitutive modelling of unsaturated soils. *Acta Geotechnica*, 1(3):137–147.

- Gladkikh, M. and Bryant, S. (2003). Prediction of interfacial areas during imbibition in simple porous media. *Advances in Water Resources*, 26(6):609 – 622.
- Gopala, V. R. and van Wachem, B. G. (2008). Volume of fluid methods for immiscible-fluid and free-surface flows. *Chemical Engineering Journal*, 141(1–3):204 – 221.
- Gueyffier, D., Li, J., Nadim, A., Scardovelli, R., and Zaleski, S. (1999). Volume-of-fluid interface tracking with smoothed surface stress methods for three-dimensional flows. *Journal of Computational physics*, 152(2):423–456.
- Gunstensen, A. K., Rothman, D. H., Zaleski, S., and Zanetti, G. (1991). Lattice boltzmann model of immiscible fluids. *Physical Review A*, 43(8):4320.
- Harris, C. C. and Morrow, N. R. (1964). Pendular moisture in packings of equal spheres. *Nature*, 203:706–708.
- Hassanizadeh, S. M., Celia, M. A., and Dahle, H. K. (2002). Dynamic effect in the capillary pressure–saturation relationship and its impacts on unsaturated flow. *Vadose Zone Journal*, 1(1):38–57.
- Hilpert, M. and Miller, C. T. (2001). Pore-morphology-based simulation of drainage in totally wetting porous media. *Advances in Water Resources*, 24(3–4):243 – 255. Pore Scale Modeling.
- Hirt, C. W. and Nichols, B. D. (1981). Volume of fluid (vof) method for the dynamics of free boundaries. *Journal of computational physics*, 39(1):201–225.
- Hotta, K., Takeda, K., and Iinoya, K. (1974). The capillary binding force of a liquid bridge. *Powder Technology*, 10(4):231–242.
- Hughes, R. and Blunt, M. (2000). Pore scale modeling of rate effects in imbibition. *Transport in Porous Media*, 40(3):295–322.
- Iveson, S. M., Litster, J. D., Hapgood, K., and Ennis, B. J. (2001). Nucleation, growth and breakage phenomena in agitated wet granulation processes: a review. *Powder technology*, 117(1):3–39.
- Jain, A. K. and Juanes, R. (2009). Preferential mode of gas invasion in sediments: Grain-scale mechanistic model of coupled multiphase fluid flow and sediment mechanics. *Journal of Geophysical Research: Solid Earth*, 114(B8):n/a–n/a. B08101.
- Jennings, J. (1961). A revised effective stress law for use in the prediction of the behaviour of unsaturated soils. *Pore pressure and suction in soils*, pages 26–30.
- Jennings, J. and Burland, J. (1962). Limitations to the use of effective stresses in partly saturated soils. *Géotechnique*, 12(2):125–144.
- Jerier, J.-F., Hathong, B., Richefeu, V., Chareyre, B., Imbault, D., Donze, F.-V., and Doremus, P. (2010). Study of cold powder compaction by using the discrete element method. *Powder Tech.*, In Press.

- Joekar-Niasar, V. and Hassanizadeh, S. M. (2012). Analysis of fundamentals of two-phase flow in porous media using dynamic pore-network models: A review. *Critical Reviews in Environmental Science and Technology*, 42(18):1895–1976.
- Joekar-Niasar, V., Hassanizadeh, S. M., and Dahle, H. K. (2010a). Non-equilibrium effects in capillarity and interfacial area in two-phase flow: dynamic pore-network modelling. *Journal of Fluid Mechanics*, 655:38–71.
- Joekar-Niasar, V., Prodanović, M., Wildenschild, D., and Hassanizadeh, S. M. (2010b). Network model investigation of interfacial area, capillary pressure and saturation relationships in granular porous media. *Water Resources Research*, 46(6):n/a–n/a. W06526.
- Jommi, C. (2000). Remarks on the constitutive modelling of unsaturated soils. *Experimental evidence and theoretical approaches in unsaturated soils*, 153:139–153.
- Josa, A., Balmaceda, A., Gens, A., and Alonso, E. (1992). An elastoplastic model for partially saturated soils exhibiting a maximum of collapse. *3rd international conference on computational plasticity, Barcelona*, 1:815–826.
- Khaddour, G., Hashemi, A., Salager, S., Desrues, J., Massart, T. J., and Francois, B. (2013). Phase segmentation in 3d x-ray images of unsaturated granular materials. In *XVI French-Polish Colloquium of Soil and Rock Mechanics*.
- Khaksar, H., Habibagahi, G., and Nikooee, E. (2013). *SWRC Modeling in Unsaturated Soils: A Pore Network Approach*, chapter 186, pages 1570–1579.
- Khalili, N., Geiser, F., and Blight, G. (2004). Effective stress in unsaturated soils: review with new evidence. *International Journal of Geomechanics*, 4(2):115–126.
- Khalili, N. and Khabbaz, M. (1998). A unique relationship of chi for the determination of the shear strength of unsaturated soils. *Géotechnique*, 48(5).
- Khalili, N. and Loret, B. (2001). An elasto-plastic model for non-isothermal analysis of flow and deformation in unsaturated porous media: formulation. *International Journal of Solids and Structures*, 38(46):8305–8330.
- Kharaghani, A., Metzger, T., and Tsotsas, E. (2011). A proposal for discrete modeling of mechanical effects during drying, combining pore networks with dem. *AIChE Journal*, 57(4):872–885.
- Kharaghani, A., Metzger, T., and Tsotsas, E. (2012). An irregular pore network model for convective drying and resulting damage of particle aggregates. *Chemical Engineering Science*, 75:267 – 278.
- King, P. (1987). The fractal nature of viscous fingering in porous media. *Journal of Physics A: Mathematical and General*, 20(8):L529.
- Kohgo, Y., Nakano, M., and Miyazaki, T. (1993). Theoretical aspects of constitutive modelling for unsaturated soils. *SOILS AND FOUNDATIONS*, 33(4).

- Koplik, J. and Lasseeter, T. (1985). Two-phase flow in random network models of porous media. *Society of Petroleum Engineers Journal*, 25(01):89–100.
- Lenormand, R. (1990). Liquids in porous media. *Journal of Physics: Condensed Matter*, 2(S):SA79.
- Lenormand, R. and Bories, S. (1980). Description d'un mécanisme de connexion de liaison destine a l'étude du drainage avec piégeage en milieu poreux. *CR Acad. Sci*, 291:279–282.
- Lenormand, R., Touboul, E., and Zarcone, C. (1988). Numerical models and experiments on immiscible displacements in porous media. *Journal of Fluid Mechanics*, 189:165–187.
- Leong, E. C. and Rahardjo, H. (1997). Permeability functions for unsaturated soils. *Journal of Geotechnical and Geoenvironmental Engineering*, 123(12):1118–1126.
- Li, X. (2003). Effective stress in unsaturated soil: a microstructural analysis. *Géotechnique*, 53(2):273–277.
- Lian, G., Thornton, C., and Adams, M. J. (1993). A theoretical study of the liquid bridge forces between two rigid spherical bodies. *Journal of colloid and interface science*, 161(1):138–147.
- Likos, W. J. and Jaafar, R. (2013). Pore-scale model for water retention and fluid partitioning of partially saturated granular soil. *Journal of Geotechnical and Geoenvironmental Engineering*, 139(5):724–737.
- Lindquist, W. B., Lee, S.-M., Coker, D. A., Jones, K. W., and Spanne, P. (1996). Medial axis analysis of void structure in three-dimensional tomographic images of porous media. *Journal of Geophysical Research: Solid Earth*, 101(B4):8297–8310.
- Liu, M., Liu, G., and Lam, K. (2003). Constructing smoothing functions in smoothed particle hydrodynamics with applications. *Journal of Computational and applied Mathematics*, 155(2):263–284.
- Liu, Y. and Snoeyink, J. (2005). A comparison of five implementations of 3d delaunay tessellation. In Pach, J., Goodman, J. E., and Welzl, E., editors, *Combinatorial and Computational Geometry*, pages 439–458. MSRI Publications.
- Loret, B. and Khalili, N. (2000). A three-phase model for unsaturated soils. *International Journal for Numerical and Analytical Methods in Geomechanics*, 24(11):893–927.
- Loret, B. and Khalili, N. (2002). An effective stress elastic–plastic model for unsaturated porous media. *Mechanics of Materials*, 34(2):97–116.
- Lu, T., Nielsen, D., and Biggar, J. (1995). Water movement in glass bead porous media: 3. theoretical analyses of capillary rise into initially dry media. *Water Resources Research*, 31(1):11–18.

-
- Ma, S., Mason, G., and Morrow, N. R. (1996). Effect of contact angle on drainage and imbibition in regular polygonal tubes. *Colloids and Surfaces A: Physicochemical and Engineering Aspects*, 117(3):273 – 291.
- Maâtouk, A., Leroueil, S., and La Rochelle, P. (1995). Yielding and critical state of a collapsible unsaturated silty soil. *Géotechnique*, 45(3):465–477.
- Marketos, G. and Bolton, M. D. (2010). Flat boundaries and their effect on sand testing. *International Journal for Numerical and Analytical Methods in Geomechanics*, 34(8):821–837.
- Marzougui, D. (2014). *Extension de la DEM aux granulaires immergés pour l'étude des suspensions denses*. PhD thesis, Grenoble INP.
- Marzougui, D., Chareyre, B., and Chauchat, J. (2015). Microscopic origins of shear stress in dense fluid–grain mixtures. *Granular Matter*, 17(3):297–309.
- Mason, G. (1971). A model of the pore space in a random packing of equal spheres. *Journal of Colloid and Interface Science*, 35(2):279 – 287.
- Mason, G. and Mellor, D. W. (1995). Simulation of drainage and imbibition in a random packing of equal spheres. *Journal of Colloid and Interface Science*, 176(1):214 – 225.
- Mason, G. and Morrow, N. R. (1991). Capillary behavior of a perfectly wetting liquid in irregular triangular tubes. *Journal of Colloid and Interface Science*, 141(1):262–274.
- Matyas, E. L. and Radhakrishna, H. (1968). Volume change characteristics of partially saturated soils. *Géotechnique*, 18(4):432–448.
- Mayer, R. P. and Stowe, R. A. (1965). Mercury porosimetry—breakthrough pressure for penetration between packed spheres. *Journal of Colloid Science*, 20(8):893 – 911.
- Mei, R., Luo, L.-S., and Shyy, W. (1999). An accurate curved boundary treatment in the lattice boltzmann method. *Journal of computational physics*, 155(2):307–330.
- Mitarai, N. and Nori, F. (2006). Wet granular materials. *Advances in Physics*, 55(1-2):1–45.
- Modaressi, A. and Abou-Bekr, N. (1994). A unified approach to model the behaviour of saturated and unsaturated soils. In *Proc of 8th Int Conf Computer Methods and Advances in Geomechanics*, pages 1507–1513.
- Mogensen, K. and Stenby, E. H. (1998). A dynamic two-phase pore-scale model of imbibition. *Transport in Porous Media*, 32(3):299–327.
- Monaghan, J. and Kocharyan, A. (1995). Sph simulation of multi-phase flow. *Computer Physics Communications*, 87(1):225–235.
- Morgenstern, N. (1979). Properties of compacted soils. In *Contribution to panel discussion, Session IV, Proc., 6th Panamerican Conf. on Soil Mechanics and Foundation Engineering*, volume 3, pages 349–354.
-

- Morris, J. P. (2000). Simulating surface tension with smoothed particle hydrodynamics. *International Journal for Numerical Methods in Fluids*, 33(3):333–353.
- Mualem, Y. (1974). A conceptual model of hysteresis. *Water Resources Research*, 10(3):514–520.
- Newitt, D. and Conway-Jones, J. (1958). A contribution to the theory and practice of granulation. *Trans. Inst. Chem. Eng*, 36.
- Nikooee, E., Habibagahi, G., Khaksar, H., Hassanizadeh, S., and Raoof, A. (2014). Pore network modeling of unsaturated soils: Fundamentals, recent advancements and future perspectives. In *Numerical Methods in Geotechnical Engineering - NUMGE 2014*, A. Hicks, Ronald B.J. Brinkgreve & Alexander Rohe (Eds.), pages 1007–1012. Crc Press.
- Nitao, J. J. and Bear, J. (1996). Potentials and their role in transport in porous media. *Water Resources Research*, 32(2):225–250.
- Noble, D. R., Chen, S., Georgiadis, J. G., and Buckius, R. O. (1995). A consistent hydrodynamic boundary condition for the lattice boltzmann method. *Physics of Fluids (1994-present)*, 7(1):203–209.
- Nuth, M. and Laloui, L. (2008). Effective stress concept in unsaturated soils: Clarification and validation of a unified framework. *International journal for numerical and analytical methods in Geomechanics*, 32(7):771–801.
- Olsson, E. and Kreiss, G. (2005). A conservative level set method for two phase flow. *Journal of computational physics*, 210(1):225–246.
- Øren, P.-E. and Bakke, S. (2003). Reconstruction of berea sandstone and pore-scale modelling of wettability effects. *Journal of Petroleum Science and Engineering*, 39(3):177–199.
- Osher, S. and Sethian, J. A. (1988). Fronts propagating with curvature-dependent speed: algorithms based on hamilton-jacobi formulations. *Journal of computational physics*, 79(1):12–49.
- Pham, H. Q. (2005). *A volume-mass constitutive model for unsaturated soils*. PhD thesis, University of Saskatchewan.
- Pham, H. Q., Fredlund, D. G., and Barbour, S. L. (2005). A study of hysteresis models for soil-water characteristic curves. *Canadian Geotechnical Journal*, 42(6):1548–1568.
- Pitois, O., Moucheront, P., and Chateau, X. (2001). Rupture energy of a pendular liquid bridge. *The European Physical Journal B - Condensed Matter and Complex Systems*, 23(1):79–86.
- Princen, H. (1968). Comments on “the effect of capillary liquid on the force of adhesion between spherical solid particles”. *Journal of Colloid and interface Science*, 26(2):249–253.

-
- Princen, H. (1969). Capillary phenomena in assemblies of parallel cylinders: Ii. capillary rise in systems with more than two cylinders. *Journal of Colloid and Interface Science*, 30(3):359 – 371.
- Prodanović, M. and Bryant, S. L. (2006). A level set method for determining critical curvatures for drainage and imbibition. *Journal of Colloid and Interface Science*, 304(2):442 – 458.
- Prodanović, M., Lindquist, W., and Seright, R. (2006). Porous structure and fluid partitioning in polyethylene cores from 3d x-ray microtomographic imaging. *Journal of Colloid and Interface Science*, 298(1):282 – 297.
- Raeini, A. Q., Blunt, M. J., and Bijeljic, B. (2012). Modelling two-phase flow in porous media at the pore scale using the volume-of-fluid method. *Journal of Computational Physics*, 231(17):5653–5668.
- Raouf, A. and Hassanizadeh, S. M. (2013). Saturation-dependent solute dispersivity in porous media: Pore-scale processes. *Water Resources Research*, 49(4):1943–1951.
- Rostami, A., Habibagahi, G., Ajdari, M., and Nikooee, E. (2015). Pore network investigation on hysteresis phenomena and influence of stress state on the swrc. *International Journal of Geomechanics*, 15(5):04014072.
- Russell, A. and Khalili, N. (2006). A unified bounding surface plasticity model for unsaturated soils. *International Journal for Numerical and Analytical Methods in Geomechanics*, 30(3):181–212.
- Scholtès, L., Chareyre, B., Michallet, H., Catalano, E., and Marzougui, D. (2015). Modeling wave-induced pore pressure and effective stress in a granular seabed. *Continuum Mechanics and Thermodynamics*, 27(1-2):305–323.
- Scholtès, L., Chareyre, B., Nicot, F., and Darve, F. (2009). Micromechanics of granular materials with capillary effects. *International Journal of Engineering Science*, 47(1):64 – 75.
- Scholtès, L., Hicher, P.-Y., Nicot, F., Chareyre, B., and Darve, F. (2009a). On the capillary stress tensor in wet granular materials. *International Journal for Numerical and Analytical Methods in Geomechanics*, 33(10):1289–1313.
- Scholtès, L., Nicot, F., Chareyre, B., and Darve, F. (2009b). Discrete modelling of capillary mechanisms in multi-phase granular media. *Computer Modeling in Engineering and Sciences*, 52(3):297–318.
- Schrefler, B. (1984). *The finite element method in soil consolidation*. PhD thesis, University College of Swansea.
- Shan, X. and Chen, H. (1993). Lattice boltzmann model for simulating flows with multiple phases and components. *Physical Review E*, 47(3):1815.

- Sheng, D., Gens, A., Fredlund, D. G., and Sloan, S. W. (2008). Unsaturated soils: from constitutive modelling to numerical algorithms. *Computers and Geotechnics*, 35(6):810–824.
- Sheng, D., Sloan, S., and Gens, A. (2004). A constitutive model for unsaturated soils: thermomechanical and computational aspects. *Computational Mechanics*, 33(6):453–465.
- Sheppard, A., Sok, R., and Averdunk, H. (2005). Improved pore network extraction methods. In *International Symposium of the Society of Core Analysts*, pages 21–25.
- Silin, D. and Patzek, T. (2006). Pore space morphology analysis using maximal inscribed spheres. *Physica A: Statistical Mechanics and its Applications*, 371(2):336 – 360.
- Silin, D. B., Jin, G., and Patzek, T. W. (2003). Robust determination of the pore space morphology in sedimentary rocks. In *SPE Annual Technical Conference and Exhibition*. Society of Petroleum Engineers.
- Sinha, P. K. and Wang, C.-Y. (2007). Pore-network modeling of liquid water transport in gas diffusion layer of a polymer electrolyte fuel cell. *Electrochimica Acta*, 52(28):7936–7945.
- Skempton, A. (1960). Significance of terzaghi’s concept of effective stress (terzaghi’s discovery of effective stress). *From Theory to Practice in Soil Mechanics*. John Wiley & Sons Inc.
- Slowik, V., Hübner, T., Schmidt, M., and Villmann, B. (2009). Simulation of capillary shrinkage cracking in cement-like materials. *Cement and Concrete composites*, 31(7):461–469.
- Soulie, F., Cherblanc, F., El Youssoufi, M. S., and Saix, C. (2006). Influence of liquid bridges on the mechanical behaviour of polydisperse granular materials. *International journal for numerical and analytical methods in geomechanics*, 30(3):213–228.
- Sussman, M., Almgren, A. S., Bell, J. B., Colella, P., Howell, L. H., and Welcome, M. L. (1999). An adaptive level set approach for incompressible two-phase flows. *Journal of Computational Physics*, 148(1):81 – 124.
- Sussman, M., Smereka, P., and Osher, S. (1994). A level set approach for computing solutions to incompressible two-phase flow. *Journal of Computational physics*, 114(1):146–159.
- Sweijen, T., Nikooee, E., Hassanizadeh, S. M., and Chareyre, B. (2016). The effects of swelling and porosity change on capillarity: Dem coupled with a pore-unit assembly method. *Transport in Porous Media*, pages 1–20.
- Swift, M. R., Orlandini, E., Osborn, W., and Yeomans, J. (1996). Lattice boltzmann simulations of liquid-gas and binary fluid systems. *Physical Review E*, 54(5):5041.
- Tamagnini, R. (2004). An extended cam-clay model for unsaturated soils with hydraulic hysteresis. *Géotechnique*, 54(3):223–228.

-
- Tartakovsky, A. M. and Meakin, P. (2005). Simulation of unsaturated flow in complex fractures using smoothed particle hydrodynamics. *Vadose Zone Journal*, 4(3):848–855.
- Tartakovsky, A. M. and Meakin, P. (2006). Pore scale modeling of immiscible and miscible fluid flows using smoothed particle hydrodynamics. *Advances in Water Resources*, 29(10):1464–1478.
- Terzaghi, v. K. (1936). The shearing resistance of saturated soils and the angle between the planes of shear. In *Proceedings of the 1st International Conference on Soil Mechanics and Foundation Engineering*, volume 1, pages 54–56. Harvard University Press Cambridge, MA.
- Tong, A.T., Catalano, E., and Chareyre, B. (2012). Pore-scale flow simulations: Model predictions compared with experiments on bi-dispersed granular assemblies. *Oil Gas Sci. Technol. – Rev. IFP Energies nouvelles*, 67(5):743–752.
- Tuller, M., Or, D., and Dudley, L. M. (1999). Adsorption and capillary condensation in porous media: Liquid retention and interfacial configurations in angular pores. *Water Resources Research*, 35(7):1949–1964.
- van der Marck, S. C., Matsuura, T., and Glas, J. (1997). Viscous and capillary pressures during drainage: Network simulations and experiments. *Phys. Rev. E*, 56:5675–5687.
- Van Dijke, M. and Sorbie, K. (2006). Existence of fluid layers in the corners of a capillary with non-uniform wettability. *Journal of colloid and interface science*, 293(2):455–463.
- Van Genuchten, M. T. (1980). A closed-form equation for predicting the hydraulic conductivity of unsaturated soils. *Soil science society of America journal*, 44(5):892–898.
- Vizika, O., Avraam, D., and Payatakes, A. (1994). On the role of the viscosity ratio during low-capillary-number forced imbibition in porous media. *Journal of colloid and interface science*, 165(2):386–401.
- Šmilauer et al., V. (2015). *Yade Documentation 2nd ed.* The Yade Project. <http://yadedem.org/doc/>.
- Welch, S. W. and Wilson, J. (2000). A volume of fluid based method for fluid flows with phase change. *Journal of computational physics*, 160(2):662–682.
- Wheeler, S., Sharma, R., and Buisson, M. (2003). Coupling of hydraulic hysteresis and stress–strain behaviour in unsaturated soils. *Géotechnique*, 53(1):41–54.
- Wheeler, S. J. and Sivakumar, V. (1995). An elasto-plastic critical state framework for unsaturated soil. *Géotechnique*, 45(1):35–53.
- Wilkinson, D. and Willemsen, J. F. (1983). Invasion percolation: a new form of percolation theory. *Journal of Physics A: Mathematical and General*, 16(14):3365.
-

- Yuan, C., Chareyre, B., and Darve, F. (2015a). A pore-scale approach of two-phase flow in granular porous media. In *Particles 2015 IV International Conference on Particle-Based Methods*, E. Onate, M. Bischoff, DRJ Owen, P. Wriggers and T.Zohdi (Eds), Barcelona.
- Yuan, C., Chareyre, B., and Darve, F. (2015b). Pore-scale simulations of drainage in granular materials: finite size effects and the representative elementary volume. *Advances in Water Resources*.
- Zerhouni, M. (1991). *Rôle de la pression interstitielle négative dans le comportement des sols: application au calcul des routes*. PhD thesis, Châtenay-Malabry, Ecole Centrale Paris.
- Zhao, H. Q., Macdonald, I. F., and Kwiecien, M. J. (1994). Multi-orientation scanning: A necessity in the identification of pore necks in porous media by 3-d computer reconstruction from serial section data. *Journal of Colloid and Interface Science*, 162(2):390 – 401.
- Zou, Q. and He, X. (1997). On pressure and velocity boundary conditions for the lattice boltzmann bgk model. *Physics of Fluids (1994-present)*, 9(6):1591–1598.

Résumé en français

Introduction Générale

La présence de deux fluides non miscibles dans un matériau granulaire déformable est fréquente dans la nature et dans de nombreux domaines de l'ingénierie et de la science. Pour comprendre l'évolution d'un tel système multiphase, il est nécessaire de connaître les propriétés de chaque phase, leur distribution et leurs interactions aux interfaces.

Le mouvement des phases fluides du système (ou écoulement biphasique) inclue le déplacement individuel de chaque fluide et le mouvement des interfaces fluide-fluide. Dans le régime quasi-statique, le mouvement peut être au mouvement des interfaces uniquement. Pour décrire l'écoulement dans l'espace complexe du milieu poreux, des difficultés apparaissent. Les modèles à l'échelle des pores (pore-network) idéalisent l'espace comme un réseau de pores séparés par des étranglements. Des critères locaux sont ensuite définis pour conditionner les événements locaux.

Le mouvement des grains solides est déduit des lois du mouvement de Newton. Moyennant des lois de contact appropriées entre grains voisins, nous pouvons obtenir la déformation du squelette granulaire à l'échelle microscopique. La méthode des éléments discrets (DEM) fournit un cadre pertinent pour l'intégration numérique de ce problème. Compte tenu des effets des fluides sur chaque particule solide, nous devons formuler les forces fluide agissant sur ces particules via la pression des fluides et la tension d'interface.

Le couplage mécanique nécessite un lien direct et explicite entre la géométrie du réseau et les positions des grains solides. Récemment, une approche à l'échelle des pores baptisée PFV-DEM a été considérée comme une approche efficace pour la simulation de ces couplages dans les matériaux saturés Chareyre et al. (2012); Tong, A.T. et al. (2012); Catalano et al. (2014); Scholtès et al. (2015). L'extension aux problèmes biphasiques est le point clé de cette thèse.

Dans ce travail, nous proposons un modèle hydromécanique à l'échelle des pores pour les milieux poreux partiellement saturés, appelé " 2PFV-DEM " (pore-scale two-phase flow - discrete element method) modèle. Il est conçu principalement pour simuler le drainage de matériaux granulaires déformables. Le schéma de couplage est similaire à celui de la méthode PFV-DEM. L'évolution quasi-statique se traduit par une séquence d'états d'équilibres successifs, dans laquelle le mouvement des interfaces est suivi. Nous nous attachons à définir de la manière la plus fidèle possible la géométrie des phases pour déterminer les forces engendrées par les pressions et la tension superficielle sur les grains solides dans chaque pore.

Nous appliquons ce modèle pour étudier deux problèmes: (1) évaluer les effets de la taille et des effets de bord avec une série de tests de drainage primaires; (2) suivre la

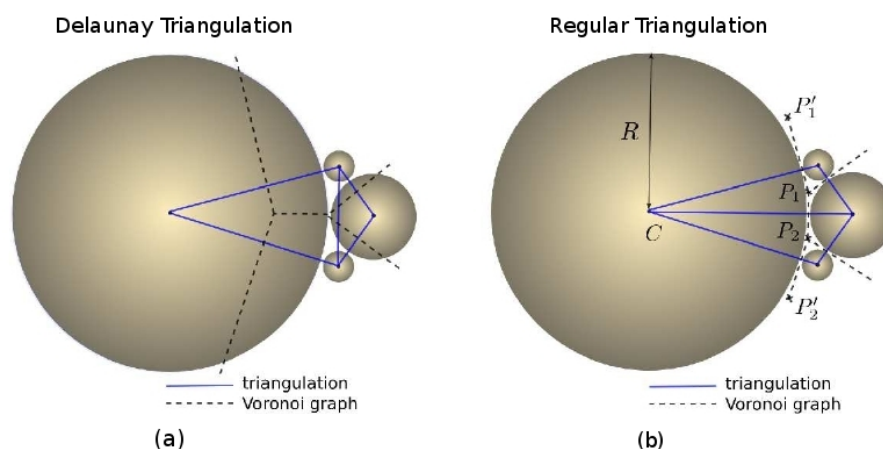


Figure 7.18: Comparaison des triangulations et de leur graph dual de Voronoi en deux dimensions. (a) le graphe dual de la triangulation de Delaunay contient des branches à l’intérieur des disques; (b) le dual de la Triangulation régulière contient toutes les branches dans l’espace poral.

contrainte effective en relation avec la saturation. Dans la dernière partie le modèle est combiné à un modèle de pont liquide pendulaire développé indépendamment Scholtès et al. (2009); Scholtès et al. (2009a); Chalak (2016). Les effets des ponts capillaires sont analysés par comparaison avec le modèle 2PFV-DEM seul.

Le 2PFV-DEM modèle

Réseau de pores

La phase solide est considérée comme un arrangement dense et aléatoire de sphères polydisperses, généré par la méthode des éléments discrets. La représentation de l’espace poral comme un réseau est obtenue en trois dimensions en utilisant la méthode de triangulation régulière.

La triangulation régulière généralise la triangulation de Delaunay classique aux points pondérés, où le poids représente la taille de chaque sphère Edelsbrunner and Shah (1996). Cette triangulation est appropriée pour décrire le chemin d’écoulement dans l’espace des pores, par opposition aux graph Delaunay/Voronoi classiques (voir Fig.7.18). Des exemples typiques sont présentés sur la Fig.7.19. Un pore est défini comme l’espace poral entouré de quatre sphères solides, dont les centres sont les sommets du tétraèdre correspondant. Le volume du pore correspond à la cavité irrégulière à l’intérieur du tétraèdre (voir Fig.7.20 (a)). L’étranglement entre deux pores (ou “gorge”) correspond à la surface contenue dans une facette tétraédrique (Fig.7.20 (b)).

Phases fluides

Règles de drainage

Nous supposons un régime quasi-statique et un mouillage parfait de la phase solide par la phase de mouillage (phase W). Nous représentons le réseau en 3D, en utilisant une

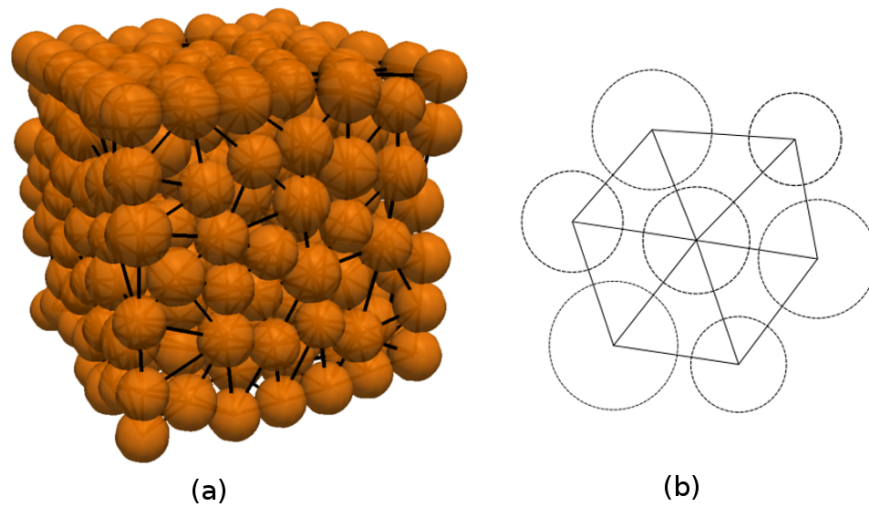


Figure 7.19: Triangulation régulière en trois dimensions (a) et en deux dimensions (b).

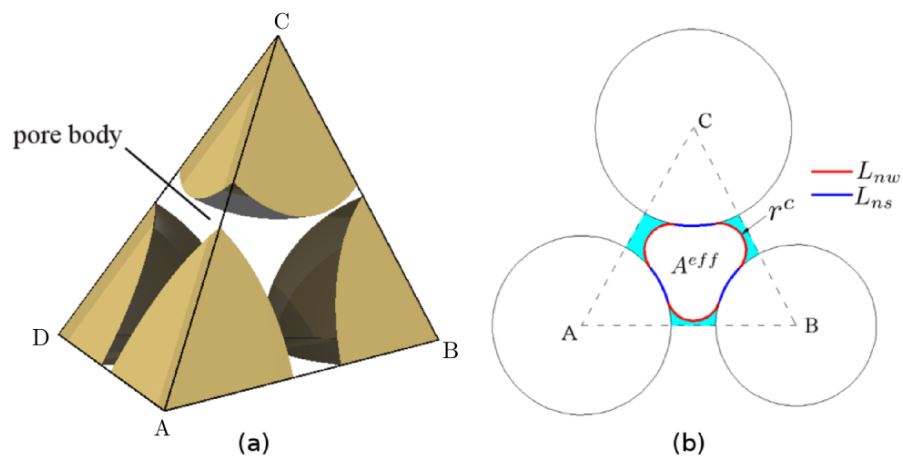


Figure 7.20: Géométrie des pores. (a) un pore tétraédrique. (b) un étranglement. r^c est la courbure de l'interface; L_{nw} longueur de la ligne de contact entre phases NW et W; L_{ns} longueur de la ligne de contact NW-S. $L^{eff} = \sum(L_{nw} + L_{ns})$ où L^{eff} est le périmètre effectif de l'étranglement. A^{eff} est l'aire d'entrée effective.

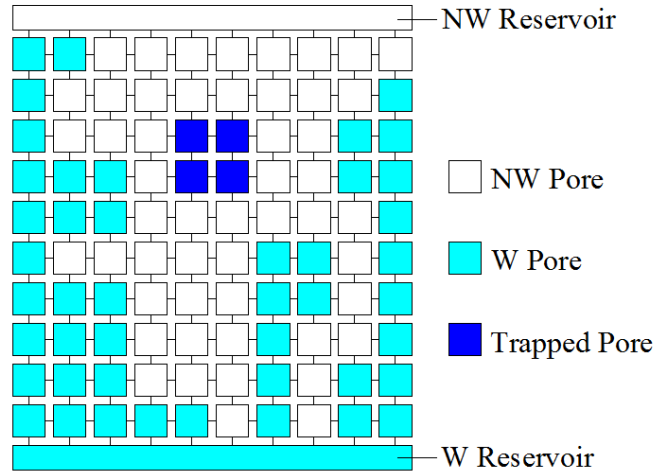


Figure 7.21: Illustration des conditions aux limites, l'invasion de la phase NW et le piégeage de la phase W.

cartographie de réseau en 2D dans un souci de clarté (voir Fig.7.21). Les pores et les gorges sont représentés par des carrés et des connexions linéaires respectivement. Dans un premier temps, l'échantillon est totalement saturé. Nous supposons que les limites supérieures et inférieures sont connectées à des réservoirs NW et W, respectivement. Le drainage commence en diminuant la pression de la phase W p^w tandis que la pression p^n du réservoir NW est maintenue constante. Dès qu'un pore est envahi, la phase NW atteint de nouveaux point d'étranglement, déclenchant éventuellement une cascade récursive de "sauts de Haines", et envahissant plus d'un pore pour une seule valeur de p^w appliquée, jusqu'à ce qu'il n'y ait plus aucune gorge satisfaisant $p_e^c < p^c$ accessible à la phase NW.

Sur de courtes périodes de temps, nous supposons que la phase W peut être déconnectée de son réservoir. Nous qualifions ce mode de drainage, le drainage "with-trap". Alternativement, un drainage "no-trap" peut être supposé pour refléter l'évolution de long terme. Dans le modèle, nous pouvons décider si les pores proches de la limite latérale devraient être disponibles pour l'invasion, ou tout simplement ignorées comme ne participant pas au système. Nous appelons ces deux hypothèses "open boundary" et "closed-boundary", respectivement.

Détermination de la pression capillaire d'entrée

Nous proposons de déterminer p_e^c basée sur la méthode MS-P (Mayer-Stowe-Princen), qui emploie l'équilibre des forces sur l'interface NW-W (Mayer and Stowe (1965); Princen (1969))

$$\sum \mathbf{F}(p^c) = \mathbf{F}^c(p^c) + \mathbf{F}^t(p^c) = 0 \quad (7.19)$$

où F^c est la pression capillaire agissant sur l'interface et F^t est la force totale de tension superficielle sur son contour. p_e^c est la valeur de p^c telle que $\sum \mathbf{F}(p^c) = 0$. Sous une hypothèse de mouillage parfait cet équilibre conduit à

$$\mathbf{F}_{ij}^t = \int_{\partial^w \Phi_i \cap \Theta_j \cap \mathcal{S}_{ij}} \gamma^{nw} \mathbf{n} dl + \int_{\partial^s \Phi_i \cap \Theta_j \cap \mathcal{S}_{ij}} \gamma^{nw} \mathbf{n} dl = L_{ij}^{eff} \gamma^{nw} \mathbf{n} \quad (7.20)$$

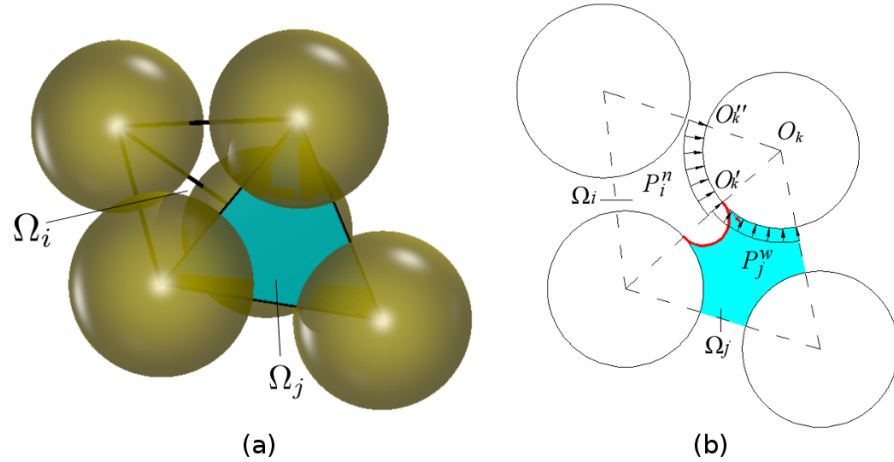


Figure 7.22: (a) Construction d'un sous-domaine Ω_{ij} , les pores de Ω_i sont occupés par la phase NW (Φ_i), le pore de Ω_j est occupé par la phase W (Θ_j); (b) La pression du fluide à deux phases et la tension interfaciale sur la phase S. (En 2D pour la clarté).

dans laquelle, L_{ij}^{eff} est la longueur totale des lignes de contact. Tous les termes de Eq.7.20 peuvent être exprimés en fonction de r^c , comme le suit,

$$\sum \mathbf{F}(r^c) = \mathbf{F}^c(r^c) + \mathbf{F}^t(r^c) = 0 \quad (7.21)$$

La résolution de l'équation numérique donne r_e^c . À son tour, p_e^c peut être déterminée.

Les phases solides

La force totale F^k induit sur la particule k par la présence des fluides comprend les effets des pressions de fluides p et des tensions interfaciales S-NW-W γ ,

$$\mathbf{F}^k = \int_{\partial\Gamma_k} p \mathbf{n} ds + \int_{\partial\Phi \cap \partial\Gamma_k} \gamma \mathbf{n} dl = \mathbf{F}^{c,k} + \mathbf{F}^{t,k} \quad (7.22)$$

Nous supposons qu'un pore ne peut être remplie que par une seule phase fluide. En considérant les pores incidents à une particule k (voir Fig.3.5),

$$\mathbf{F}_i^{c,k} = \int_{\partial\Gamma_k \cap \Omega_i} p_i \mathbf{n} ds = \begin{cases} \int_{\partial\Gamma_k \cap \Phi_i} p_i^n \mathbf{n} ds & : \text{if } \Omega_i \text{ is occupied by NW-phase (i.e., } p_i = p_i^n) \\ \int_{\partial\Gamma_k \cap \Theta_i} p_i^w \mathbf{n} ds & : \text{if } \Omega_i \text{ is occupied by W-phase (i.e., } p_i = p_i^w) \end{cases} \quad (7.23)$$

La force totale de tension F_{ij}^t s'appliquant sur la phase solide dans le domaine Ω_{ij} s'exerce sur trois sphères différentes, et devra être divisée plus tard en trois termes. F_{ij}^t est défini comme le suit:

$$\mathbf{F}_{ij}^t = \int_{\partial\Phi_i \cap \Theta_j \cap S_{ij}} \gamma \mathbf{n} dl, \quad (7.24)$$

résultat obtenu à partir de Eq.7.20 lors du calcul de p_e^c . La force de tension interfaciale sur la phase S dépend des longueurs des lignes de contact NW-W-S:

$$\mathbf{F}_{ij}^{t*} = \int_{\partial^s \Phi_i \cap \Theta_j} \gamma^{nw} \mathbf{n} dl \quad (7.25)$$

d'où

$$\sum \mathbf{F}_{ij} = \mathbf{F}_{ij}^{c*} + \mathbf{F}_{ij}^{t*} = 0 \quad (7.26)$$

où les \mathbf{F}_{ij}^{c*} sont les effets des pressions de phases.

$$\mathbf{F}_{ij}^{c*} = \int_{\partial \Phi_i \cap \Theta_j} (p^n - p^w) \mathbf{n} ds \simeq A_{ij}^f (p^n - p^w) \mathbf{n} \quad (7.27)$$

dans lequel, A_{ij}^f est l'aire de la gorge dans la facette S_{ij} . La combinaison de Eq.7.25-7.27 donne la force de traction totale

$$\mathbf{F}_{ij}^{t*} = -A_{ij}^f (p^n - p^w) \mathbf{n} \quad (7.28)$$

La force sur la sphère k s'écrit donc

$$\mathbf{F}_{ij}^{t*,k} = \mathbf{F}_{ij}^{t*} \frac{\delta_{ij}^k}{\sum_{k=1}^3 \delta_{ij}^k} \quad (7.29)$$

Enfin, la force totale sur une particule est obtenue en additionnant les forces de tension interfaciales et de pression de toutes les facettes incidentes suivant

$$\mathbf{F}^k = \sum_{(ij)_{incident}} \{ \mathbf{F}_i^{c,k} + \mathbf{F}_{ij}^{t*,k} \} \quad (7.30)$$

Mise en œuvre

Le modèle 2PFV-DEM a été implémenté dans la plate-forme Yade. La génération du réseau par triangulation régulière a été implémentée en C++ et utilise la librairie CGAL-Boissonnat et al. (2000).

Simulations numériques

Comparaison des courbes de rétention d'eau avec des essais correspondants

Configuration de simulation

On vérifie le modèle en comparant les résultats de la simulation avec des données expérimentales, provenant d'un essai de drainage en régime quasi-statique, dans un milieu poreux synthétique Culligan et al. (2004). Une boîte cubique de taille 5.0 mm × 6.0 mm × 5.0 mm est définie, dans laquelle 400 sphères sont placées. La distribution de taille (PSD - voir Tab.7.1) et la

Weight(%)	Diameter(mm)
30	1-1.4
35	0.850
35	0.600

Table 7.1: Distribution de la taille des particules de l'expérience.

porosité sont définies comme dans l'essai. Pour plus de généralité, les données de l'essai et des simulations sont tous proposées sous la forme sans dimension, dans laquelle P_c est normalisée par

$$\bar{p}^c = \frac{p^c \bar{D}}{\gamma^{nw}} \quad (7.31)$$

dans lequel, \bar{p}^c est appelée pression capillaire normalisée, γ^{nw} est la tension interfaciale NW-W et \bar{D} est la taille moyenne des sphères.

Résultats

Nous calculons le drainage primaire pour 100 arrangement aléatoires ayant la même PSD et la même porosité. Fig.7.23 présente les résultats, dans lesquels nous recueillons tous les points (\bar{p}^c, s^w) éparés de chaque simulation pour les superposer sur un même graph. Comme le montre la Fig.7.23, les courbes $\bar{p}^c - s^w$ montrent un accord assez bon avec l'expérience. Les données expérimentales sont dans la gamme de fluctuation des simulations.

Nous observons la géométrie du processus d'invasion par des sections d'échantillon dans la Fig.7.24. La comparaison des tranches (b) et (c) montre que dans certaines circonstances, même une très faible variation de la pression capillaire peut provoquer un déplacement significatif des interfaces. La tranche.(d) indique la fin de la simulation, où une saturation résiduelle est obtenue. Le champs de pression du fluide résiduel est représenté sur la Fig.7.25.

Conclusions

L'objectif principal de cette thèse est de fournir une méthodologie numérique efficace pour reproduire les comportements hydrauliques et mécaniques des matériaux partiellement saturés. Nous nous sommes concentré sur une approche couplée à l'échelle des pores, dans laquelle une technique de décomposition spatiale et la méthode des éléments discrets (DEM) ont été combinées pour les fluides et les grains solides respectivement. Un lien explicite a été établi entre la géométrie de l'espace poral et la position des grains.

Le modèle a été spécialement établi afin de simuler l'évolution quasi-statique des phases lors du drainage. Sous conditions oedométriques, une série d'essais de drainage primaire a été simulée. Les données expérimentales de référence (courbes de rétention d'eau) sont prédites de manière satisfaisante.

Nous avons appliqué le modèle 2PFV-DEM pour aborder trois questions liées aux couplages hydromécaniques (voir développements dans le corps de la thèse):

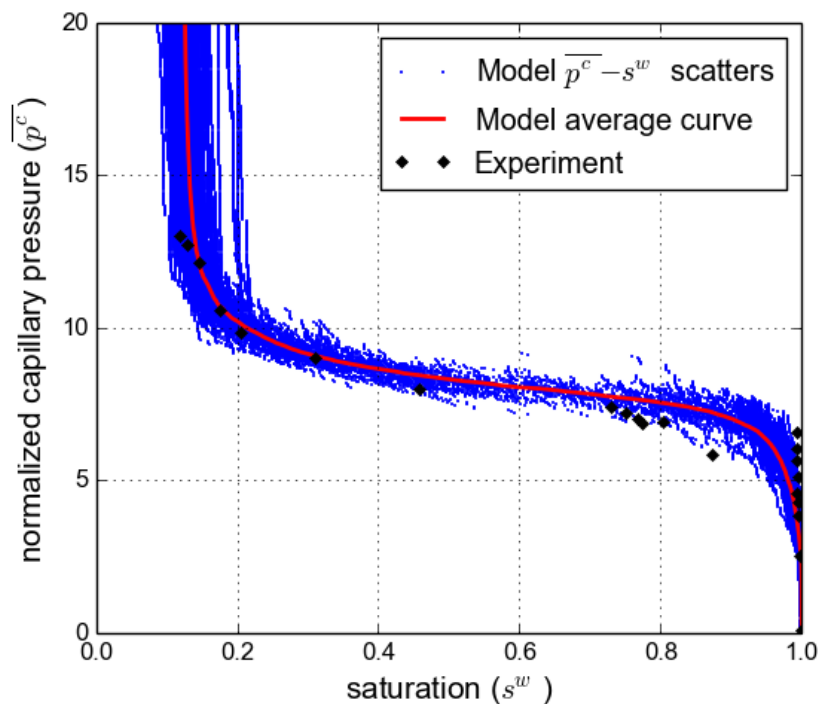


Figure 7.23: Comparaison entre la simulation et l'expérience pour les courbes de drainage primaire $\bar{p}^c - s^w$ (100 simulations superposées).

- Les effets de taille et les effets de bord: les résultats montrent que l'écart-type de la saturation suit une loi simple de la réduction de variance avec l'augmentation de la taille de l'échantillon. L'écart-type ne devrait pas être le seul critère pour évaluer la représentativité; la taille de l'échantillon peut aussi être la cause de biais importants sur les moyennes moyennes. Nous avons constaté que au moins 20,000 sphères doivent être utilisées afin de réduire le biais à moins de 0.02 en terme de saturation.
- Le paramètre de contrainte effective de Bishop χ : χ est exprimé selon des points de vue macroscopique et microscopique. Les résultats montrent que les deux grandeurs sont assez semblables. Nous concluons que la contrainte micromécanique de contact peut être considérée comme l'analogie à micro-échelle de la contrainte effective macroscopique.
- En outre, le régime 2PFV-DEM a été étendu pour inclure les ponts liquides du régime pendulaire et évaluer leur contribution. Bien que les ponts pendulaires contribuent faiblement au volume total de fluide, ils contribuent de manière significative à la déformation du squelette granulaire.

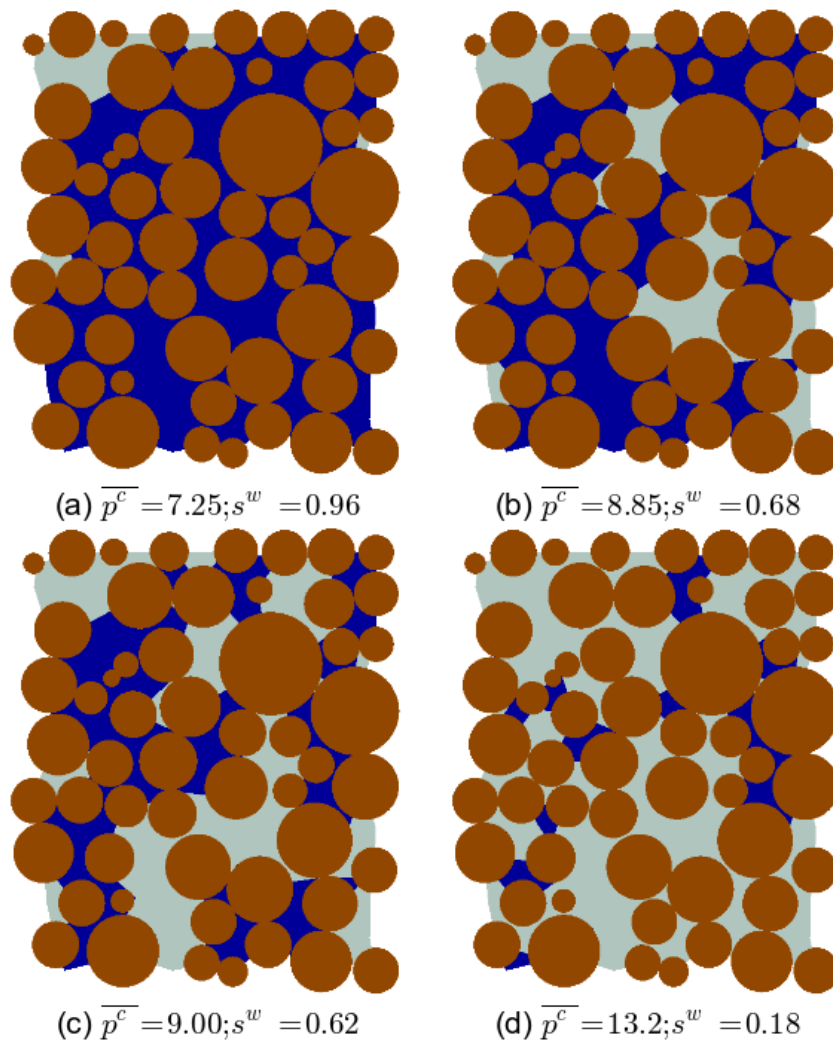


Figure 7.24: Processus de drainage (400 particules), la phase NW envahie par le haut. Brown (gris) est la phase solide, celle bleue (noir) est la phase W, et celle cyan claire (blanc) est la phase NW.

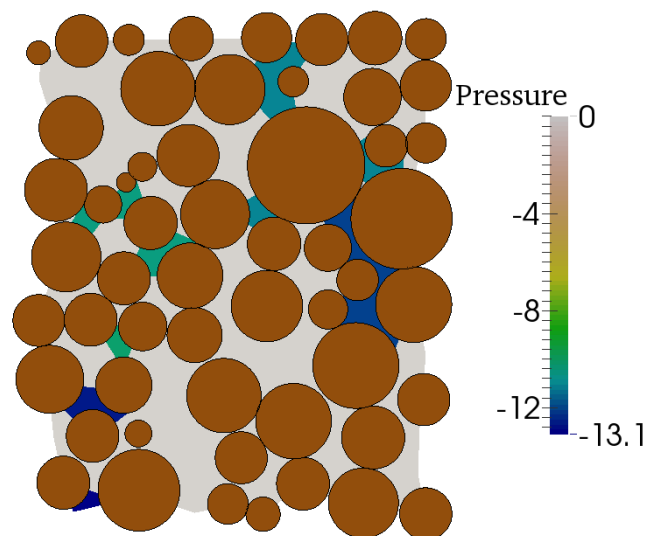


Figure 7.25: Distribution de la pression capillaire en mode de drainage "avec-trap". Le cercle de Brown est en phase solide, la région en couleur claire signifie la pression p^n en phase NW, les régions en couleur sombres sont des pressions W en phase p^w .